The Resonant Acousto-Optic Effect

R. H. Poolman

A Thesis submitted to
Cardiff University
for the degree of
Doctor of Philosophy

March 6, 2012

Declaration

This work has not previously been accepted in substance for any degree and is not being concurrently submitted in candidature for any degree.

Signed: _____
Candidate

Date: _____

Statement 1

This thesis is the result of my own investigations, except where otherwise stated. Other sources are acknowledged by giving explicit references. A bibliography is appended.

Signed: _____
Candidate

Date: _____

Statement 2

I hereby give consent for my thesis, if accepted, to be available for photocopying and for inter-library loan, and for the title and summary to be available to outside organisations.

Signed: _____
Candidate

Date: _____

Dedicated to the memory of Prof. Alexei Ivanov

Acknowledgments

It has been my privilege to work with my late supervisor Prof. Alexei Ivanov. He was a source of great help and support throughout both my final undergraduate year and my PhD studies. I could not have asked for a more dedicated supervisor. Prof. Ivanov's support is acknowledged in the dedication of this thesis. I would also like to thank Dr. Egor Muljarov, initially for his help with the numerical methods used in this thesis and lately for replacing Prof. Ivanov as my first supervisor, under difficult circumstances. In the later stages of PhD in particular, Dr. Muljarov has shown a great deal of patience and support to his student. I have been very fortunate to be taught by such dedicated physicists.

I am thankful to my office mates, Joanna, Joe, Kanchana, Leonidas and Mark. They have been a continual source of support, encouragement and good humour. I am particular thankful to Joe for putting his kettle in the office, the most vital piece of equipment I used in my entire PhD!

I am grateful to the invaluable advice I received in the earl stages of my PhD from Dr. Fabio Biancalana on computational numerics in particular, and on the pitfalls of PhD studies in general. Briefly, before Dr. Muljarov came to Cardiff, he was my second supervisor and provided a great deal help in this role. I would also like to thank Prof. Wolfgang Langbein, Prof. Sergei Tikhodeev, Prof. Dmitry Khokhlov and Prof. R. Zimmermann for valuable discussions throughout my PhD. I am also grateful to Dr. George Zorinyants for his assistance in translating Russian texts.

Finally, I would like to thank my family. My parents, Ken and Lyn, for the support and love they have shown. I could not have taken this opportunity if they had not helped me through the early stages of education with patience and enthusiasm. My partner, Hannah, for her love, help and patience. Without her encouragement I would not have attempted a PhD and without her support I would not have completed it. Throughout my undergraduate and postgraduate years she has been a constant source of support and encouragement, thank you.

Abstract

This dissertation is theoretical investigation of the resonant acousto-optic effect in ionic crystals and thin metal foils. The optical properties of these types of materials, in the presence of coherent acoustic pump excitation, are numerically modelled and compared with analytical results.

The resonant acousto-optic effect in bulk ionic materials is shown to be dependent on the coupling of a bulk acoustic wave to the TO-phonon component of a TO-phonon polariton. This requires that the material used is not only an ionic crystal but also has a strongly anharmonic interatomic potential. It is also demonstrated that the process "TO phonon $\pm$ one (two) transverse acoustic phonon(s)$\rightarrow$ TO phonon" is responsible for the cubic (quartic) resonant acousto-optic effect. The role of acoustic intensity and frequency in the optical properties of CuCl and TlCl is considered. Higher order transitions are also investigated.

It is shown that, in the ferroelectric material $LiNbO_3$, both cubic and quartic scattering channels are sufficiently strong enough to consider the resonant acousto-optic effect associated with them on an equal footing. The coupling strength of both scattering channels is estimated to the nearest order of magnitude. The cubic coupling is found be $\sigma_3 = 5$ meV and the quartic coupling strength is found to be $\sigma_4 = 0.3$ meV both for the acoustic intensity $I_{\text{ac}} = 25$ kWcm^{-2}. The effect the phase difference between the two anharmonic terms has on the optical properties of $LiNbO_3$ is then investigated. A tunable THz filter is proposed, based on the resonant acousto-optic effect in $LiNbO_3$.

A numerical method is developed to calculated the partial wave amplitudes and optical properties of metal foils with acoustically excited, propagating sinusoidally corrugated surfaces. It is then used on a system of a thin acoustically perturbed Au foil on a glass substrate. The effects of varying the angle of incidence, acoustic wavevector, corrugation amplitude and foil thickness are investigated. The numerical method is shown to remain stable even for strong coupling between the acoustic wave and surface plasmon polariton

Publications

R. H. Poolman, A. L. Ivanov and E. A. Muljarov. Ultrasonic control of terahertz radiation via lattice anharmonicity in $LiNbO_3$ *Appl. Phys. Lett.*, **98**, 263505 (2011).

R. H. Poolman, E. A. Muljarov and A. L. Ivanov. Far-infrared response of acoustically modulated transverse optical-phonon polaritons. *IET Optoelectronics*, **5**, 128 (2011)

E. A. Muljarov, R. H. Poolman, and A. L. Ivanov. Resonant acousto-optics in the terahertz range: TO-phonon polaritons driven by an ultrasonic wave. *Phys. Rev. B* **83**, 115204 (2011)

R. H. Poolman, E. A. Muljarov, and A. L. Ivanov. Terahertz response of acoustically driven optical phonons. *Phys. Rev. B* **81**, 245208 (2010)

Presentations

R. H. Poolman, E. A. Muljarov and A. L. Ivanov. The Resonant Acousto-Optic Effect due to TO-phonon Anharmonicity. *Semiconductor and Integrated Optoelectronics 2010 (SIOE '10)*, Cardiff (29^{th}-31^{st} March 2010).

R. H. Poolman, E. A. Muljarov and A. L. Ivanov. Resonant Acousto-Optic Effect for THz Band of Semiconductors. *Optics of Excitons in Confined Systems 11 (OECS11)*, Madrid (7^{th}-11^{th} September 2009).

Contents

List of Tables

List of Figures

1 Introduction

In 1922 Leon Brillouin proposed the diffraction of light by an acoustic wave (AW) propagating through a given medium, this became the discipline of acousto-optics. However, the experimental confirmation showed that the photoelastic effect was extremely weak, with the dielectric constant contrast of only $\sim 10^{-5}$. Therefore, the resulting diffraction of light was also weak, it is normally seen in the lowest diffraction order only. While this is the case for the non-resonant acousto-optic effect, the *resonant* acousto-optic (RAO) effect causes a far stronger optical response.

This thesis is a theoretical study of the physics of the RAO effect and the resulting modification of the optical properties of the given material. Data were obtain through numerical modelling of two cases and have been compared to analytical results where applicable. The first case to be considered is the RAO effect for transverse optical (TO) phonon polaritons in several ionic crystalline materials. The second is the RAO effect associated with surface plasmon polaritons (SPP) in a thin gold film on a glass substrate.

1.1 Overview

The first chapter studies the theory of the components necessary for RAO effect and gives a review of the previous research on the topic. It presents a conceptual discussion of the cases of the RAO effect studied in this thesis.

Chapter two is entitled "Resonant Acousto-Optics with TO-Phonons: One Anharmonic Term in the Lattice Potential" This chapter considers the RAO effect due to either cubic or quartic anharmonicity in CuCl and TlCl, respectively. It includes a derivation of the macroscopic equations used to perform the numerical calculations, which produced results for both chapters two and three. It also discusses the Hamiltonian of TO-phonon polaritons undergoing acoustic pumping. The numerical results for both the cubic anharmonicity RAO effect and the quartic equivalent will be presented and compared with analytic calculations where applicable. In this chapter higher order effects such as a phase difference induced between multiple anharmonic components will be introduced.

The third chapter is entitled "Resonant Acousto-Optics with TO-Phonons: Two Anharmonic Terms in the Lattice Potential" This chapter investigates an RAO effect due to two anharmonicities in $LiNbO_3$. It includes a discussion of the increased total strength of the RAO effect and of higher order effects of a possible phase difference between the two anharmonic components. Ideas relating to devices constructed from acoustically driven $LiNbO_3$ are also presented.

Chapter four is entitled "Acousto-Plasmonics" and discusses the RAO effect for SPPs in a thin gold film on a glass substrate. This chapter gives an in depth discussion of the effects of replacing the TO-phonon as the mediator between acoustic and light waves. Also discussed is the geometry used in modelling the effect and the particular numerical scheme used to produced the numerical results. Comparison of these results with analytical equivalents is presented where appropriate.

Finally, general conclusions are present in the fifth chapter, along with proposals for further investigation.

1.2 Background

The RAO effect is essentially the enhancement, via the mediation of a solid state excitation, of the interaction between light and sound in a given material. It was proposed in 2001 by Ivanov and Littlewood, who where investigating the possibility of an acoustically induced Stark shift for excitons [1]. The optical Stark effect in a semiconductor is the result of two exciton states being coupled by a high intensity laser pulse in a quantum well structure then probed by weak light [2–4]. The proposal by

Ivanov and Littlewood was to replace the coupling between excitons by high-intensity laser pulses, with acoustical coupling of mixed exciton and light field states, known as exciton polaritons. One of the implications of this is the use of the strong coupling between the exciton and light field in the polariton to improve the strength of the interaction between the acoustic wave and the near infrared light field.

The RAO effect concept has been expand to include various different mediating solid state excitations in a variety of different contexts. In 2003 Ivanov and Littlewood proposed microcavity polaritons for the mediating solid state excitation between the light field and the acoustic wave [5]. The microcavity polariton is a mixed state of quantum well excitons and optical microcavity modes. The acoustic wave induced polariton transitions result in large modifications of the materials optical properties, that are dependent on the acoustic intensity [6, 7]. The experimental confirmation was produced in 2006 from the examination of a surface acoustic wave (SAW) driven quantum well microcavity [8].

An analog of the RAO effect is the coarse periodic modulation superimposed on a Bragg mirror, proposed by Phillip Russel in 1986 [9]. Here, the Bragg mirror takes the place of a polarization field of the crystal lattice. This was extended by Paulo Santos in 2001 when a photonic crystal structure (PCS) was modulated using a SAW, where its was shown that the efficiency of light-sound coupling could be improved by acoustically induced umklapp scattering events in PCS band structure. [10].

In this work the focus will be on the RAO effect mediated by two types of solid state excitation, the transverse optical (TO) phonon [11] and the surface plasmon. The TO-phonon is a dipole active acoustic excitation from one of the upper phonon branches. In ionic materials it propagates as a mixed mode with light, this is know as a TO-phonon polariton. In an analogous way to the RAO effect for excitons, the TO-phonon mediates and strongly enhances the acoustic wave interaction with the light field. For this case of the RAO effect the range of interaction falls between $0 < \omega < 60$ meV, which corresponds to THz light frequencies.

This work also includes a chapter on the use of surface plasmons as a mediator in the RAO effect. A plasmon is the quanta of the oscillation of Fermi-Dirac gas of conduction electrons in a metal, in thin films these are known as surface plasmons and their resonance is red-shifted relative to the bulk plasmon due to the confinement in one direction [12, 13]. For the surface plasmon polariton (SPP) the RAO effect occurs in at the blue of the visible spectrum up to the near ultra violet.

1.3 Surface Acoustic Waves

In general, all AWs can be treated as propagating elastic deformations of a homogeneous and continuous solid medium. The analytic study of these phenomena begins from consideration of the forces exerted on an infinitesimal volume of the material in question by the contiguous volume of which it is a part. This is expressed using the stress tensor T_{ij}, which is the component of force per unit area of the infinitesimal volume normal to the x_i direction, acting on the surface normal to the x_j direction. If the resultant displacement is u_j and there are no further forces to consider then

$$\mu \frac{\partial^2 u_i}{\partial t^2} = \sum_j \frac{\partial T_{ij}}{\partial x_j}, \tag{1.1}$$

where μ is mass per unit length.

Eq. (1.1) gives a general description of stress induced deformation of a continuous homogeneous media rather than merely surface disturbances. By substituting a plane wave solution into the equations an eigenvalue problem can be derived

$$\sum_j (K_{ij} - \delta_{ij}\mu v^2)\beta_j = 0,$$

where $K_{jk} = \sum_{k,l=1}^{3} \varkappa_i \varkappa_j c_{ijkl}$ and β_j are the eigenvectors. The elastic constant tensor is c_{ijkl} and the wavevector of the plane wave solution $\varkappa_i$, all subscripts take values of 1,2 or 3. The eigenvalues for this set of equations are the phase velocities v of the acoustic plane wave associated with β_j. The polarization of the plane wave these solutions represent are mutually orthogonal, there is one quasi-longitudinal and two quasi-shear modes of vibration. In most circumstances the quasi-longitudinal has the higher velocity. In bulk waves the symmetry of the medium can cause waves to adopt pure longitudinal or transverse characteristics, an example of this would isotropic crystals. This bulk case is applicable to the TO-phonon RAO effect, discussed in Chapters 2 and 3.

The case above is for a non-piezoelectric material in which the stress tensor is an expression of the deformation of the material that is linearly dependent on mechanical strain. However, the piezoelectric effect is a part of most surface wave components, leading to a necessity to treat the resultant electric field. It should be noted that, due to the propagation speed of acoustic waves, the electric field can be treated as the gradient of a time dependent scalar potential φ. This not only modifies the stress

tensor but also requires the introduction of an electric displacement $\mathbf{D}$ to which the stress tensor is coupled

$$T_{ij} = \sum_{kl} c_{ijkl} \frac{\partial u_k}{\partial x_l} + \sum_{k} e_{kij} \frac{\partial \varphi}{\partial x_k}, \tag{1.2a}$$

$$D_i = -\sum_{j} \varepsilon_{ij} \frac{\partial \varphi}{\partial x_j} + \sum_{jk} e_{ijk} \frac{\partial u_j}{\partial x_k}. \tag{1.2b}$$

The c_{ijkl} term in Eq. (1.2a) defines the mechanical relationship between stress and strain. The electromechanical tensor is e_{ijk} and is present in the final terms of both Eqs. (1.2). Finally, the dielectric tensor ε_{ij} relates the electric field $\mathbf{E} = \nabla\varphi$ to the dielectric induction $\mathbf{D}$. This displacement field must now be taken into account in the equations of motion by including Maxwell's equation for a charge free dielectric $\nabla \cdot \mathbf{D} = 0$. It should be noted that in a piezoelectric material, the piezoelectric interaction included in Eq. (1.2a) increases the magnitude of the elements of T_{ij}. Thus, the physical effect of the piezoelectric interaction is to stiffen the material.

The surface wave solution stems from the boundary conditions associated with a semi-infinite medium of which the surface has no tangential stress component. On definition of the surface normal in the x_3 direction, and stating that the surface lies at $x_3 = 0$, we can express this boundary condition as

$$T_{3,1} = T_{3,2} = T_{3,3} = 0. \tag{1.3}$$

The surface wave solution to Eq.(1.1) and $\nabla\mathbf{D} = 0$ is a linear combination of partial waves of the form

$$u_j = \alpha_j e^{ik(b_i x_i - vt)}, \tag{1.4}$$

where kb_i is a decay constant and $b_1 \equiv 1$, $b_2 \equiv 0$ and $b_3 \equiv b$. To ensure the amplitudes vanish in the direction anti-parallel to the x_3 axis, it is necessary that complex b have a negative imaginary part.

Using Eq. (1.4) to solve the coupled system results in the eigenvalue problem [14]

$$(L_{kl} - \delta_{kl}\mu v^2)\alpha_k = 0,$$

where $1 \leq k, l \leq 3$ and $\delta_{k,l}$ is the Kronecker delta. The matrix L is dependent of the material constants c_{ijkl}, e_{ijk} and ε_{ik} as well as b. Thus, to determine b the associated

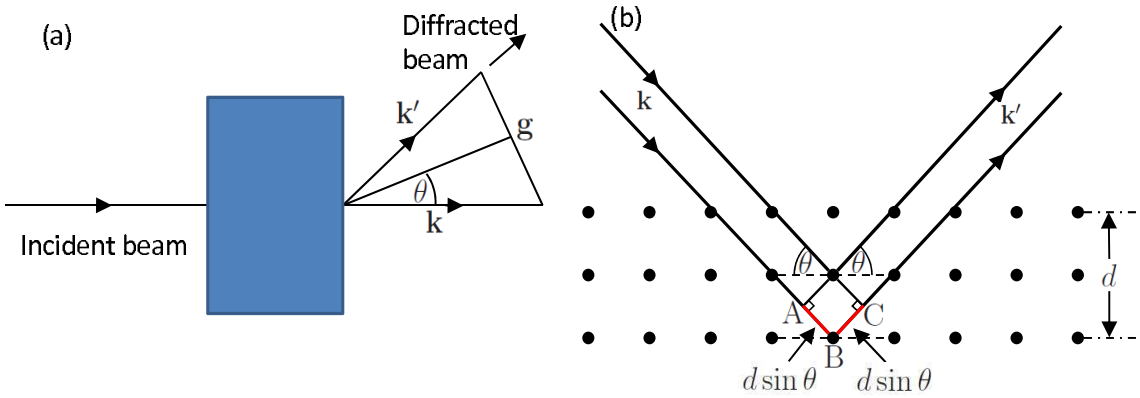

Figure 1.1: A diagram showing the path length difference caused by the reflection of incident light from an array of ions.

determinantal equation can be solved. This produces four roots, the only one of which that pertains to surface waves is complex with an imaginary part from the lower half of the complex plain.

The characteristics of any given surface wave are dependent on the the symmetry of the crystal in which they propagate. The symmetry defines the number of independent elements that can be found in c_{ijkl} and the other material tensors. However, there are few statements that can be made about surface waves in general. The most immediately apparent is that the amplitude of such modes strongly decays into the crystal becoming negligible within $2\lambda_{ac}$ for an isotropic material, where λ_{ac} is the acoustic wavelength. It also the case that the phase velocity of these surface modes is always lower than their bulk equivalent. Further information on SAWs can be found in a collection of articles edited by Oliner [14].

1.4 Bragg Condition

In a material that is made of a periodic array of atoms, the structure can be investigated by considering the scattering of radiation of a specific frequency off the material. This is the basis of X-ray crystallography and several other techniques for characterization of periodic structure. Usually these techniques produce a spectrum of the scattered radiation containing several peaks that yield information about the materials structural properties.

For a monochromatic beam with a wavevector $\mathbf{k}$, which is incident on some material

diffracted beams can be observed at $\mathbf{k}' = \mathbf{k} + \mathbf{g}$. The reciprocal lattice vector of the material is $\mathbf{g}$. If the energy of the diffracted beam and the incident beam are the same, i.e. wavevectors of the same length, then a condition is placed on the scattering angle between the incident and diffracted beams. In Figure 1.1 (a) the angle between the two beams is 2θ, therefore the reciprocal lattice vector is given by

$$|\mathbf{g}| = 2|\mathbf{k}| \sin\theta. \tag{1.5}$$

The magnitude of the reciprocal lattice vector is $|\mathbf{g}| = 2\pi n/d$ where d is the distance between the planes of atoms in a crystalline material as shown in Figure 1.1 (b) and n is an integer. By combining this with Eq. 1.5 and rearranging the result is

$$n\lambda = 2d \sin\theta, \tag{1.6}$$

where $\lambda = 2\pi/|\mathbf{k}|$. This is the Bragg condition. In this thesis an acoustic wave provides a dynamic superlattice and it is this periodicity to which the Bragg condition will be applied. The role of the reciprocal lattice vector will be played by the acoustic wave vector $\mathbf{K}$.

1.5 Optical Phonons

A general crystal with p atoms per unit cell can have the displacement of those atoms represented by $\mathbf{u}(\mathbf{lb})$, where $\mathbf{l}$ labels the unit cell and $\mathbf{b}$ the atom of that unit cell. The potential energy of the crystal V is dependent on the instantaneous position of the atoms contained within the crystal. The equations of motion for lattice waves can be derived using the harmonic approximation of the crystal potential, in which only those terms that are quadratic in $\mathbf{u}(\mathbf{lb})$ are retained

$$V_{\text{harm}} = \frac{1}{2} \sum_{\substack{\mathbf{l}\ \mathbf{l}' \\ \mathbf{b}\ \mathbf{b}' \\ \alpha\ \beta}} \Phi_{\alpha\beta} \begin{pmatrix} \mathbf{l} & \mathbf{l}' \\ \mathbf{b} & \mathbf{b}' \end{pmatrix} u_\alpha \begin{pmatrix} \mathbf{l} \\ \mathbf{b} \end{pmatrix} u_\beta \begin{pmatrix} \mathbf{l}' \\ \mathbf{b}' \end{pmatrix}$$

where

$$\Phi_{\alpha\beta} \begin{pmatrix} \mathbf{l} & \mathbf{l}' \\ \mathbf{b} & \mathbf{b}' \end{pmatrix} = \frac{\partial^2 V}{\partial u_\alpha(\mathbf{lb}) \partial u_\beta(\mathbf{l}'\mathbf{b}')}.$$

This derivative is infinitesimal translational invariance, physically this means when all atoms are displaced identically no potential results. It also displays lattice translational symmetry which manifests as $\Phi(\mathbf{lb};\mathbf{l'b'}) = \Phi(0\mathbf{b};(\mathbf{l'}-\mathbf{l})\mathbf{b'})$. Using this invariance, along with Newtons's second law and Hooke's law we can write the equation of motion using the harmonic potential

$$m_b\ddot{u}_\alpha(\mathbf{lb}) = -\sum_{\mathbf{l'b'}\alpha\beta} \Phi_{\alpha\beta}\begin{pmatrix}0 & \mathbf{l'}\\ \mathbf{b} & \mathbf{b'}\end{pmatrix} u_\beta(\mathbf{l'b'}). \tag{1.7}$$

To derive the phonon dispersion relation a Fourier series solution is used in Eq (1.7) which leads to a determinantal equation for the lattice wave frequency

$$|D_{\alpha,\beta}(\mathbf{bb'}|\mathbf{k}) - \omega^2\delta_{\alpha\beta}\delta_{\mathbf{bb'}}| = 0,$$

where the dynamical matrix is Hermitian and given by

$$D_{\alpha,\beta}(\mathbf{bb'}|\mathbf{k}) = \frac{1}{\sqrt{m_b m_{b'}}}\sum_{\mathbf{l'}} \Phi_{\alpha\beta}\begin{pmatrix}0 & \mathbf{l'}\\ \mathbf{b} & \mathbf{b'}\end{pmatrix} e^{i\mathbf{k}\cdot\mathbf{x}(\mathbf{l'})}$$

with dimensions $3p \times 3p$. Thus, $\omega^2(\mathbf{k}s)$ are the real eigenvalues of the problem, the real roots of which physically correspond to the phonon dispersion branches. The s-dependency of ω indicates that, in general, the dispersion has multiple branches.

The most general phonon dispersion has $3p$ branches, the lowest lying set of three all obey $\omega(0) \to 0$, these are the acoustic phonon modes. Along axis of high symmetry the phonon modes display three orthogonal polarizations, two transverse and one longitudinal. Should $p = 1$ then these are the only phonon modes available to the crystal, however for $p > 1$ higher modes can exist, these are characterized by stationary points in the gradient of the dispersion at the Brillouin zone center. These phonon modes are known as the optical modes, like the acoustic modes there are three polarizations. In the TO-phonon RAO effect the transverse modes are used to mediate the light and acoustic fields. A more complete discussion is given by Srivastava in chapters 2 and 3 of his book [15].

1.6 Interatomic Potential Anharmonicity

The use of a lattice oscillation to mediate the interaction between the acoustic wave and light field means that the interatomic potential plays an important role in the TO-phonon polariton case of the RAO effect. The motion of atoms in a crystalline lattice is caused by interatomic forces that are due to the potential of the given crystalline lattice. The Taylor series expansion of the potential V in powers of the atomic displacement u_α is

$$V = \frac{1}{2}\sum_{\substack{l\ l'\\ b\ b'\\ \alpha\ \beta}} \Phi_{\alpha\beta}\begin{pmatrix} l & l' \\ b & b' \end{pmatrix} u_\alpha \begin{pmatrix} l \\ b \end{pmatrix} u_\beta \begin{pmatrix} l' \\ b' \end{pmatrix} + \tag{1.8}$$
$$\frac{1}{3!}\sum_{\substack{l\ l'\ l''\\ b\ b'\ b''\\ \alpha\ \beta\ \gamma}} \Psi_{\alpha\beta\gamma}\begin{pmatrix} l & l' & l'' \\ b & b' & b'' \end{pmatrix} u_\alpha \begin{pmatrix} l \\ b \end{pmatrix} u_\beta \begin{pmatrix} l' \\ b' \end{pmatrix} u_\gamma \begin{pmatrix} l'' \\ b'' \end{pmatrix} + \dots ,$$

where Φ are the harmonic force constants in the α direction on the atom $(l\ b)$ when the atom $(l'\ b')$ is displaced in the β direction. The cubic anharmonic equivalent is given by Ψ, higher order anharmonicities would have their own terms. Including the quadratic term only in any lattice dynamical model leads only to harmonic oscillations of the atoms of the lattice [15, 16].

An anharmonic potential is the lattice potential that includes higher order terms than quadratic. These terms describe the interaction of phonons and so are essential to the TO-phonon RAO effect, which relies on acoustically induced TO-phonon transitions. The anharmonic potential can be expressed in phonon coordinates $A(\mathbf{q}\,\mathbf{j})$ as [15]

$$\sum_{\substack{\mathbf{q_1}\ \mathbf{q_2}\ \mathbf{q_3}\\ j_1\ j_2\ j_3}} V\begin{pmatrix} \mathbf{q_1} & \mathbf{q_2} & \mathbf{q_3} \\ j_1 & j_2 & j_3 \end{pmatrix} A\begin{pmatrix} \mathbf{q_1} \\ j_1 \end{pmatrix} A\begin{pmatrix} \mathbf{q_2} \\ j_2 \end{pmatrix} A\begin{pmatrix} \mathbf{q_3} \\ j_3 \end{pmatrix} + \dots , \tag{1.9}$$

where

$$V\begin{pmatrix} \mathbf{q_1} & \mathbf{q_2} & \mathbf{q_3} \\ j_1 & j_2 & j_3 \end{pmatrix} = \frac{1}{3!}\frac{i}{\sqrt{N_0\Omega}}\sum_{\substack{b\ b'\ b''\\ \alpha\ \beta\ \gamma}} \left(\frac{\hbar^3}{8m_b m_{b'} m_{b''}\omega(\mathbf{q}_1 j_1)\omega(\mathbf{q}_2 j_2)\omega(\mathbf{q}_3 j_3)}\right)^{1/2}$$
$$\times e_\alpha(b \mid \mathbf{q}_1 j_1) e_\beta(b' \mid \mathbf{q}_2 j_2) e_\gamma(b'' \mid \mathbf{q}_3 j_3)$$
$$\Psi_{\alpha\beta\gamma}\begin{pmatrix} \mathbf{q}_1 & \mathbf{q}_2 & \mathbf{q}_3 \\ b & b' & b'' \end{pmatrix} \delta_{\mathbf{G},\mathbf{q}_1+\mathbf{q}_2+\mathbf{q}_3}. \tag{1.10}$$

The mass of the atom is m_b and the frequency of the phonon from branch j_n with wavevector $\mathbf{q}_n$ is $\omega(\mathbf{q}_n j_n)$, $N_0\Omega$ is the crystal volume and N_0 the number of unit cells. The phonon polarization is $e(b \mid \mathbf{q}j)$ and the Kronecker delta ensures conservation of *crystal* momentum. The phonon coordinates are given by $A(\mathbf{q}j) = a^\dagger_{\mathbf{q}j} - a_{\mathbf{q}j}$ where $a^\dagger_{\mathbf{q}j}$ and $a_{\mathbf{q}j}$ are the phonon creation and annihilation operators respectively. These are derived from canonically conjugate normal coordinates $X(\mathbf{q}j)$ (spatial coordinate) and $P(\mathbf{q}j)$ (momentum) and are given by

$$a_{\mathbf{q}s} = \frac{1}{\sqrt{2\hbar\omega(\mathbf{q}j)}} P(\mathbf{q}j) - i\sqrt{\frac{\omega(\mathbf{q}j)}{2\hbar}} X^\dagger(\mathbf{q}j), \tag{1.11a}$$

$$a^\dagger_{\mathbf{q}s} = \frac{1}{\sqrt{2\hbar\omega(\mathbf{q}j)}} P^\dagger(\mathbf{q}j) + i\sqrt{\frac{\omega(\mathbf{q}j)}{2\hbar}} X(\mathbf{q}j). \tag{1.11b}$$

A full derivation of this can be found in Chapter 4 of Srivastava (1990) [15] and phonon coordinates are discussed in Cowley (1968) [16].

The expansion of the phonon coordinates into their creation and annihilation operators yields four types of terms; the annihilation of two phonons and the creations of one $a_{\mathbf{q}_1 j} a_{\mathbf{q}_2 j'} a^\dagger_{\mathbf{q}_3 j''}$, the creation of two phonons and the annihilation of one $a^\dagger_{\mathbf{q}_1 j} a^\dagger_{\mathbf{q}_2 j'} a_{\mathbf{q}_3 j''}$, the creations of three phonons $a^\dagger_{\mathbf{q}_1 j} a^\dagger_{\mathbf{q}_2 j'} a^\dagger_{\mathbf{q}_3 j''}$ and finally the annihilation of three phonons $a_{\mathbf{q}_1 j} a_{\mathbf{q}_2 j'} a_{\mathbf{q}_3 j''}$. However, due to the crystal momentum conservation $\mathbf{q}_1 + \mathbf{q}_2 + \mathbf{q}_3 = \mathbf{G}$, where $\mathbf{G} = 0$ (*normal* process) or $\mathbf{G} \neq 0$ (*umklapp* process), the latter two terms are virtual three phonon processes. The two types of transition are described by the conservation laws

$$\omega(\mathbf{q}_1 j) + \omega(\mathbf{q}_2 j) = \omega(\mathbf{q}_3 j),$$
$$\mathbf{q}_1 + \mathbf{q}_2 = \mathbf{q}_3 + \mathbf{G},$$

In an *Umklapp* process the sum of the two momenta falls outside the first Brillouin zone and the $\mathbf{G}$ vector is not zero, it acts to flip the third phonon back into the first Brillouin zone.

For the RAO effect with TO-phonons the mediation requires the acoustic wave to interact with the TO-phonon component of the polariton, making the lattice anharmonicity essential. Therefore, strongly anharmonic crystal lattices are the best candidates for the RAO effect. In particular, lattices in which $V(\mathbf{k}\ j_{TO} | \mathbf{K}\ j_{ac} | \mathbf{k}'\ j'_{TO})$ or a higher order equivalent are large, give the strongest interaction between the acoustic wave and TO-phonon that results in an efficient TO-phonon transition.

1.7 Surface Plasmons

This section will introduce the plasmon and plasmon polaritons by show the effect confining it to two dimensions has on its resonant frequency.

1.7.1 Plasmons

In general, plasmons are the quanta associated with an oscillating charged gas. For better understanding of the RAO effect in thin metal films, a discussion of the oscillations of its conduction electrons is necessary. This will begin with a description of plasmons in metals.

Originally, plasmons in metal were investigated by considering a fast electron interacting with the conduction electrons. A physical picture for interactions of this sort was suggested by Pines and Bohm in 1952 [17]. The central idea of this picture is that the interaction of the fast electron with the conduction electrons, leads to fluctuations in the density of the conduction electrons. These fluctuations can be split into two parts, the collective electron behavior and the individual behavior.

The Coulomb repulsion felt between all electrons causes each to be surrounded by a cloud with a radius of the Debye length in which there is lack of electrons. This results in the screening of the field of any given electron. The screening is sufficiently strong enough to render the collision cross section far smaller than the mean free path of the given electron. Therefore, both an electron and its surrounding void are considered an individual free particle. The thermally governed collisions of these particles are the short range density fluctuations that form the individual half of the fast electron interaction picture of Pines and Bohm.

The long range component of the Coulomb force leads to the simultaneous interaction of many of the dressed electrons. To consider an assembly of electrons in a metal requires some account of the ions that form the lattice, and the way in which they effect the electrons. It is assumed that the lattice ions are fixed and that the average charge density associated with them is the same as the electrons. As a result, the positive ionic charge is said to be smeared out and serves to cancel the average negative charge of the electrons. This is known as the jellium model of a metal [12, 17, 18].

To begin with, a unit volume of the metal with periodic boundary conditions is considered. The Fourier transform of the potential energy of the inter-electron interaction is then given by

$$\frac{e^2}{|\mathbf{x}_i - \mathbf{x}_j|} = 4\pi e^2 \sum_k \frac{1}{k^2} e^{i\mathbf{k}\cdot(\mathbf{x}_i - \mathbf{x}_j)},$$

which gives the equation of motion

$$\ddot{\mathbf{x}}_i = -\frac{4\pi e^2 i}{m} \sum_{\substack{j\neq i \\ k\neq 0}} \frac{\mathbf{k}}{k^2} e^{i\mathbf{k}\cdot(\mathbf{x}_i - \mathbf{x}_j)}. \tag{1.12}$$

The electron position is given by $\mathbf{x}$ and the double dots on the left hand side indicate second order differentiation with respect to time. The electron's effective mass is given by m and charge by e. The Fourier inverse of $\mathbf{x}$ is $\mathbf{k}$. The $k = 0$ magnitude is excluded from the sum because it corresponds to the mean electronic charge distribution which is canceled in the jellium model.

For further study of the plasmon, Eq. (1.12) must be written in terms of electron density. As the electrons are considered point particles when dealing with their collective behavior and the system is box of unit volume, conversion of position to density is simply

$$\rho(\mathbf{x}) = \sum_i \delta(\mathbf{x} - \mathbf{x}_i).$$

The Fourier components of which are

$$\rho_k = \sum_i e^{-i\mathbf{k}\cdot\mathbf{x}_i}, \tag{1.13}$$

and in the reverse

$$\rho(\mathbf{x}) = \sum_{i,\mathbf{k}} e^{i\mathbf{k}\cdot(\mathbf{x} - \mathbf{x}_i)}.$$

The mean electron density is ρ_0, which, as the system is a unit volumed box, is also the number of electrons in the system n. When $k \neq 0$ the description is of fluctuations about ρ_0. To complete the conversion of Eq. (1.12) to ρ_k we simply differentiate Eq. (1.13) with respect to time and use Eq. (1.12) to given the acceleration. This

results in

$$\ddot{\rho}_{\mathbf{k}} = -\sum_i (\mathbf{k}\cdot\mathbf{v}_i)^2 e^{-i\mathbf{k}\cdot\mathbf{x}_i} - \sum_{\substack{i\neq j,\ j\neq i \\ \mathbf{k}'\neq 0}} \frac{4\pi n e^2}{m(k')^2}\mathbf{k}\cdot\mathbf{k}' e^{i(\mathbf{k}'-\mathbf{k})\cdot\mathbf{x}_i} e^{-i\mathbf{k}'\cdot\mathbf{x}_j}, \tag{1.14}$$

where the electron velocity is given by $\mathbf{v}_i$.

The first term of this equation is simply the motion of the electrons due to thermal excitation, it is the second term that contains the pertinent information. By considering the second term and splitting the sum over $\mathbf{k}'$ into two parts, one of the central approximations of collective electron behavior can be investigated. The first part of the sum in the second term is $\mathbf{k}' = \mathbf{k}$ and corresponds to the mean electron density, which in the current case of a unit volume, leads to the sum over i yielding n. The second term is the sum over $\mathbf{k}' \neq \mathbf{k}$ and includes the phase factors $\exp[i(\mathbf{k}'-\mathbf{k})\cdot\mathbf{x_i}]$. These position dependent phases tend to cancel to zero, as there are a large number of electrons, randomly distributed. Neglecting this second part of the sum in the first approximation is known as the random phase approximation. This allows Eq. (1.14) to be expressed as

$$\ddot{\rho}_{\mathbf{k}} = -\sum_i (\mathbf{k}\cdot\mathbf{v}_i)^2 e^{-i\mathbf{k}\cdot\mathbf{x}_i} - \frac{4\pi n e^2}{m}\sum_i e^{-i\mathbf{k}\cdot\mathbf{x}_i}. \tag{1.15}$$

In this equation the second term takes account of the effect of particle interactions.

When $\mathbf{k}$ is sufficiently small the first term can be neglected leading to

$$\ddot{\rho}_{\mathbf{k}} = -\frac{4\pi n e^2}{m}\rho_{\mathbf{k}},$$

This is a wave equation for the electron density where the frequency of oscillation is given by the factor in front of $\rho_{\mathbf{k}}$. The organised collective motion of the electrons, manifest as an oscillating electron density, is the plasma oscillation and the plasma frequency ω_p is given by

$$\omega_p = \sqrt{\frac{4\pi n e^2}{m}}. \tag{1.16}$$

From this discussion it must be concluded that unperturbed electrons in a bulk metal take part in random thermal motions that show no collective behavior. In fact the random motions of free particles work to damp any collective disturbance due to the individual angular frequencies of each particle $\mathbf{k}\cdot\mathbf{v}_i$ expressed in the first term of

Eq. (1.15). However, when a Coulomb interaction is applied the result is a collective oscillation, in which each particle shares the same frequency of oscillation given by ω_p. This collective oscillating displacement of the electron density is the plasma oscillation, the quantum of which is a plasmon with energy $\hbar\omega_p$.

1.7.2 Dielectric Treatment of an Electron Gas

Thus far, the plasmon has been described in a unit volume of a given metal, for use in the RAO effect it is necessary to consider the plasmon confined to a thin film. To proceed with this discussion it is convenient to express the effect of electron-electron interactions via a wavevector and frequency dependent dielectric function $\varepsilon(\mathbf{k},\omega)$. This scheme was originally developed independently by Lindhard in 1954 and Hubbard in 1955 as an effective way of dealing with electron many body problems [19]. The condensed treatment given here comes from Solyom, Ziman and Dressel and Gruner [18, 20, 21].

To start with we consider a time dependent perturbation, acting on a free electron gas. The perturbation can be split into two potentials with the same $\mathbf{r}$ and t dependence

$$\delta U(\mathbf{r},t) = \delta V(\mathbf{r},t) + \delta\Phi(\mathbf{r},t), \tag{1.17}$$

where δV is the applied potential, $\delta\Phi$ is the induced potential and the total potential is δU. At position $\mathbf{r}$ and time t any given electron experiences a potential of frequency ω and wavevector $\mathbf{q}$ given by

$$\delta U = U(\mathbf{q})e^{i\mathbf{q}\cdot\mathbf{r}}e^{-i\omega t}e^{\alpha t},$$

which grows, slowly, with time constant α. The perturbation is real and so δU and its complex conjugate δU^* act on state $|\mathbf{k}\rangle$ and couple states $|\mathbf{k}+\mathbf{q}\rangle$ to it. From time dependent perturbation theory it follows that the electron density fluctuation due to the perturbing potential is given by

$$\begin{aligned}\delta\rho =& e\sum_{\mathbf{k}}\left[\frac{U(\mathbf{q})}{\mathcal{E}(\mathbf{k})-\mathcal{E}(\mathbf{k}+\mathbf{q})+\hbar\omega+i\hbar\alpha}\right.\\ &\left.+\frac{U(\mathbf{q})}{\mathcal{E}(\mathbf{k})-\mathcal{E}(\mathbf{k}-\mathbf{q})-\hbar\omega-i\hbar\alpha}\right]e^{i\mathbf{q}\cdot\mathbf{r}}e^{-i\omega t}e^{\alpha t}+\text{complex conjugate.}\end{aligned}$$

To generalise $\delta\rho$ the probability that $|\mathbf{k}\rangle$ is occupied in the unperturbed metal $f_0(\mathbf{k})$ is introduced . This is done by changing the summation variable $\mathbf{k}$ in the second term to $\mathbf{k}+\mathbf{q}$. This leads to

$$\delta\rho = e\sum_{\mathbf{k}} \frac{f_0(\mathbf{k}) - f_0(\mathbf{k}+\mathbf{q})}{\mathcal{E}(\mathbf{k}) - \mathcal{E}(\mathbf{k}+\mathbf{q}) + \hbar\omega + i\hbar\alpha} e^{i\mathbf{q}\cdot\mathbf{r}} U(\mathbf{q}) e^{-i\omega t} e^{\alpha t} + \text{complex conjugate.} \tag{1.18}$$

This is the charge distribution calculated in terms of the total potential.

The charge distribution gives rise to the $\delta\Phi$ potential, which is described in Eq. (1.17), via the Coulomb interaction of the electrons. This allows Poisson's equation to be used to calculate $\delta\Phi$ as a function of $\delta\rho$

$$\nabla^2\delta\Phi = -4\pi e\delta\rho. \tag{1.19}$$

The combination of Eq. (1.18) and Poisson's equation gives

$$\Phi(\mathbf{q}) = \frac{4\pi e^2}{q^2}\sum_{\mathbf{k}} \frac{f_0(\mathbf{k}) - f_0(\mathbf{k}+\mathbf{q})}{\mathcal{E}(\mathbf{k}) - \mathcal{E}(\mathbf{k}+\mathbf{q}) + \hbar\omega + i\hbar\alpha} U(\mathbf{q}). \tag{1.20}$$

By definition

$$\delta U \equiv \frac{\delta V}{\varepsilon(\mathbf{q},\omega)}$$

where, from Eq. (1.17),

$$\delta U = \frac{\delta\Phi}{1-\varepsilon(\mathbf{q},\omega)}.$$

Thus, rearranging this and combining with Eq. (1.20) gives

$$\varepsilon(\mathbf{q},\omega) = 1 - \frac{4\pi e^2}{q^2}\sum_{\mathbf{k}} \frac{f_0(\mathbf{k}) - f_0(\mathbf{k}+\mathbf{q})}{\mathcal{E}(\mathbf{k}) - \mathcal{E}(\mathbf{k}+\mathbf{q}) + \hbar\omega + i\hbar\alpha}, \tag{1.21}$$

which is known as Lindhard's dielectric function. This is the dielectric function for an electron gas in the jellium model of a metal.

For plasmons $\omega >> \alpha$, therefore in this region only the real part of the Lindhard dielectric function needs to be considered. By writing Eq. (1.21) as two terms and using a change of variables $\mathbf{k}+\mathbf{q} \rightarrow \mathbf{k}$ in the second term the Lindhard dielectric

function can be written as [20]

$$\varepsilon(\mathbf{q},\omega) = 1 - \frac{4\pi e^2}{q^2}\sum_{\mathbf{k}} \frac{f_0(\mathbf{k})}{\mathcal{E}(\mathbf{k}) - \mathcal{E}(\mathbf{k}+\mathbf{q}) + \hbar\omega} - \frac{f_0(\mathbf{k})}{\mathcal{E}(\mathbf{k}-\mathbf{q}) - \mathcal{E}(\mathbf{k}) + \hbar\omega}.$$

By changing the variables $\mathbf{k} \to -\mathbf{k}$ in the second term and introducing the energy of the state $\mathbf{k}+\mathbf{q}$ as $\mathcal{E}(\mathbf{k}+\mathbf{q}) = \hbar^2\mathbf{k}\cdot\mathbf{q}/m_e$ then, after some rearrangement, this becomes

$$\varepsilon(\mathbf{q},\omega) = 1 - 4\pi e^2\frac{\hbar^2}{m_e}\sum_{\mathbf{k}} \frac{f_0(\mathbf{k})}{(\hbar\omega - \hbar^2\mathbf{k}\cdot\mathbf{q}/m_e)^2 - \mathcal{E}(\mathbf{k})^2}.$$

For large ω this can be expanded up to q^2 as

$$\varepsilon(\mathbf{q},\omega) = 1 - \frac{4\pi e^2}{m_e\omega^2}\sum_{\mathbf{k}} f_0\left[1 + 2\frac{\hbar}{m_e\omega}\mathbf{k}\cdot\mathbf{q} + 3\left(\frac{\hbar}{m_e\omega}\right)^2(\mathbf{k}\cdot\mathbf{q})^2\right].$$

By considering only the first term, the summation over $\mathbf{k}$ returns number of occupied $\mathbf{k}$ states n, therefore

$$\varepsilon(\mathbf{q},\omega) = 1 - \frac{\omega_p^2}{\omega^2} \tag{1.22}$$

where $\omega_p = (4\pi ne^2)/m_e$. This is the Drude dielectric function.

1.7.3 Surface Plasmons

The concept of the surface plasmon was introduced in 1957 by Ritchie, who predicted that the confinement of a plasmon in a thin metal foil would lead to reduction in the resonant energy of the plasmon [12]. In a 1959 a pair of papers by Powell and Swann verified Ritchie's predictions. The first paper showed a resonance at a lower energy as well as the bulk plasmon resonance in Al films up to 100 Å in thickness [22], the second paper showed the same in Mg films of equivalent thickness [23]. It is this resonance at a reduced energy that is the surface plasmon predicted by Ritchie.

The perturbation discussed in the previous section causes transitions of electrons from occupied to unoccupied levels. Should a conduction electron make a transition, it would be necessary for it to gain a quanta of energy $\hbar\omega$ and momentum $\hbar\mathbf{k}$, the exciting particle would lose energy and momentum of corresponding amount. In the

case of Ritchie, like Pines and Bohm, this exciting particle is a fast electron. The probability, per unit path length, of transitions of this nature occurring is

$$P(\mathbf{k},\omega) = \frac{1}{\hbar\omega} W(\mathbf{k},\omega), \tag{1.23}$$

where $W(\mathbf{k},\omega)$ is the energy absorbed per unit k-space volume, frequency interval and path length of the fast electron.

Before calculating $W(\mathbf{k},\omega)$ for the thin metal film, the associated potential $U(\mathbf{k},\omega)$ must first be derived. This is achieved with linearized hydrodynamic Bloch equations and an assumption of irrotational motion. These equations are [13]

$$\gamma\psi + \frac{\partial}{\partial t}\psi = -\frac{e}{m}U + \frac{P\rho}{m\rho_0}, \tag{1.24a}$$

$$\frac{\partial \rho}{\partial t} = \rho_0 \psi, \tag{1.24b}$$

$$\nabla^2 U = 4\pi e[\rho + \delta(x - vt)\delta(y)\delta(z)], \tag{1.24c}$$

$$\nabla^2 U = 4\pi e\delta(x - vt)\delta(y)\delta(z). \tag{1.24d}$$

The first equation is the integral of the equation of motion, the second is the continuity equation, the third is Poisson's equation for the metal and the fourth is Poisson's equation in the vacuum. The damping is given by γ, the velocity potential is ψ and the fast electron velocity is v. The pressure change per unit number density is P/ρ_0 in the undisturbed gas.

To solve Eqs. (1.24) for U in a foil of thickness a in the x-direction, boundary conditions (BC) that state both field intensity and electric potential are continuous across the boundary and at the foil surface the normal velocity component vanishes are applied. It is also assumed that the incident electron is a lot faster than the conduction electrons, this is ensured by making the final term on the right hand side of Eq. (1.24a) small. By considering only the first order terms in $P/(\rho_0 m)$, U can be derived and its Fourier transform taken to give the total energy lost by the fast electron

$$W = e\frac{i}{(2\pi)^3}\int d\mathbf{k}\int d\omega k_x \delta\left(k_x + \frac{\omega}{v}\right) U(\mathbf{k},\omega), \tag{1.25}$$

where k_x is the component of the wavevector in the x-direction. To calculate the probability of a conduction electron transition occurring due to the fast electron

Eq. (1.25) is substituted into Eq. (1.23). The probability of a transition perpendicular to the fast electron velocity can then be calculated by splitting $\mathbf{k}$ into $k_\parallel$ and $k_\perp$ and integrating over k_x, where $k_\perp$ and $k_\parallel$ and the components of $\mathbf{k}$ that are perpendicular and parallel to the velocity vector of the fast electron. We can then split $P(k_\perp, \omega)$ into a term for the transition probability per unit foil thickness in an infinite foil $P_\infty(k_\perp, \omega)$ and for boundary effects $P_b(k_\perp, \omega)$. Thus, the total probability is

$$P(k_\perp, \omega) = aP_\infty(k_\perp, \omega) + P_b(k_\perp, \omega).$$

In the limit of large foil thickness this result is given by [12]

$$P(k_\perp, \omega) = \frac{e^2 a}{\hbar\pi^2 v^2}\left[\frac{\mathrm{Im}(1/\varepsilon)}{k_\perp^2 + \omega^2/v^2} - \frac{2k_\perp}{a(k_\perp^2 + \omega^2/v^2)^2}\mathrm{Im}\left(\frac{(1-\varepsilon)^2}{\varepsilon(1+\varepsilon)}\right)\right].$$

On substitution of the appropriate Drude dielectric function, the boundary effect is

$$P_b(k_\perp, \omega) = \frac{e^2}{\pi^2\hbar v^2}\frac{2k_\perp}{\left(k_\perp^2 + \frac{\omega^2}{v^2}\right)^2}\cdot\frac{\gamma\omega_p^4}{\omega} \cdot\left[\frac{\frac{1}{4}\omega_p^2}{(\omega^2 - \frac{1}{2}\omega_p^2)^2 + \gamma^2\omega^2} - \frac{\omega_p^2}{(\omega^2 - \omega_p^2)^2 + \gamma^2\omega^2}\right]. \tag{1.26}$$

The contents of the large square bracket are the key result, it shows the there are two resonances. The second term in this bracket is the bulk plasmon term, it shows that the boundary causes a decrease in the energy loss the fast electron feels due to excitation of plasmons. Concurrent with that reduced is the new term, the first term in the bracket, that states a loss will be felt by the fast electron at the *surface* plasmon frequency, given by

$$\omega_s = \frac{\omega_p}{\sqrt{2}}. \tag{1.27}$$

By decreasing foil thickness the strength of the bulk plasmon resonance reduces as the surface plasmon resonance increases. The shift in frequency occurs because a thin foil's surface will display the depolarizing effect [12]. That is, the applied field results in dipole ordering within the material. This order induced a field counter to the applied field causing a resonance at the interfaces of the foil at a lower energy than the bulk plasmon.

1.8 Polaritons

This section gives a discussion of the two cases of polaritons that are pertinent to the the RAO effect that was studied in this thesis. In general the polariton is a propagating mode of a given material that is a mixture of both an optical mode and some matter excitation.

1.8.1 TO-phonon Polaritons

The treatment of lattice vibrations in ionic crystals was the topic of a paper by Kun Huang in 1951, in it he proposed the extension of the then current electrostatic theory to include the remaining three Maxwell equations, that is Gauss Law and the two cross product equations [24]. This inevitably leads to a prediction of a mixed state between the lattice vibrations of an ionic crystal and any incident light field of resonant frequency.

In a second paper on the topic Huang gave a derivation of the mixed modes and relative energy of a spatially dispersionless mixed lattice state, for a two-ion, optically isotropic lattice [25, 26]. The starting point is the macroscopic equations for the motion of the charges in an ionic crystal

$$\ddot{\mathbf{w}} = -\omega_0^2 \mathbf{w} + \left(\frac{\varepsilon_0 - \varepsilon_b}{4\pi}\right)^2 \omega_0 \mathbf{E}, \tag{1.28a}$$

$$\mathbf{P} = \left(\frac{\varepsilon_0 - \varepsilon_b}{4\pi}\right)^2 \omega_0 \mathbf{w} + \frac{\varepsilon_b - 1}{4\pi} \mathbf{E}, \tag{1.28b}$$

where the dielectric polarization is $\mathbf{P}$ and the electric field is $\mathbf{E}$, ω_0 is called by Huang the frequency of the infrared dispersion and is the frequency of the lowest energy optical lattice vibration. Huang has also used a form of relative ionic displacement $\mathbf{w} = \mathbf{u}[(m_- + m_+)/V_0]^{1/2}$, where $\mathbf{u}$ is the relative ionic displacement, $m_{+,-}$ are the reduced masses of the ions and V_0 is the volume of unit lattice formed by the ion pair. The dielectric constants in these equations are the low frequency dielectric constant ε_0, measured when the electric field frequency $\omega << \omega_0$, and the high frequency dielectric constant ε_b measured when $\omega >> \omega_0$. These equations are then solved with

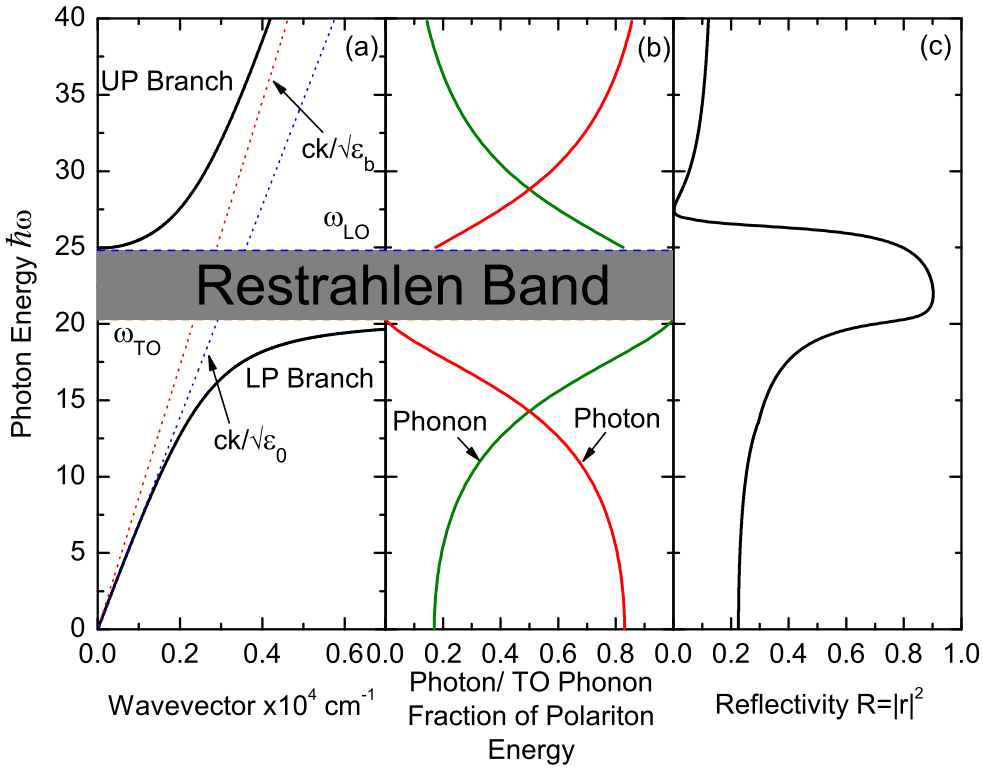

Figure 1.2: A schematic of (a) the dispersion, (b) the of the photon and phonon components and (c) the reflectivity of the TO-phonon polariton. The first panel includes the bare light dispersion for dielectric constant in the case $\omega \to 0$ (blue dashed line) and $\omega \to \infty$ (red dashed line).

Maxwell's equations

$$\nabla \cdot \mathbf{D} = 0, \tag{1.29a}$$

$$\nabla \cdot \mathbf{H} = 0, \tag{1.29b}$$

$$\nabla \times \mathbf{E} = -\frac{1}{c}\dot{\mathbf{H}}, \tag{1.29c}$$

$$\nabla \times \mathbf{H} = \frac{1}{c}\dot{\mathbf{D}}, \tag{1.29d}$$

where $\mathbf{D} = \mathbf{E} + 4\pi\mathbf{P}$ and $\mathbf{H}$ is the magnetic field.

The inclusion of all four of Maxwell's equations allows the calculation of propagating modes around the center of the Brillouin zone in ionic crystals. The five vibrational solutions to Eqs. (1.28) and Eqs. (1.29) consist of one longitudinal mode and four transverse. Including the retarded electric field leads to the transverse lattice modes coupling to it. The result is that all four transverse modes are mixed states between

lattice vibrations and the optical field, these are TO-phonon polariton modes. This result differs from the original electrostatic approximation, i.e. Eq. (1.29a) and $\nabla \times \mathbf{E} = 0$, . This serves as a first approximation for the modes that are valid for short wavelengths, far from the Brillouin zone center, where the polariton modes behave as if they are unretarded.

Fig. 1.2 (a) shows that the transverse mode of the lower polariton (LP) branch is approximated by the bare light mode, that is the optical mode which is considered uncoupled to the ionic lattice vibrations, $\omega = ck/(\varepsilon_0^{1/2})$. As the wavevector increases through the range the dispersion becomes an asymptote of the TO-phonon dispersion. This suggests that the degree to which a polariton is a mixed state is dependent on the polariton wavevector. This is more clearly demonstrated in Fig. 1.2 (b). The fraction of the energy in the polariton which is due to the lattice vibrational and due to transverse electric field is shown over a range of photon energy. This demonstrates that near to the restrahlen band the polariton has large amount of its energy as a lattice vibration, this is the region where no polaritons can propagate and the solution is purely due to lattice vibrations.

In the upper polariton (UP) branch, the polariton begins as approximating a pure transverse lattice vibration, and asymptotically approaches the bare light dispersion $\omega = ck/(\varepsilon_b^{1/2})$, which would exist if the ions where assumed to be fixed and the dielectric constant ε_b depended only on the electronic motion of the crystal. This is the reverse of the LP branch and is clearly demonstrated in Fig. 1.2 (b).

It should be noted that the longitudinal mode is a pure lattice vibration because the light field is transverse, and therefore does not usually couple to lattice vibrations. This solution can be obtained from either the electrostatic approximation or the Maxwell's equations methods.

The result on the optical properties of the system, due to the mixed mode propagation of light through the ionic material, is that at the frequencies at which the lattice mode character is dominant no optical propagation occurs. This leads to to the characteristic optical stop gap that is present in all polariton supporting lattices. This effect is clearly seen in Fig. 1.2 (c), which shows the polariton reflectivity, rotated through a right angle for easier comparison with the dispersion of Fig. 1.2 (a).

A more convenient method of expressing the polar motion of an ionic crystal using macroscopic equations was suggested in 1958 by J. J. Hopfield in his study of

light absorption in dielectrics [27]. His study was of the role of exciton polaritons in optical absorption, which was later expanded to include spatial dispersion of exciton polaritons [28]. In both papers, the macroscopic equation for the polarization field associated with an undamped, spatially dispersionless polariton in an optically isotropic dielectric was given as

$$\left(\frac{\partial^2}{\partial t^2} + \omega_0^2\right)\mathbf{P} = \frac{\varepsilon_b \omega_c^2}{4\pi}\mathbf{E}, \tag{1.30}$$

where ω_0 is the frequency of an undamped TO-phonon polariton.

By solving this equation and Maxwell's wave equation in a polarizable medium

$$\left(\frac{\varepsilon_b}{c^2}\frac{\partial^2}{\partial t^2} - \frac{\partial^2}{\partial x^2}\right)\mathbf{E} = -\frac{4\pi}{c^2}\frac{\partial^2}{\partial t^2}\mathbf{P},$$

with a plane wave electric field and polarization the dispersion equation of the undamped TO-phonon polariton can be derived. This can be expressed as

$$\frac{k^2c^2}{\omega^2} = \left(1 + \frac{\omega_c^2}{\omega_0^2 - \omega^2}\right)\varepsilon_b \tag{1.31}$$

and is the equation used to calculate the dispersion given in Fig. 1.2 (a).

The dispersion can also be calculated by using the Hopfield Hamiltonian as a starting point [27]. It is expressed here in terms of the photon creation and annihilation operators $c_{\mathbf{k}}^\dagger$,$c_{\mathbf{k}}$ and the polarization equivalent $b_{\mathbf{k}}^\dagger$,$b_{\mathbf{k}}$ [27, 29],

$$\begin{aligned} H_{pol} = \sum_{\mathbf{k}} \Big[& \hbar ck\ c_{\mathbf{k}}^\dagger c_{\mathbf{k}} + \hbar\omega_0\ b_{\mathbf{k}}^\dagger b_{\mathbf{k}} + iB_{\mathbf{k}}\ (c_{\mathbf{k}}^\dagger b_{\mathbf{k}} - c_{\mathbf{k}} b_{\mathbf{k}}^\dagger + c_{-\mathbf{k}} b_{\mathbf{k}} - c_{-\mathbf{k}}^\dagger b_{\mathbf{k}}^\dagger) \\ & + D_{\mathbf{k}}\ (c_{\mathbf{k}}^\dagger c_{\mathbf{k}} + c_{\mathbf{k}} c_{\mathbf{k}}^\dagger + c_{-\mathbf{k}} c_{\mathbf{k}} + c_{-\mathbf{k}}^\dagger c_{\mathbf{k}}^\dagger)\Big] \end{aligned} \tag{1.32}$$

where,

$$B_{\mathbf{k}} = \hbar\omega_0\sqrt{\frac{\varepsilon_b\omega_c}{4\omega_0 kc}}$$

and

$$D_{\mathbf{k}} = \hbar\frac{\varepsilon_b\omega_c}{4kc}.$$

The Hamiltonian given here is for a mixed state of photon and polarization, this is

the polariton.

1.8.2 Surface Plasmon Polaritons

It has been previously established that confinement of plasmons to thin films led to the red shifting of the resonant energy of the plasmon [Eq. (1.27)], which is now called the surface plasmon with a resonant frequency ω_s. For the in-plane surface plasmon wavevectors $\mathbf{k}$ in the range $\omega_s/c << k << \omega_f/c$, where ω_f is the Fermi frequency, $\omega(\mathbf{k})$ is only weakly dispersive. This is the nonretarded regime, where the discrepancy between the surface plasmon phase velocity and light velocity is sufficiently great that the light velocity can be considered infinite. Any surface plasmon in this wavevector region can be consider only weakly dispersive. The retarded region is $k < \omega_s/c$ where the plasmon velocity and the vacuum speed of light are comparable. In this region the optical field and the plasmon couple, this results in a surface plasmon polariton. This section of the introductory chapter is a description of the SPP.

The excitation of surface plasmons by light is possible but a pair of criteria must be fulfilled before this occurs. The most general, is that for any propagating transverse surface wave to be excited by light, there must be an electric field component that is normal to the surface in which the wave is to be excited. The solutions to Maxwell's equations [Eqs. (1.29)] can be split into two possible polarizations in which either the electric field is parallel to the interface or the magnetic field is, these are known as s-polarised [transverse electric (TE)] and p-polarized [transverse magnetic (TM)] waves, respectively. The p-polarised solution consists of a magnetic field component parallel to the interface and two electric field components, one parallel and the perpendicular. In the case of a field confined to a flat surface at $z = 0$ the p-polarised solutions are

$$\mathbf{E}_i = \begin{pmatrix} E_{i_x} \\ 0 \\ E_{i_z} \end{pmatrix} e^{-\kappa_i |z|} e^{i(k_i x - \omega t)}, \tag{1.33a}$$

$$\mathbf{H}_i = \begin{pmatrix} 0 \\ H_{i_y} \\ 0 \end{pmatrix} e^{-\kappa_i |z|} e^{i(k_i x - \omega t)}, \tag{1.33b}$$

where κ_i is the decay constant along z and the subscript defines the material.

There are no s-polarised surface oscillations [13]. For surface oscillations to be generated it is required that the electric field has a component perpendicular to the surface. In only the p-polarised case does this happen, therefore only p-polarised light can generate surface plasmon polaritons.

It is necessary for surface plasmons that the decay of the associated light field into each medium are equal and opposite [13]. This requirement leads to the surface plasmon condition

$$\frac{\varepsilon_1}{\kappa_1} + \frac{\varepsilon_2}{\kappa_2} = 0, \tag{1.34}$$

where ε_i is the dielectric function in each semi-infinite medium. By using Eqs. (1.33) in Maxwell's equations (Eqs. (1.29)) with $\mathbf{D} = \varepsilon_i \mathbf{E}$ we can show that

$$\kappa_i = \sqrt{k^2 - \varepsilon_i \left(\frac{\omega}{c}\right)^2},$$

where, because the boundary condition require the in plane wavevector to be continuous across the interface, $k = k_1 = k_2$. By using this Eq. (1.34) the surface plasmon condition becomes

$$k(\omega) = \frac{\omega}{c}\sqrt{\frac{\varepsilon_1 \varepsilon_2}{\varepsilon_1 + \varepsilon_2}}. \tag{1.35}$$

Finally, for a simple Drude metal in a vacuum

$$\varepsilon = 1 - \frac{\omega_p}{\omega(\omega + i\Gamma)},$$

where the damping is given by Γ. By using this in the surface plasmon condition Eq. (1.35) the dispersion relation can be derived as

$$\frac{k^2 c^2}{\omega^2} = \frac{\omega(\omega + i\Gamma) - \omega_p^2}{2\omega(\omega + i\Gamma) - \omega_p^2}. \tag{1.36}$$

In Fig.1.3 the SPP dispersion is shown for $\Gamma = 0$.

The upper red solid line in Fig. 1.3. is the dispersion of the light field in the bulk of the metal. Due to the highly absorptive nature of metal it is of little interest for optical manipulation. The lower blue solid line is the dispersion of the SPP and is

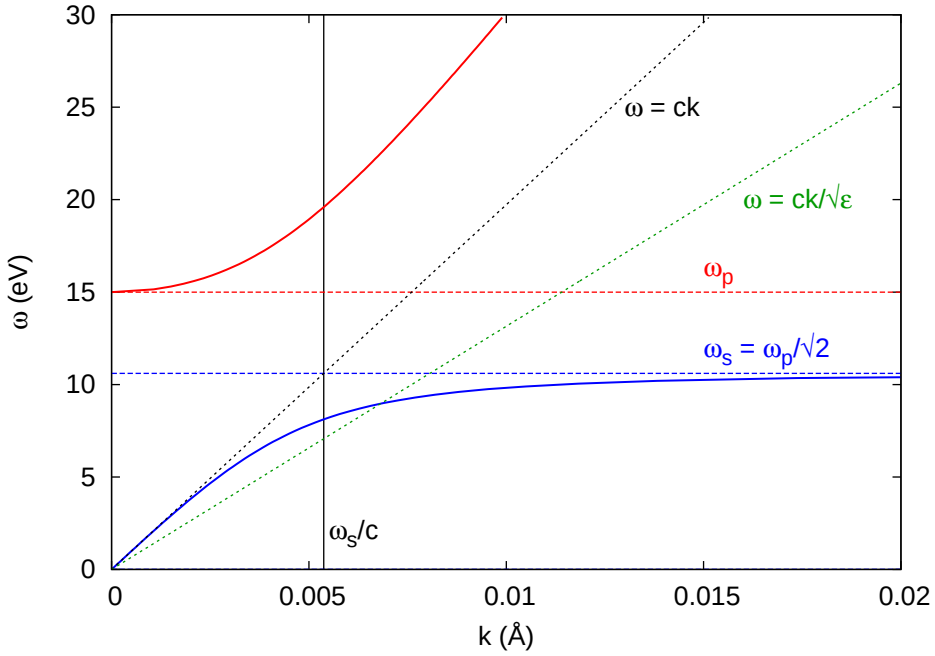

Figure 1.3: A dispersion for a surface plasmon of energy $\hbar\omega_p = 15$ eV, compared with the bare light dispersion for $\Gamma = 0$. The solid blue line is the SPP dispersion and the dashed blue line is Ritchie's surface plasmon frequency ω_s [Eq. (1.27)]. The solid red line is the dispersion of light in the bulk of the metal and the dashed red line is the polariton frequency ω_p [Eq. (1.16)] given by Pines and Bohm. The dashed black line is the vacuum light line and the dashed green line is the light for the prism ATR coupler.

given by

$$\omega^2(k) = \frac{\omega_p^2}{2} + c^2k^2 - \sqrt{\frac{\omega_p^4}{4} + c^4k^4}, \tag{1.37}$$

and displays interesting behavior in two separate regions [13]. The first region occurs when $k < \omega_s/c$, which is the region left of the thin black line in Fig. 1.3. Below this k-value is the retarded region and the polariton nature of light propagation is dominant. The second region occurs when $k >> w_s/c$, the dispersion asymptotically approaches Ritchie's surface plasmon frequency, where no plasmon-light coupling occurs.

At no point along the SPP dispersion is there an intersection with light line ωk. Physically, this is because the wavevector found in Eq. (1.37) is for a 2D mixed state in the plane of the surface, due to the lack of a propagating mode in the z-direction. This conclusion leads to the second of the two criteria needed to optically excite the SPP. As light incident on the surface of a metal cannot have the correct

dispersion properties to excite an SPP, the dispersion relation must be modified. This can be achieved in two ways, either through imparting extra momentum via the *umklapp* processes associated with scattering of gratings or some other roughness [30], or through the manipulation of the light dispersion via an attenuated total reflection (ATR) coupler, which excites the plasmon from the substrate side [31]. In this thesis the scattering method is used.

1.9 Resonant Acousto-Optic Effect

The optical, dynamical or AC Stark effect has been known for some time, in general it causes an excitation state of a given medium to split in to multiple states via an oscillating perturbation [32]. The optical Stark effect was observed in crystalline materials via the coupling of two exciton-polariton states in Cu_2O crystals [2] and GaAs multiple quantum wells (MCW) [3]. The later experiment pumped the exciton well away from their resonance with a laser pulse, yet transmittance spectra of the much weaker probe pulse was modified due to this pumping. The pump pulse causes internal transitions of exciton polaritons formed by the probe pulse [3, 4].

In 2001 Ivanov and Littlewood proposed to use an acoustic wave (AW) as part of an improved scheme to study the dynamical Stark effect [1]. They proposed a scheme in which the pumping laser pulse of the optical Stark effect is replaced by an acoustic wave, the exciton polaritons are still formed by the weak probe beam. The proposed acoustically induced Stark effect was to remove the many-body effects associated with laser pumped equivalent. The weak probe pulse is not strong enough for many body effects to be a concern. In 2003 this idea was generalised to include microcavity polaritons. In this case, quantum well (QW) excitons formed polaritons with microcavity (MC) photons, which were in turn modulated by a collinearly propagating SAW [5].

The dynamical Stark effect that is parametrically driven by a coherent AW is the RAO effect. In both exciton case and the microcavity polariton case mentioned in Section 1.2, the intensity of the AW controls the splitting of the probed states. The term “resonant” in the acronym RAO refers to fact that, unlike *conventional* acousto-optics, the coherent acoustic wave is resonantly coupled to the solid state excitation. In the two cases previously mentioned these excitations are two separate case of exciton. The matter excitation must be optically “dressed”, i.e a polariton, to allow the AW to modulate the light field. This gives rise to a picture of the solid

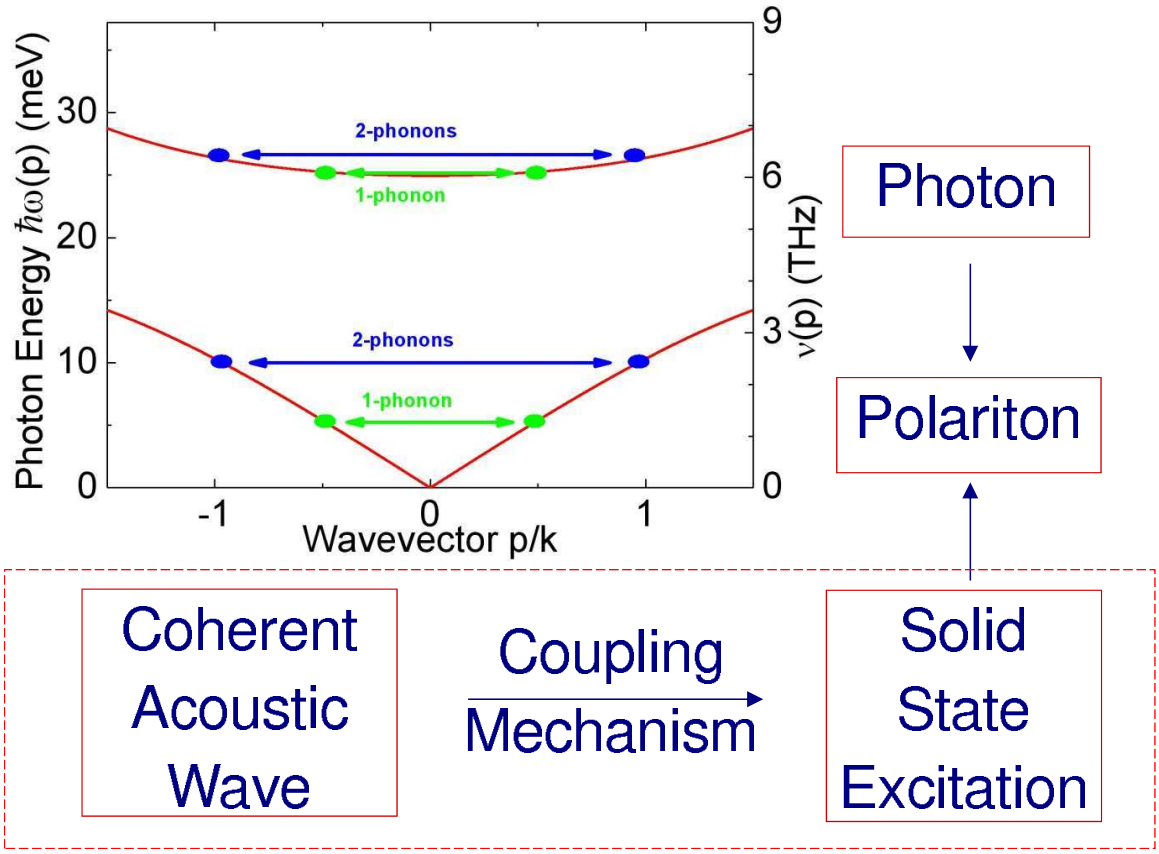

Figure 1.4: A schematic representation of the RAO effect as a physical process and the effect it has on the polariton dispersion

state excitation resonantly enhancing the acousto-optic interaction. The schematic in Fig. 1.4 represents this process, the matter component of the polariton mediating the interaction between light and sound. The arrows in the bare polariton dispersion show the acoustic coupling of two states of the solid state excitation and are equal to the phonon wavevectors. In Fig. 1.4the polariton frequency is $\omega = \nu/(2\pi)$, the polariton wavevector is p and the acoustic wavevector is k.

The acoustically induced transitions of the solid state component of the polariton, at the points in the dispersion resonant with AW, result in the opening of band gaps in the dispersion at those resonant points. Like the main polariton restrahlen band these acoustically induced band gaps are regions in which no polaritons can propagate. This has a strong effect on the optical properties of the material in which the RAO effect is occurring, for example the total reflectivity spectrum shows very pronounced peaks at the spectral position of the acoustically induced band gaps. An example is shown in Fig. 1.5. The color of the arrows corresponds to the order of the TO-phonon transition given in dispersion of Fig. 1.4.

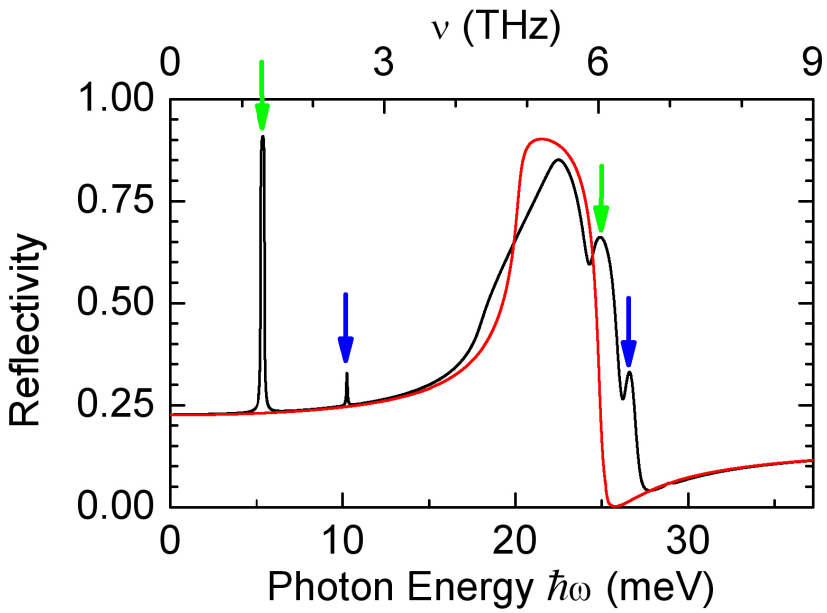

Figure 1.5: A figure to show the results of the RAO effect on the reflectivity spectrum in CuCl

The periodicity of the AW used to modulate the polarization field in the material leads to an acoustically induced superlattice. The periodicity determines the spectral position of the acoustically induced band gaps, which occurs at $p \simeq \pm nk/2$ where n is an integer. Like its crystalline analogue, this acoustically induced band structure can be probed using Bragg scattering through the manipulation of the angle of incidence of a probe light field [6, 7]. In 2006 this technique was used to experimentally investigate and confirm the existence of the RAO effect for microcavity polaritons [8].

The polariton involved in an RAO effect constitutes strong coupling between the photon and the solid state excitation, however for an RAO effect to occur it is necessary that the coupling of the acoustic field to the polarization be just as strong. Thus, they must be treated on an equal footing [6]. For the cases of excitons and microcavity polaritons discussed above the coupling associated with the AW comes from both the deformation potential and the piezoelectric matrix element.

The deformation potential is the potential generated by the deformation of the unit cell of a crystalline material due to the time dependent strain of a non-zero wavevector acoustic phonon. It relates the volume dilation of a given volume of the crystalline medium to an energy shift of an electronic energy band [33]. This is the dominant coupling mechanism for the AW to exciton coupling in exciton polariton and MC polariton RAO effect when a purely longitudinal acoustic wave is used [11]. This

is because the dilation of the crystalline volume due to a purely longitudinal AW is sufficiently symmetric that stress induced by a macroscopic electric field is small.

The piezoelectric interactions is a stress induced macroscopic electric field in a noncentrosymmetric crystal or, equivalently, a strain induced electric field. For sufficiently small strains the relationship between the induced electric field and the strain is linear and given by the third order electromechanical tensor [33]. A transverse AW in the exciton or MC polariton RAO effect would lead to the piezoelectric interaction being the dominant one for AW to exciton coupling [11]. The transverse AW would cause a small asymmetric deformation of the crystalline structure leading to the piezoelectric coupling between AW and exciton.

This thesis studies two examples of the RAO effect, one is associated with TO-phonon polaritons and the other with SPPs. This first case uses TO-phonons as the polarization field providing the strong coupling to light and was initially proposed by Ivanov in 2007 [11]. This limits the possible media in which this case of the RAO effect is manifest, for polariton formation of this type to occur the medium must be an ionic crystal. The coupling between the AW and the TO-phonon component of the polariton occurs via the anharmonic components of the interatomic potential of the medium in which the RAO effect takes place. Specifically, the third and fourth order terms of the Taylor expansion of the interatomic potential are important for the coupling of the TO-phonon to the transverse acoustic (TA) phonons of the AW in the RAO effect. With this mind the materials used are CuCl, TlCl and $LiNbO_3$ where the third order term is strong for CuCl, the fourth order for TlCl and both are relevant for $LiNbO_3$.

The second case that will be studied in this thesis uses SPPs as the polarization field in thin metal foils. Due to the strong attenuation properties of light it is necessary to restrict the thickness of the metal. The SAW deforms the metal film periodically, similar to the grating method of light-SPP coupling. The grating is used to impart momentum to surface plasmons via umklapp processes to couple it to propagating photon states. This will result in an acoustically induced Brillouin zone and the corresponding peaks in the reflectivity. For the RAO effect the wavelength of the AW can selected so that instead of coupling SPPs to photon states, they are coupled to other SPPs of the same wavevector magnitude but with opposite sign.

1.10 Summary

This chapter has introduced the concept of the RAO effect and discussed the required background knowledge. The recent advances in the field of resonant acousto-optics were outlined. Introducing the RAO effect by starting with the original case of bulk exciton polaritons and microcavity polaritons. The coupling mechanism of the TO-phonon polariton RAO effect, the anharmonic crystalline potential, was then discussed. This was followed by the solid state excitation associated with the RAO effect in metals, which is the surface plasmon. Polaritons were then introduced as a coupled light-matter component of the RAO effect.

The following chapters will discuss the RAO effect for TO-phonons with either one anharmonic term considered as the coupling mechanism or two. The RAO effect for thin metal films will also be discussed, where SPPs are the matter excitation coupled to the AW via Bragg scattering processes.

2 Resonant Acousto-Optics with TO-Phonons: One Anharmonic Term in the Lattice Potential

For TO-phonon polaritons the RAO effect is the coupling of a photon and acoustic phonon mediated by TO-phonon, as discussed in section 1.9. The key to this interaction is the anharmonic coupling between the two phonon branches. This chapter will separately discuss the nature of the interaction between an acoustic phonon and TO-phonon due to cubic and quartic anharmonicities of an interatomic potential. The results of numerical simulations of the RAO effect, based on a modification of Hopfield's macroscopic equation of the polariton, will be shown in this chapter. For the cubic anharmonicity, a comparison of the numerical results will be made with analytic calculations for low intensity acoustic waves, with good agreement.

2.1 Theoretical Background

In section 1.9 a brief discussion of the RAO effect and it's development was presented. In this section detailed background theory for the case of RAO effect of TO-phonon polaritons will be given for a general ionic crystalline material. The most general form

of the macroscopic equations, used in this thesis to model the RAO effect, are [34, 35]

$$\left[\frac{\varepsilon_{\mathrm{b}}}{c^2}\frac{\partial^2}{\partial t^2} - \nabla^2\right]\mathbf{E}(\mathbf{r},t) = -\frac{4\pi}{c^2}\frac{\partial^2}{\partial t^2}\mathbf{P}(\mathbf{r},t), \tag{2.1a}$$

$$\left[\frac{\partial^2}{\partial t^2} + 2\gamma_{\mathrm{TO}}\frac{\partial}{\partial t} + \omega_0^2 + 4\omega_0\sigma_4 + 4\omega_0\sigma_3\cos(\Omega t - \mathbf{Kr} + \phi)\right.$$
$$\left. + 4\omega_0\sigma_4\cos(2\Omega t - 2\mathbf{Kr})\right]\mathbf{P}(\mathbf{r},t) = \frac{\varepsilon_{\mathrm{b}}}{4\pi}\omega_{\mathrm{R}}^2\mathbf{E}(\mathrm{r},t). \tag{2.1b}$$

The electric and TO-phonon polarization fields are $\mathbf{E}$ and $\mathbf{P}$, the TO-phonon frequency is ω_0, the polariton Rabi frequency is $\omega_R = \sqrt{\omega_{\mathrm{LO}}^2 - \omega_0^2}$, where ω_{LO} is the longitudinal optical (LO) phonon frequency. The dielectric background constant is ε_b. The TO-phonon mainly decays into short wavelength acoustic phonons, this is included by the damping constant γ_{TO}. The cosine terms model the oscillatory nature of the bulk acoustic wave to which TO-phonon polariton is anharmonically coupled. The cosine with σ_3 as a prefactor has the acoustic wavevector $\mathbf{K}$ and the acoustic frequency Ω as arguments because the anharmonic coupling is a one phonon process only in the cubic scattering channel. This is in contrast to the quartic coupling term, which has an extra factor of 2 in the cosine argument due to the two-phonon process which couples the TO-phonon polariton to the acoustic wave via the quartic channel. The term ϕ is a phase difference between the two oscillating terms.

This thesis considers only an AW with linear dispersion properties $\Omega = v_{ac}K$, where v_{ac} is the acoustic velocity. The strength of the coupling between the TO-phonon component of the polariton and the AW is given by $\sigma_{3,4}$. The subscript refers to the order in the anharmonic potential that is responsible for the interaction. The coupling strength is also dependent on the intensity of the AW I_{ac}, the exact relationship varies for each anharmonic term of the Taylor expansion. For the anharmonicities investigated in this thesis the relationships are as follows:

$$\sigma_3 \propto \sqrt{I_{\mathrm{ac}}}; \tag{2.2a}$$

$$\sigma_4 \propto I_{\mathrm{ac}}. \tag{2.2b}$$

A full discussion of the relationship between the coupling constant and I_{ac} will be given in the next chapter, where the relationship between the two anharmonic components is discussed.

Due to the propagating nature of the periodicity introduced by the AW, the solutions of Eqs (2.1) can be expressed as a Fourier series, which simultaneously accounts for

both temporal and spacial modulation,

$$E(z,t) = e^{i(kz-\omega t)} \sum_n E_n e^{in(Kz-\Omega t)}\,, \tag{2.3a}$$

$$P(z,t) = e^{i(kz-\omega t)} \sum_n P_n e^{in(Kz-\Omega t)}\,. \tag{2.3b}$$

where $\omega = 2\pi\nu$ and k are the frequency and wavevector of the light field, respectively. The substitution of Eqs. (2.3) into Eqs. (2.1) leads to an eigenvalue problem

$$\left[(k+nK)^2 - \frac{\varepsilon_b}{c^2}(\omega+n\Omega)^2\right] E_n = \frac{4\pi}{c^2}\,(\omega+n\Omega)^2 P_n, \tag{2.4a}$$

$$\left[\omega_0^2 + 4\omega_0\sigma_4 - 2i\gamma(\omega+n\Omega) - (\omega+n\Omega)^2\right] P_n$$

$$+2\sigma_3\omega_0(P_{n+1}e^{-i\phi} + P_{n-1}e^{i\phi}) + 2\sigma_4\omega_0(P_{n+2}+P_{n-2}) = \frac{\varepsilon_b\,\omega_R^2}{4\pi}\,E_n. \tag{2.4b}$$

The Chapters 2 and 3 deal with eigenvalues $\omega(k)$ and $k(\omega)$ and eigenvectors E_n and P_n of this problem. The calculation of the reflectivity and extinction associated with these results for a semi-infinite geometry is also important to the investigation of the RAO effect. These calculations are also found in Chapters 2 and 3.

In general the matrix problem in Eqs (2.4) is complex, therefore both $\omega(k)$ or $k(\omega)$ are, generally, complex even when $\gamma = 0$. The calculation of these two forms of the dispersion are performed by either supplying real valued k to calculate the quasi-energy spectrum $\omega(k)$ or by providing real valued ω to calculate the quasi-momentum spectrum $k(\omega)$. From this latter calculation the optical properties, such as reflection and transmission, of an AW driven TO-phonon polaritons can be obtained.

The Hamiltonian for a system of acoustically driven far infrared polaritons is

$$H = H_{\rm pol} + \hbar\sum_{\mathbf{p}} \Big[4\sigma_4 b^\dagger_{\mathbf{k}} b_{\mathbf{k}} + (\sigma_3 e^{-i\Omega t} b^\dagger_{\mathbf{k}} b_{\mathbf{k}-\mathbf{K}} + \text{H.C.}) +$$

$$(\sigma_4 e^{-2i\Omega t} b^\dagger_{\mathbf{k}} b_{\mathbf{k}-\mathbf{2K}} + \text{H.C.})\Big]\,, \tag{2.5}$$

where $H_{\rm pol}$ is the Hopfield polariton Hamiltonian (Eq.(1.32)) given in section 1.8. Some properties of the RAO effect can be calculated using this Hamiltonian. However, in this thesis all calculation where made using the macroscopic equations, Eqs. (2.1) and the Hamiltonian is included for completeness only.

Table 2.1: Parameters for bulk CuCl and TlCl used in the calculations presented in this chapter (* ∼4 K †room temperature).

	CuCl	TlCl
$\hbar\omega_0$ (meV)	20.28	7.81
$\hbar\omega_R$ (meV)	14.53	17.97
ε_b	5.22	5.1
$\hbar\gamma$ (meV)	0.02^*	$0.92^\dagger$

2.2 Numerical Model

The numerical model presented in this section is for the coupling due to third order anharmonicity, the coupling constant σ_4 is set to zero in Eqs. (2.1). Initially, the eigenvalues $\omega(k)$ are calculated and the dispersion investigated, this is then followed with the calculation and investigation of eigenvalues $k(\omega)$. In both case, the translational properties of the acoustically induced branches are important to further calculation. It should be noted that the model presented here is also used in Section 2.5 when σ_4 is non-zero and $\sigma_3 = 0$. The case of nonzero σ_3 and σ_4 is discussed in Chapter 3

2.2.1 Quasienergy Spectrum

The quasienergy spectrum $\omega(k)$ is, for nonzero damping, a complex quantity dependent on real valued k in an unbound semiconductor. It shows the permitted values of ω for any given real value of k propagating TO-phonon polaritons can take when acoustically driven. At band-gaps the values of $\omega(k)$ become purely imaginary, which corresponds only to decaying solutions of Eqs. (2.1). For the purpose of studying the RAO effect it is useful to consider the propagating polariton solutions only. This can be achieved by setting the $\gamma = 0$ and considering the real part of $\omega(k)$. In this context, the rather idealised $\omega(k)$ can be used to investigate the effects that the AW driving has on the propagating TO-phonon polaritons. Even in this case however there are still regions where $\mathrm{Im}[\omega(k)] \neq 0$, at these frequencies acoustically induced band gaps form. These will be discussed later. This subsection presents a comparison between the AW driven quasienergy branches and the bare TO-phonon polariton dispersion, which corresponds to the situation where both $\sigma_3 = 0$ and $\sigma_4 = 0$ in Eqs. (2.1).

To consider only the third order coupling between the AW and the TO-phonon component of the polariton, we put that $\sigma_4 = 0$. In this case ϕ in Eqs. (2.4) becomes arbitrary and so it is removed along with the σ_4 terms. Equation (2.4b) is then reduced to

$$\left[\omega_0^2 - (\omega + n\Omega)^2\right] P_n + 2\sigma_3\omega_0(P_{n+1} + P_{n-1}) = \frac{\varepsilon_b\,\omega_R^2}{4\pi}\,E_n. \tag{2.6}$$

This can be solved, along with Eq. (2.4a), as an eigenvalue problem for the polariton eigenfrequency $\omega = \tilde{\omega}_\lambda$. The subscript refers to the energy bands $\lambda = 1, 2, \ldots$, which are separated by acoustically induced band gaps. The eigenvalue problem itself can be put into linear form for ease of calculation, this is done in Appendix A.1 in the presences of both cubic and quartic anharmonicity. For the case of cubic anharmonicity only ($\sigma_4 = \phi = 0$), the result is

$$\hat{\mathbb{W}}\vec{\mathbb{X}} = \tilde{\omega}\vec{\mathbb{X}}. \tag{2.7}$$

For the calculation of $\tilde{\omega}$ to take place Eq. (2.7) must be truncated at $-n_r \leq n \leq n_r$. This introduces the matrix dimension $M = 2n_r + 1$. Thus, the dimensions of the $\tilde{\omega}$-independent matrix $\hat{\mathbb{W}}$ are $4M \times 4M$. The vector $\vec{\mathbb{X}}$ is $4M$ in length and contains the electric field's Fourier components. The factor of 4 in the matrix dimension M comes from the fact that the polariton dispersion is split between the UP and LP branch, which gives a factor of 2. The positive and negative pairs that all eigenfrequencies come in provides the other factor of 2. Due to the periodic nature of the AW in both space and time, each branch of the quasienergy dispersion has the translational property

$$\tilde{\omega}_\lambda(k + sK) = \tilde{\omega}_\lambda(k) + s\Omega. \tag{2.8}$$

The eigenfunctions that correspond to each branch $\omega_\lambda(k)$ also obey a similar property

$$E_n(k + sK) = E_{n+s}(k). \tag{2.9}$$

An expression of the same form exists for P_n.

The quasienergy spectrum of AW driven polaritons is shown in Figure 2.1 for CuCl, the units of the x-axis are the acoustic wavevector K. It is due to the periodicity in both space and time, caused by the driving AW, that the first acoustically induced Brillouin zone contains the folded bare polariton dispersion. This is then translated

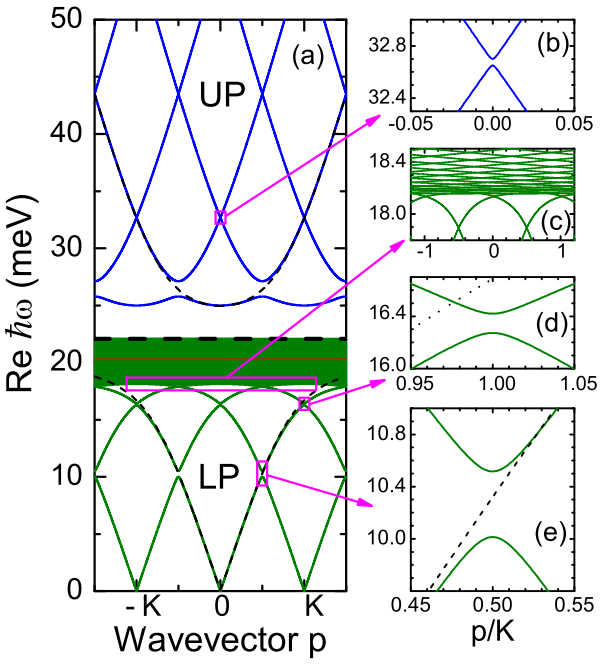

Figure 2.1: The quasienergy spectrum of both the UP (blue) and LP (green) branches of a bulk undamped TO-phonon polariton in CuCl. The polariton is driven by an AW with $\nu = 100$ MHz ($K = 0.3109\ \mu\text{m}^{-1}$) and an acoustic intensity corresponding to $\sigma = 1$ meV. The acoustically unexcited spectrum is given by the thin dashed lines and the heavy dashed line show the artificial cutoff of the LP quasicontinuum. Panels (b)-(e) show ares of the spectrum that are heavily modified by the acoustic wave.

by both nK and $n\Omega$, where n labels the order of the Bragg replica, into the other acoustically induced Brillouin zones. At the center and boundary of these zones band gaps open in the quasienergy spectrum, due to the coupling between the AW and the polaritons. These band gaps are highlighted in Figures 2.1(b), 2.1(d) and 2.1(e). In these spectral regions polariton propagation is *not* permitted, this has a large impact on the optical properties of the polaritons, e.g. the light reflectivity and Bragg scattering. In general the position of the band gaps is dependent on Ω. The width is dependent on both Ω and the coupling strength of the AW to the polariton. This is discussed in more detail later in this chapter.

In the regions in which polariton propagation *is* permitted, the acoustically altered spectrum deviates from the bare polariton spectrum. This is clearly seen in Figure 2.1(d) and 2.1(e), where the dashed line is the bare dispersion $\omega^{(0)}(k)$. It is clear from these insets that not only is there deviation but that it gets larger as $\omega \to \omega_0$. Around the TO-phonon resonance the deviation is dramatic. The reason for this is that the bare LP branch of the polariton spectrum has an upper bound of the TO-phonon frequency, which it approaches asymptotically. However, the acoustically modified LP branch spectrum does not behave in the same way around the TO-phonon frequency, this can be clearly seen in Figure 2.1 (a). The red line is set at ω_0 and clearly demonstrates that the degree of anti-crossing around the lower Restrahlen band edge when the TO-phonon polariton is acoustically driven, which is shown in Figure 2.1 (c), pushes states into the Restrahlen band. In principle the

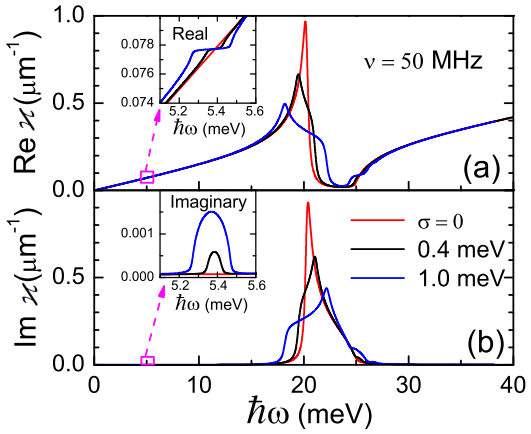

Figure 2.2: The (a) real and (b) imaginary part of the quasimomentum of the central Bragg replica of acoustically driven TO-phonon polaritons, for a variety of coupling strengths between the AW and TO-phonon. The insets show the effect of the AW on the polariton quasimomentum for the lowest acoustic band gap. The damping of the TO-phonon is $\gamma = 0.2$ meV and the acoustic frequency is $\nu = 50$ MHz ($K = 0.1555\ \mu\text{m}^{-1}$).

quasi-continuum states continue over the whole range examined here, however the contribution they make to the reflectivity of the acoustically driven TO-phonon polaritons drops very rapidly away from ω_0. It should also be noted that around ω_0 the Bragg condition at which the band gaps appear breaks down, due to the excessive anti-crossing and level repulsion.

2.2.2 Quasimomentum Spectrum

For an ionic material undergoing the RAO effect an incident light field of frequency ω excites TO-phonon polariton modes in the bulk of the material. For the given frequency of incident light, the polariton mode has a specific value of complex momentum $k = \tilde{\kappa}_j(\omega)$. These values are known in the literature as as forced harmonic solutions [36] and are calculated from Eqs. (2.4) by solving the inverse problem to that solved in the previous section. Thus, $\tilde{\kappa}_j(\omega)$ are complex eigenvalues. The associated eigenvectors also gain an index becoming E_{nj} and P_{nj}. This extra index has the range $-\infty \leq j \leq \infty$ and distinguishes the different partial waves. The unique partial wave composition of the total electric and polarization fields is determined by the boundary conditions. However, these partial waves are not independent. The eigenvalues and eigenvectors obey the translational relations that are analogous to those given in Eqs. (2.8) and (2.9)

$$\tilde{\kappa}_{j+s}(\omega) = \tilde{\kappa}_j(\omega - s\Omega) + sK, \tag{2.10a}$$

$$E_{n,j+s}(\omega) = E_{n+s,j}(\omega - s\Omega), \tag{2.10b}$$

$$P_{n,j+s}(\omega) = P_{n+s,j}(\omega - s\Omega). \tag{2.10c}$$

These relations invariably follow from the periodicity of both space and time caused by the passage of the AW.

The calculation of the complex quasimomenta $\tilde{\kappa}_j(\omega)$ begins at the same point as the quasienergy spectrum, with Eq. (2.6). From this we can arrive at a linear eigenvalue problem

$$\hat{\mathbb{V}}\vec{\mathbb{Y}} = \tilde{\kappa}\vec{\mathbb{Y}},$$

the full derivation of which is given in the second section of Appendix A.2 where both cubic and quartic anharmonicity are considered. To derive the quasimomentum eigenvalue problem for the case of third order anharmonicity only, σ_4 is set to zero in Appendix A.2. To calculate the quasimomentum spectrum it is necessary that the problem is truncated to $-n_r \leq n \leq n_r$, which makes $\hat{\mathbb{V}}$ a square $2M \times 2M$ matrix and the vectors $\vec{\mathbb{Y}}$ have $2M$ elements. The factor of 2 is due to the symmetry $\mathrm{Im}[\tilde{\kappa}] \rightarrow -\mathrm{Im}[\tilde{\kappa}]$. The reason for only one factor of two in the matrix and vector dimensions for the quasimomentum problem is the lack of separation into UP and LP branches. This is due to the fact that while the real polariton wave falls to zero for both $\gamma = 0$ and $\sigma_3 = 0$, the imaginary part becomes non-zero because the polariton solution is evanescent in Restrahlen band. For the more realistic case of a non-zero γ the real part retains some small non-zero value, this is shown by the red line in Figure 2.2.

When calculating the quasimomentum eigenvalues the matrices have to remain finite, to ensure this it is necessary to truncate the matrices. At these truncation points the quasimomentum Bragg replicas are badly distorted, the translational relations Eqs. (2.10) can be used to solve this problem. First the central root $\varkappa = \tilde{\kappa}_{j=0}(\omega)$ is selected. This is defined as the root which satisfies $\varkappa(0) = 0$. The translational property given by Eq. (2.10a) can be exploited to use $\varkappa$ to replace the other roots. It is then necessary to use a linear interpolation scheme, this is because the AW introduces an offset between frequency points in adjacent roots. Thus, $\omega_i \leq \omega - j\Omega \leq \omega_{i+1}$ and the linear interpolation is

$$\tilde{\kappa}_j(\omega) = \varkappa(\omega_i) + \frac{\varkappa(\omega_{i+1}) - \varkappa(\omega_i)}{\omega_{i+1} - \omega_i}(\omega - j\Omega - \omega_i). \tag{2.11}$$

After applying this interpolation any truncation issues are removed. To calculate $\varkappa(\omega)$ with minimal truncation effects present it is necessary to use fairly large matrices. The size for any given calculation depends on the coupling strength, for the separate

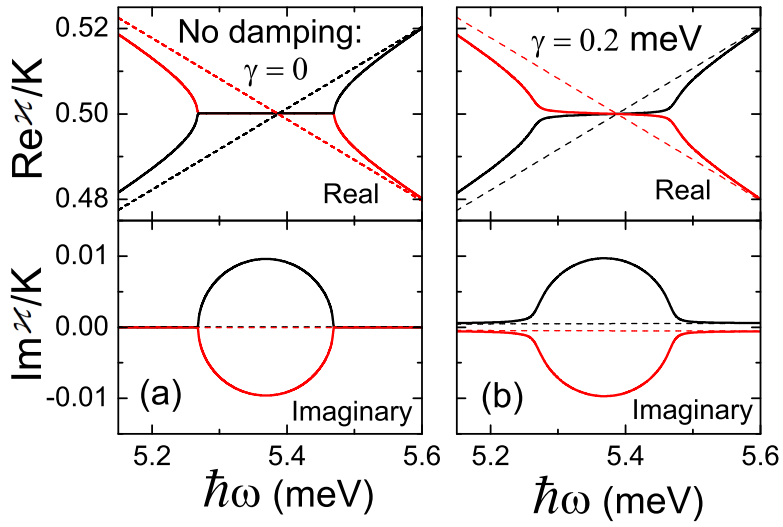

Figure 2.3: The solid lines show (a) both the real and imaginary parts of the acoustically driven complex polariton quasimomentum, at the acoustically induced band gap for no damping and in (b) for $\gamma = 0.2$ meV. The dashed lines show the same but without acoustic excitation. The black and red (gray) colors show the positive and negative acoustically shifted quasimomentum branches, respectively. The acoustic frequency is $\nu = 50$ MHz ($K = 0.1555\ \mu\text{m}^{-1}$).

third and fourth order coupling $M = 161$ therefore $-80 \leq j \leq 80$.

In Figure 2.2 the complex quasimomentum roots are shown, the real part in Figure 2.2(a) and the imaginary in Figure 2.2(b) both with and without the AW. The most noticeable alterations to the quasimomentum spectrum occur around $\omega_0 = 20.28$ meV, which are dependent on the coupling strength σ. However, other less noticeable alterations occur that are of remarkable importance to the THz properties of the crystal, despite their size relative to the Restrahlen band. The insets in Figure 2.2 shows the regions where TO-phonon transitions occur, the features they display are equivalent to the band gaps in the quasienergy spectrum. These features are examined more closely in Figure 2.3. The upper panel of Figure 2.3(a) shows the real part of the quasimomentum root for $\gamma = 0$. If this were calculated for $\nu_{ac} = 100$ MHz then it would reproduce the band gap shown in Figure 2.1(e), the difference between the two would be the horizontal line. Due to the factor of two difference between both calculations, the spectral position of the features examined in Figures 2.2 and 2.3 is half that of the band gap in Figure 2.1(e). The dashed lines in Figure 2.3 are the bare quasimomentum branches, the band gap occurs because of the strong AW induced coupling between them. The real part of the quasimomentum displays anti-crossing behaviour while the imaginary part shows the band gap. Should $\sigma = \gamma = 0$ no imaginary part would be present. In this band gap region the polariton

modes decay rapidly, this determined by the finite imaginary part of the polariton wavevector due to the coupling between AW and TO-phonon polariton component. The introduction of non-zero γ, which obeys $\gamma < \sigma$, makes little difference to the physical situation other than a non-zero imaginary part for all ω.

2.3 Band Gap Width

The modifications of the bare polariton dispersion due to the resonant acousto-optic effect falls into two categories. Firstly, the alteration of the main polariton band gap. Secondly, the creation of acoustically induced band gaps at specific points in the dispersion given by the Bragg condition, which are examined in this section. In the band gaps the propagation of the polaritons is forbidden, which results in the reflectivity increasing in the region of the gap. The width of these gaps is a figure of merit for the strength of the RAO effect, it is therefore worth consideration.

In this section a comparison is made between the numerically calculated band gap widths and the analytical calculations made by Dr. Egor Muljarov. The results of the analytical calculations given here are taken from the paper [35]. To begin, the matrix equations, Eq. (2.4), have the polarization dependence removed by making P_n the subject of Eq.(2.4a) and substituting it into Eq. (2.4b) gives

$$\alpha_n D_n E_n - \sigma\Big(\alpha_{n+1}E_{n+1} + \alpha_{n-1}E_{n-1}\Big) = 0, \tag{2.12}$$

where

$$D_n(k,\omega) = \frac{1}{2\omega_t}\left[\omega_t^2 - 2i\gamma(\omega + n\Omega) - (\omega + n\Omega)^2\frac{\omega_R^2}{\alpha_n(k,\omega)}\right], \tag{2.13a}$$

$$\alpha_n(k,\omega) = \frac{c^2}{\varepsilon_b}\left(\frac{k + nK}{\omega + n\Omega}\right)^2 - 1. \tag{2.13b}$$

The introduction of $\xi_n = E_n/E_{n+1}$ allows Eq. (2.12) to be solved recursively, by rewriting it as

$$\xi_n = \frac{\sigma\alpha_{n+1}}{\alpha_n D_n - \sigma\alpha_{n-1}\xi_{n-1}}. \tag{2.14}$$

To solve Eq. (2.12) up to the N^{th} order the truncation $E_{-N-1} = E_1 = 0$ is used. This approach to the solution of Eq. (2.12) is perturbative, with a small parameter σ/D_n,

and will break down when $\omega \to \omega_0$ or $\omega \to \sqrt{\omega_0^2 + \omega_R^2}$.

The truncation is equivalent to the pair of BC for Eq. (2.12)

$$\xi_{-N-1} = 1/\xi_0 = 0. \tag{2.15}$$

The starting point for the calculation of ξ_n would be the first BC. Iteration then continues until the relationship $\alpha_0 D_0 = \sigma\alpha_{-1}\xi_{-1}$ is reached via the final BC. This section shows the analytical results calculated using this pertabative method and compares it with the numerical calculations of the acoustically induced band gaps only. For consistency with the quasienergy dispersion discussed in section 2.2 $\gamma = 0$.

The bare polariton dispersion $\omega = \omega^0(k)$ can be calculated from the $N = 0$ case of Eqs. (2.14) and (2.15), which is

$$D_0(k, \omega) = 0. \tag{2.16}$$

The bare dispersion $\omega^0(k)$ consists of both UP and LP branches and can be seen in Figure 2.1, represented by the dashed line. In the zeroth order pertabative calculation no acoustic effects are apparent, the first and higher orders are required for that. The polariton wavevector coordinate of the gaps is given by the Bragg condition

$$k_N = NK/2\,, \quad N = 1,\, 2\,\ldots, \tag{2.17}$$

where the AW provides the periodicity. This condition leads to band gaps forming in the center and edges of the acoustically induced Brillouin zone. This is clear in Figure 2.1, which shows the numerically calculated AW modified dispersion for the extend zone scheme. The energetic position of the gaps, ω_N can be found from

$$\omega_N = \omega^0(k_N), \tag{2.18}$$

or by solving $D_0(k_N, \omega_N) = 0$. The gap widths are given by

$$\begin{aligned}
\Delta_1 &= \sigma S(\omega_1), \\
\Delta_2 &= \sigma^2 \frac{S(\omega_2)}{|D_{-1}(k_2, \omega_2)|}, \\
\Delta_3 &= \sigma^3 \frac{S(\omega_3)}{D_{-1}^2(k_3, \omega_3)}, \\
\Delta_4 &= \sigma^4 \frac{S(\omega_4)}{D_{-1}^2(k_4, \omega_4)|D_{-2}(k_4, \omega_4)|} \ldots
\end{aligned} \tag{2.19}$$

where

$$S(\omega) = \frac{2\omega\omega_0\omega_R^2}{(\omega^2 - \omega_0^2)^2 + \omega_0^2\omega_R^2}.$$

A full derivation of this result can be found in Appendix C of [35].

The AW induced band gaps δ_N are created in the polariton dispersion as a result of anti-crossing of different polariton dispersion branches. The origin of the anti-crossings lie in the translational invariance of the dispersion, which is such that states from opposite k sides of the bare polariton dispersion can become resonant. This can be arranged by a translational shift in inverse space of the states from the negative-k part of the dispersion by $(NK, N\Omega)$. Essentially, the N^{th} order band gaps open up in $\omega^0(k)$ due to the acoustically induced transition of N TO-phonons, from one side of the bare TO-phonon polariton dispersion to the other. The exact k-values which are coupled from each side of $\omega^0(k)$ are given by the Bragg condition detailed in Eq. (2.17). Accordingly, the width of the gap Δ_N is dependent on $\sigma_{3,4}^N$.

In the RAO effect the light and acoustic fields do not directly interact, the entire RAO effect is caused by the mediating TO-phonon as discussed in section 1.9. Therefore, the efficiency of the effect can increase by either increasing the acoustic intensity or by increasing the TO-phonon component of the polariton. In Figure 1.2 we show that near the TO-phonon frequency the energy of the polariton is distributed strongly in favor of the TO-phonon component. Thus, as detuning from the Restrahlen band reduces the strength of the RAO effect increases, in both LP and UP branches. In the LP branch considered in the perturbative results discussed above this is taken into account by the form factor $S(\omega)$, which increases with decreasing detuning.

The comparison of the numerical band gap width and the analytical calculation is shown in Figure 2.4 for a moderate acoustic intensity $I_{ac} = 2.4\text{kW/cm}^2$ ($\sigma = 0.4\text{meV}$).

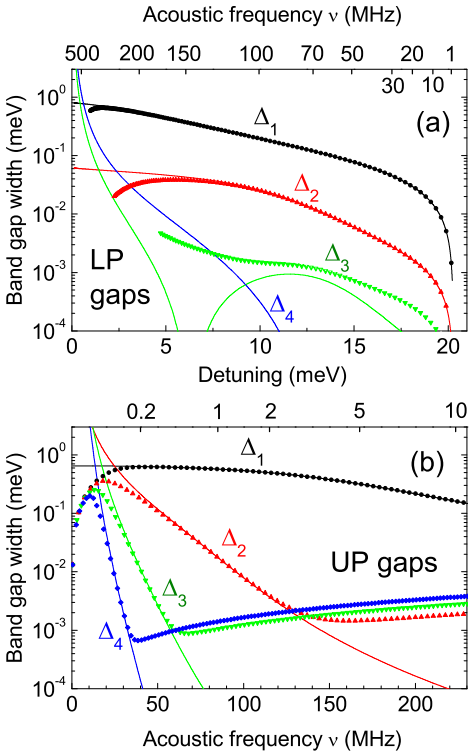

Figure 2.4: (a) Numerical (symbols) and analytical (lines) calculation of the width of the acoustically induced band gaps in the LP branch. The lower horizontal axis gives the abscissa as a detuning from the TO-phonon energy ($\omega_0 - \omega_{N=1}$) and the upper horizontal axis is simply the acoustic frequency ν. (b) Presents the same data as (a) but for the UP branch. In this case the detuning is given on the top horizontal axis and is taken from the LO-phonon frequency ($\omega_{N=1} - \sqrt{\omega_0^2 + \omega_R^2}$). The subscript $N = 1$ refers to the lowest acoustically induced energy gap. The coupling strength and damping for both panels is $\sigma_3 = 0.4$ meV and $\gamma = 0.2$ meV, respectively.

For Δ_1 and Δ_2 (lines) the agreement with the numerics (symbols) is excellent over a large range of the results. In the LP branch, shown in Figure 2.4 (a), at high acoustic frequency (low detuning) the agreement between the analytics and numerics fails. The assumption that the analytic model is based upon is that the detuning is large compared to the coupling strength, in the case of small detuning this clearly breaks down. This is also the case for low acoustic frequency in the UP branch. Due to the postion of the UP branch above the Restrahlen band, low acoustic frequency corresponds to small detuning. The higher order band gaps are not at all well reproduced. This is due to analytical calculation considering Ω negligible, which holds for the first two band gaps. However, at higher orders the band gap width has become μeV in size, this is comparable with Ω.

2.4 Third Order Anharmonicity: Copper Chloride

This section details the boundary condition problem that was solved to produce the reflectivity spectra including all important Bragg replicas. The numerical results are presented for a variety of parameters and shown to be modified due to the AW driving

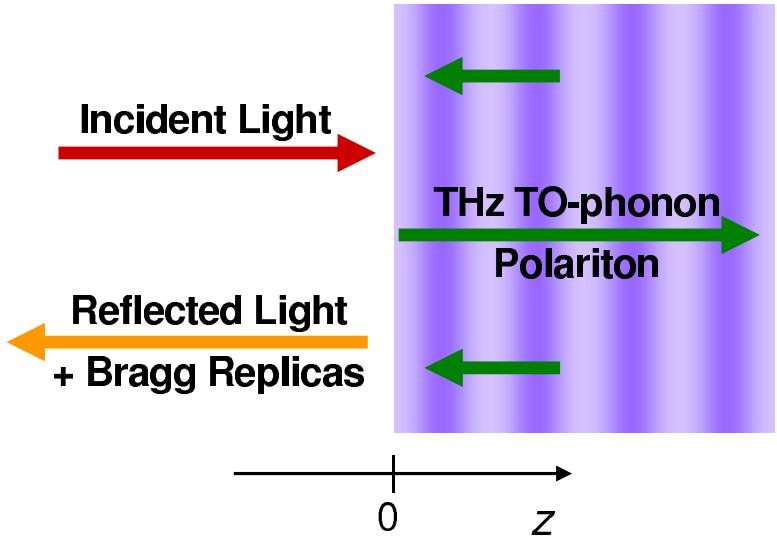

Figure 2.5: The schematic of the boundary considered for the TO-phonon polariton RAO effect. The vertical stripes symbolise a propagating bulk AW.

the TO-phonon polaritons. Some comparisons are also made to the approximate analytical results calculated using Dr. Muljarov's perturbative approach.

2.4.1 Numerical Bragg Reflectivity

This thesis considers a semi-infinite geometry for the TO-phonon polariton RAO effect problem with an ionic crystal-vacuum boundary at $z = 0$. In Figure 2.5 we see that the incident light, given by the red arrow results in reflected Bragg replicas as well as co- and counterpropagting transmitted Bragg replicas. In the vacuum the electric field takes the form

$$E(z < 0, t) = e^{iq_0 z} e^{-i\omega t} + \sum_n r_n e^{-iq_n z} e^{-i(\omega + n\Omega)t}, \tag{2.20}$$

where $q_n = (\omega + n\Omega)/c$ and r_n is amplitude of the outgoing Bragg replica, which has been normalised to the unity of the incident light wave. In the ionic crystal region

the electric field is joined by a polarization field, both have a similar form

$$E(z>0,t)=\sum_{n,j}A_jE_{nj}e^{i(\tilde{\kappa}_j+nK)z-i(\omega+n\Omega)t}, \tag{2.21a}$$

$$P(z>0,t)=\sum_{n,j}A_jP_{nj}e^{i(\tilde{\kappa}_j+nK)z-i(\omega+n\Omega)t}. \tag{2.21b}$$

Here, then normalised eigenvectors are E_{nj} and P_{nj} for the electric and polarization fields, respectively. The partial wave amplitude is given A_j.

Both the partial wave amplitudes A_j and the Bragg replica amplitudes r_n are found by considering the boundary using Maxwell's boundary conditions (BCs). These require that both the electric field and the magnetic field $H(z,t)$ are continuous across the boundary found at $z=0$. Using the one dimensional form of Eq. (1.29c) from section 1.8, $H(z,t)$ can be calculated from $E(z,t)$, which gives the set of equations

$$e^{-i\omega t}+\sum_n r_ne^{-i(\omega+n\Omega)t}=\sum_{nj}A_jE_{nj}e^{-i(\omega+n\Omega)t},$$

$$e^{-i\omega t}-\sum_n r_ne^{-i(\omega+n\Omega)t}=\sum_{nj}A_jE_{nj}\frac{\tilde{\kappa}_j+nK}{q_n}e^{-i(\omega+n\Omega)t}.$$

These equations hold for any time t. By equating coefficients they can be written in a more convenient form, that can be easily solved for r_n and A_j.

$$\delta_{n,0}+r_n=\sum_j A_jE_{nj}, \tag{2.22a}$$

$$\delta_{n,0}-r_n=\sum_j A_jE_{nj}\frac{\kappa_j+nk}{q_n}. \tag{2.22b}$$

These equations are numerically solved by a truncation $-n_B\leq n\leq n_B$, where the total number of Bragg replicas is given by $N_B=2n_B+1$. The truncation used for the BC problem is different from that used for the calculation of the central polariton quasimomentum Bragg replica $\varkappa(\omega)$. The number of Bragg replicas used for the determination of r_n and A_j is a lot smaller, therefore $N_B<<M$. An example of this can be found when trying to calculate the reflectivity for $\sigma_3=2$ meV and $\nu=100$ MHz, to determine $\varkappa(\omega)$ to an accuracy of 10^{-7} $M=81$ but to calculate r_n and A_j the matrix dimensions is only $N_B=21$.

The Bragg replicas cannot be spatially selected because of the collinear propagation

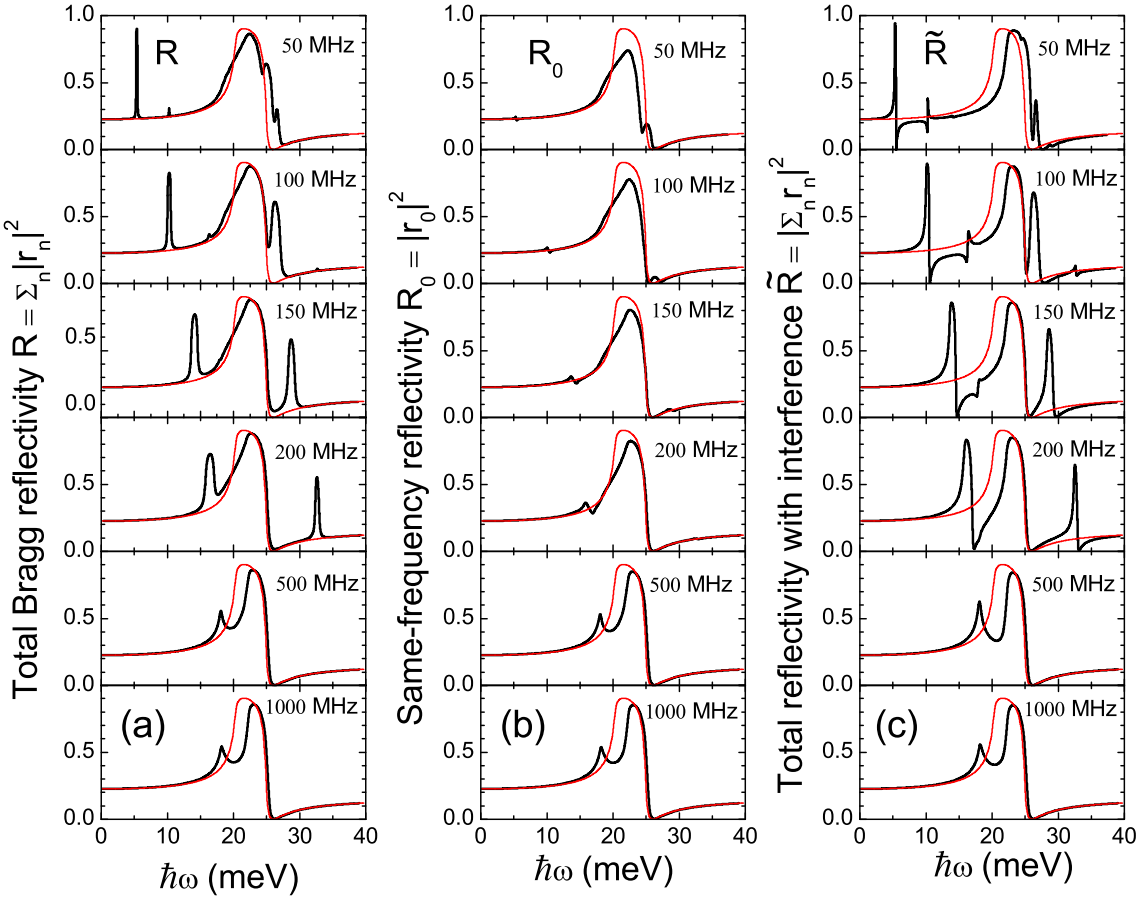

Figure 2.6: (a) Incoherent total Bragg reflectivity, (b) central Bragg replica reflectivity and (c) coherent total Bragg reflectivity for various acoustic frequency and $\sigma = 1$ meV, while $\gamma = 0.2$ meV. (a) does not show any interferences terms but (c) does. The thin red lines show the reflectivity without the presences of an AW.

of the AW and the TO-phonon polaritons. However, thanks to the propagating nature of the AW each Bragg replica has its own unique temporal evolution. This is clearly demonstrated by considering Eqs. (2.21), where the time dependence of the n^{th} Bragg replica has the frequency $\omega + n\Omega$. Clearly, the effect of this propagating AW on the Bragg replicas is to either upconvert or downconvert the undressed polariton frequency, depending on the sign of n. If a frequency selective technique is used the intensity of the n^{th} Bragg replica in the reflected light field $R_n = |r_n|^2$ can be measured.

The effect of each Bragg replica having a unique temporal evolution will have an important impact on the technique used to measure the reflected light field. If the temporal resolution of the spectrometer τ is not sufficiently fine enough to resolve the

interference fringes of the Bragg replicas then the reflectivity will be fully incoherent

$$R(\omega) = \sum_{n=-n_B}^{n_B} |r_n|^2. \tag{2.23}$$

The condition for this case of reflectivity measurement is $\Omega\tau >> 1$, for this to hold τ would have to be of the order of nanoseconds. The other example of reflectivity measurements in the case of the TO-phonon RAO effect is the fully coherent case. Here the spectrometer would have sufficiently fine τ to resolve the interference fringes of the Bragg replicas. In this case $\Omega\tau << 1$ putting τ in the sub-nanosecond to picosecond range. The fully coherent total Bragg reflectivity can be calculated by

$$\widetilde{R}(\omega) = \left| \sum_{n=-n_B}^{n_B} r_n \right|^2. \tag{2.24}$$

The two cases of measurement of the total Bragg reflectivity discussed above are shown in Figure 2.6 for various AW frequency. Figure 2.6 (a) shows the incoherent reflectivity and Figure 2.6 (c) shows the coherent equivalent. It should be noted that Figure 2.6 (c) would be equivalent to a spectrometer measuring the reflectivity with sufficient spectral resolution to observe variation of the reflectivity with time due to Ω. Thus, in general Figure 2.6 (c) is time depdent and is shown here at $t = 0$. In Figure 2.6 (b) the zeroth Bragg replica R_0 is shown. It is the only Bragg replica to survive the removal of the AW, which leads to the red curve shown in all panels of Figure 2.6. This is calculated by setting $\sigma_3 = 0$. The black curves are all calculated for a coupling strength of $\sigma_3 = 1$ meV. It can be clearly seen in Figure 2.6 that the increasing acoustic frequency up to 1 GHz has the effect of blue shifting the peak associated with the $N = 1$ TO-phonon transition. In the LP branch, when using lower AW frequencies, the reflectivity peaks are due to individual acoustic band gaps formed from specific acoustically induced TO-phonon transitions. These give rise to the large peaks for AW frequencies up to $\sim$ 300 MHz. The thickness of these peaks is dependent on the band gap width or the TO-phonon damping, whichever has the greater magnitude. As the peak approaches ω_0 it becomes wider, until the peak becomes a cusp-like feature seen in all panels of Figure 2.6 at 1 GHz. In the UP branch the peaks become hard to resolve at AW frequencies below 100 MHz as the UP states are pushed in to the Restrahlen band. Between this frequency and 300 MHz the AW frequency evolution of the peaks is similar to the LP branch counterparts. There is a noticeably stronger effect in the coherent reflectivity $\widetilde{R}(\omega)$, where the spectral

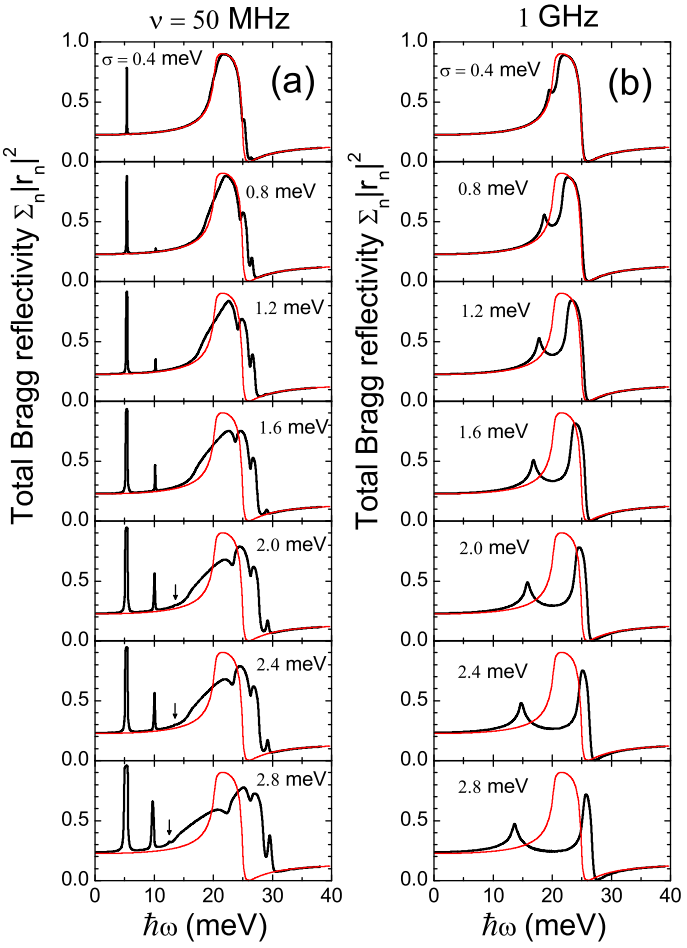

Figure 2.7: The total Bragg reflectivity calculated for (a) $\nu = 50$ MHz and (b) $\nu = 1$ GHz and for various coupling strengths. The spike in (a) due to the third-order band gap is highlighted by the arrow. The red (gray) line shows the bare TO-phonon polariton reflectivity spectrum. The damping is set to $\gamma = 0.2$ meV.

modifications are considerably enhanced due to dispersive features caused by a strong interference effect.

Due to the similarity of the three reflectivity spectra in Figure 2.6 at 1 GHz, it is clear that the evolution of the peak into a cusp-like feature takes place only in the zeroth Bragg replica, no other orders contribute. This is due to an AW frequency that is equivalent to a submicron wavelength, while the polariton wavelength is in the micron range. Thus, the light field has wavelength too large to resolve the AW. This means that the polaritons pass through a homogeneous material in which the AW has modified the ω-dependent dielectric constant, that is the AW no longer provides a dynamic superlattice and the Bragg condition no longer holds. This leads to a direct modification of the zeroth Bragg replica, all others vanish. The cusp-like feature can be understood as the result of the acoustically induced band gaps accumulating around the TO-phonon frequency, of which, in principle, there are an infinite number, though increasingly less significant. Lower detuning from the Restrahlen band does not produce a cusp like feature in the UP branch due to the shape of its dispersion.

The approximately parabolic shape of the dispersion in this region of the LP branch does not allow for the accumulation of band gaps.

In Figure 2.7 the effect of increasing the coupling strength is shown for both high and low frequency limits. In the low frequency limit shown in Figure 2.7 (a), the increased coupling strength leads, not only to an increase in the strength of the $N = 1$ TO-phonon peak but also to new features. These new features correspond to the second and third band gaps widening as a result of increased coupling strength, that is an increase in the strength of the $N = 2$ and $N = 3$ acoustically induced TO-phonon transitions. The new features can be seen in both the LP and UP branches. Figure 2.7 (b) shows the effect the increased coupling strength has on the total Bragg reflectivity in the high frequency limit. In this case there no new features appear, however the strength of cusp increases with coupling strength, as does its splitting from the Restrahlen band. The effect of this is to reduce the reflectivity of the Restrahlen band.

Figure 2.8 shows the contribution each Bragg replicas makes to the reflected electric field and how this is effected by the acoustic frequency. In the top panel of this figure the zeroth Bragg replica dispersion $\varkappa(\omega)$ is shown. In theses panels the Bragg condition is highlight by horizontal gray lines, which are separate by a wavevector of $K/2$, and arrows of length K. The y-axis is measured in units of the initial wavevector $K_0 = 0.1555$ μm. In the bottom panels the red lines show the total Bragg reflectivity and the dashed lines highlight the reflectivity peaks that appear at spectral position of the first-order acoustic bands gaps. These peaks are due to a set of one TO-phonon transitions between the positive and negative sides of the dispersion $\varkappa(\omega)$.

The term "one TO-phonon transition" refers to the scattering channel that the transitions use. The fact that the peak due to the $N = 1$ band gap in the total Bragg reflectivity has contributions from at least up to the $n = -4$ Bragg replica, indicates that this peak is dependent, albeit more weakly, on more than simply the transition of one TO-phonon. That is, it has contributions from N concurrent TO-phonon transitions that all occur using the one TO-phonon transition scattering channel. This is also true of the other peaks in the reflectivity spectrum.

The reflectivity of the n^{th} Bragg replica also has more contributions than just those due to the $N = |n|$ TO-phonon transitions. In the LP branch of Figure 2.8 (a) it is clear that some Bragg replicas contains peaks due to N-phonon transitions where $N \neq |n|$. This is because all higher order Bragg replicas accumulate the lower n-phonon

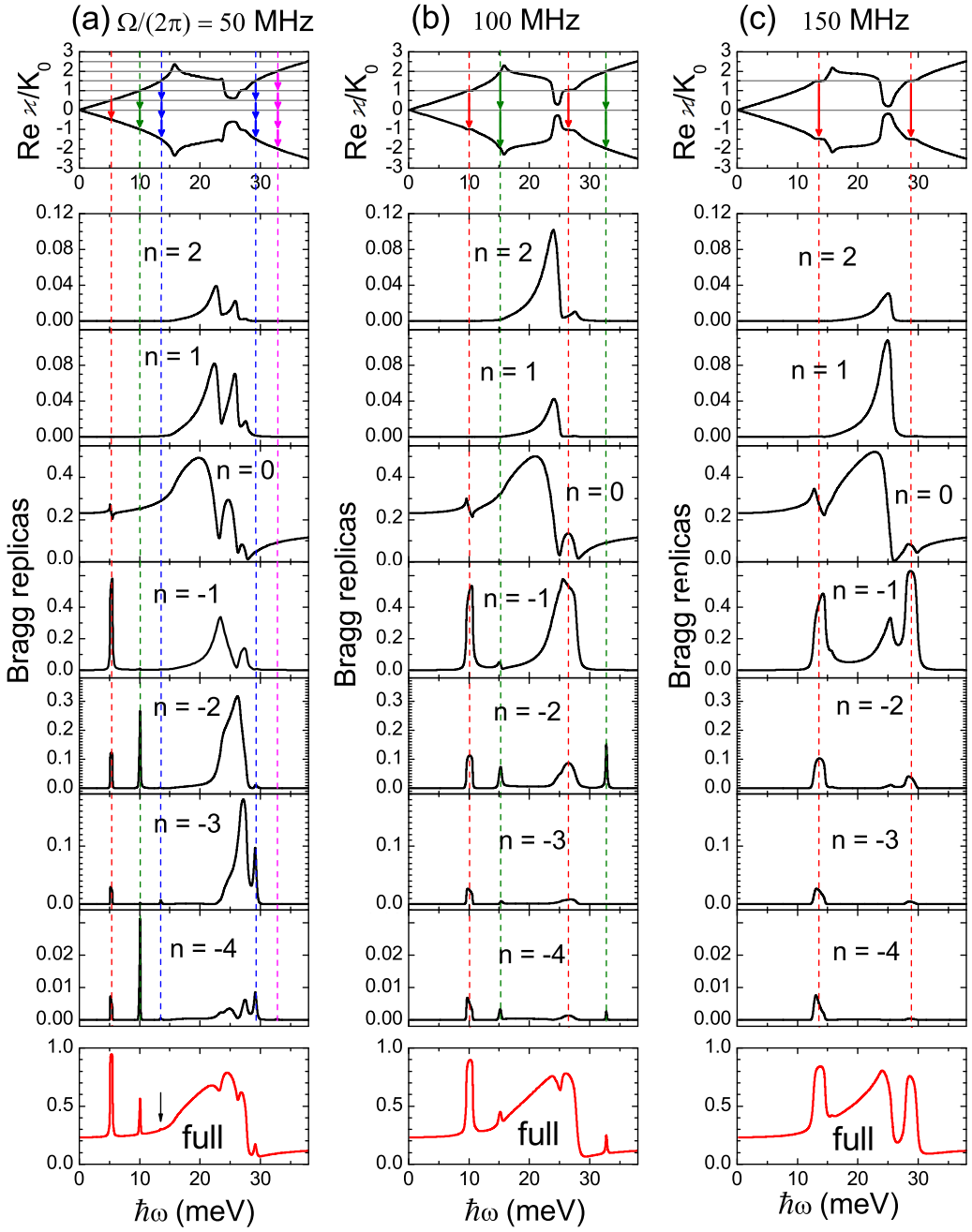

Figure 2.8: The top panel shows the acoustically modified quasimomentum spectrum over both LP and UP branches. The central panels show the contributions of the Bragg replicas in the range $-4 < n < 2$. Finally the bottom panel shows the total Bragg reflectivity. The calculations used the parameters $\sigma = 2$ meV and (a) $\nu = 50$ MHz, (b) $\nu = 100$ MHz and (c) $\nu = 150$ MHz. The vertical dashed lines indicated the positions of the band gaps, the colored arrows in the upper panels show N-phonon transitions. The associated acoustic wavevectors are (a) $K = K_0$, (b) $K = 2K_0$ and (c) $K = 3K_0$ for $K_0 = 0.1555$ μm.

transitions. In some cases the higher order Bragg replicas contain contributions from lower order transition that are stronger than $N = |n|$ transition. For example, the $n = -4$ Bragg replica in Figure 2.8 (a).

The effect of increasing the AW frequency is seen more explicitly in Figure 2.8. The position of the TO-phonon transitions is given by the Bragg condition. Upon increase of the Ω, which consequently increases K, this Bragg condition can only be fulfilled at higher frequency positions in the dispersion. This must lead to a blueshift of the band gaps. This blueshift also affects the width of the band gaps due to difference in the TO-phonon content of the TO-phonon polariton at different points in the dispersion. Higher TO-phonon contribution to the polariton leads to stronger coupling and a wider band gap, these conditions can be found around the Restrahlen band. In Figure 2.8 (a) the peaks in the LP branch are weaker than those in Figure 2.8 (b) and (c) because of their spectral position. The opposite is true in the UP branch, where a blueshift removes the band gap from the vicinity of the Restrahlen band leading to weaker peaks in the reflectivity.

The fact that the negative n Bragg replicas contribution is strongly dominant over the positive n Bragg replicas is simply because the reflectivity is being considered. The incident light excites positively propagating polariton modes, that is modes with $\varkappa > 0$. The AW can scatter these modes into the $\varkappa < 0$ part of the polariton dispersion. Due to the accompanying emission of acoustic phonons the scattering event is also a downconversion in frequency of the TO-phonon polariton. The downconvert polariton waves remain down converted in both crystal and vacuum and correspond to the negative-n components of the electric field found in Eqs (2.20) and (2.21). This is the cause of the dominant negative n TO-phonon transitions in the total Bragg reflectivity.

Finally, the peaks found in each Bragg replica R_n are not actually due to individual N TO-phonon transitions, they are all dressed by higher order processes. Any N^{th}-order band gap is caused mainly by N TO-phonon transitions, but also has components from multiple simultaneous emission of $N + s$ phonons and the absorption of s phonons, in principle for any integer s. The size of these higher order effects is depend on the magnitude of σ and in the calculations presented in this chapter $|s| \leq 20$ even for coupling up to $\sigma = 3$ meV.

2.4.2 Analytical Comparison

For a small σ (low acoustic intensity) the reflectivity of each Bragg replica can be calculated using the approximate perturbation approach discussed in section 2.3. This approach uses the N^{th} perturbative order to describe the RAO effect in which only N TO-phonons participate, there are no higher order effects. The approach would take account of Δ_N gaps due to N TO-phonon transitions. In what follows, the N^{th} Bragg replica is calculated in its lowest order, including both the upconverted $r_{n=+N}$ and downconverted $r_{n=-N}$ cases. It is also explicitly shown that only the downconverted $r_{n=-N}$ Bragg replica is resonantly enhanced.

The results of the perturbation theory presented here are derived in Appendix D of reference [35]. For the N^{th} Bragg replica the recursive form of the perturbative result is

$$r_{\pm N} = -\sum_{s=1}^{N} A_{\pm(N-s)} E_{\pm s} \frac{\beta_{\pm s} - \beta_0}{1+\beta_0}, \tag{2.25}$$

$$A_{\pm N} = -\sum_{s=1}^{N} A_{\pm(N-s)} E_{\pm s} \frac{1+\beta_{\pm s}}{1+\beta_0}, \tag{2.26}$$

$$E_{\pm N} = \sigma^N \frac{\alpha_0}{\alpha_{\pm N}} \prod_{s=1}^{N} \frac{1}{D_{\pm s}}, \tag{2.27}$$

where $D_n(\omega, k)$ is defined in Eq. (2.13a),

$$\alpha_n = \left(\frac{k+nK}{p}\right)^2 - 1\,, \quad \beta_n = \frac{k+nK}{q}, \tag{2.28}$$

$q = \omega/c$, $p = \sqrt{\varepsilon_b} q$ and for simplicity the Ω dependence has been dropped. The recursive initial point is at $N = 0$ and the starting values are given by

$$r_0 = \frac{1-\beta_0}{1+\beta_0}\,, \quad A_0 = \frac{2}{1+\beta_0}\,, \quad E_0 = 1. \tag{2.29}$$

Initially the zeroth order quasimomentum k is used in the the above equations, the zeroth order being the bare polariton dispersion $k = k^0(\omega)$. This can be calculated from Eq.(2.16) and is the inverse of the bare quasienergy dispersion $\omega = \omega^0(k)$. By

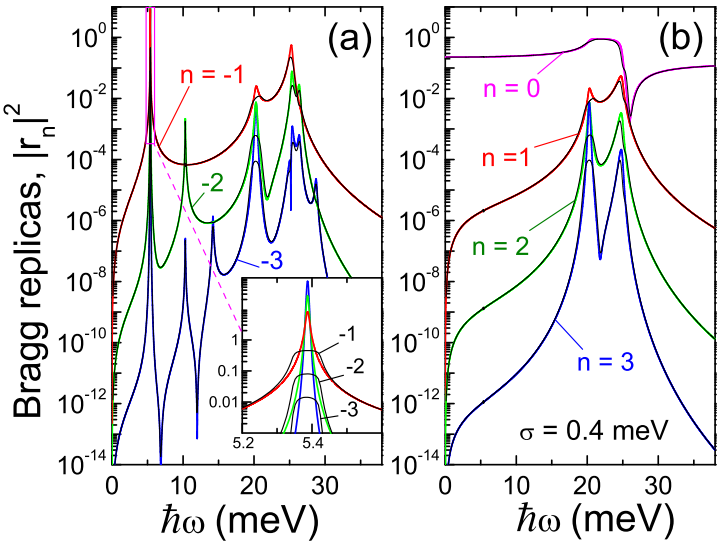

Figure 2.9: Black lines show the reflectivity of individual Bragg replicas calculated numerically, the colored lines show their analytical counter parts. In (a) $n = -1, -2, -3$ and (b) has $n = 0, 1, 2, 3$. Both analytical and numerical calculations used the parameters: coupling strength $\sigma_3 = 0.4$ meV, acoustic frequency $\nu = 50$ MHz and damping $\gamma = 0.2$ meV. The inset highlights the reflectivity peak in the region of first, lowest energy, band gap.

using Eq.(2.16) the functions $D_n(\omega, k)$ written in Eq. (2.13a) can be simplified to

$$\alpha_n D_n = \frac{\omega_R^2}{2\omega_t} \frac{(k + nK)^2 - k^2}{k^2 - p^2} \tag{2.30}$$

when Ω is neglected.

Consider Eq. (2.27), in the denominator stands D_n and from Eq.(2.25) it is clear that r_n has a maxima when $\alpha_n D_n$ is minimized. This occurs when $(k + nK)^2 \approx k^2$, which leads to a Lorentzian peak at the Bragg condition

$$\mathrm{Re}(k) = -\frac{nK}{2}, \tag{2.31}$$

the widths of which are proportional to $\mathrm{Im}(k)$. Currently, $\mathrm{Im}(k)$ is fully determined by the TO-phonon damping γ. It is instructive to note that the incident light excites TO-phonon polaritons with wavevectors $\mathrm{Re}(k) > 0$, therefore, by Eq. (2.31), only $n < 0$ fulfills the Bragg condition. Thus, only the downconverted Bragg replicas are observed in the reflectivity.

The three lowest order Bragg replica amplitudes are given by

$$r_{-1} = \sigma \frac{K}{q} \frac{2}{(1+\beta_0)^2} \frac{\alpha_0}{\alpha_{-1} D_{-1}}, \tag{2.32a}$$

$$r_{-2} = \sigma^2 \frac{K}{q} \frac{2}{(1+\beta_0)^2} \left[\frac{2\alpha_0}{\alpha_{-2} D_{-2} D_{-1}} - \frac{1+\beta_{-1}}{1+\beta_0} \frac{\alpha_0^2}{\alpha_{-1}^2 D_{-1}^2} \right], \tag{2.32b}$$

$$r_{-3} = \sigma^3 \frac{K}{q} \frac{2}{(1+\beta_0)^2} \left[\frac{3\alpha_0}{\alpha_{-3} D_{-3} D_{-2} D_{-1}} - \frac{3+2\beta_{-1}+\beta_{-2}}{1+\beta_0} \frac{\alpha_0^2}{\alpha_{-2}\alpha_{-1} D_{-2} D_{-1}} + \left(\frac{1+\beta_{-1}}{1+\beta_0} \right)^2 \frac{\alpha_0^3}{\alpha_{-1}^3 D_{-1}^3} \right]. \tag{2.32c}$$

These three results are the approximate analytical comparison to the numerical results previously presented, this can be seen more clearly in Figure 2.9 where the calculations were made for a moderate coupling strength of $\sigma_3 = 0.4$ meV. There is strong agreement between both results everywhere but the peaks, where only the spectral position is correctly reproduced by the analytics. This is most clearly seen in the inset to Figure 2.9 (a), which shows that not only is the Lorentzian shape inaccurate but that it is unphysical, with $|r_n|^2 > 1$. However, this artifact can be removed by taking into account the acoustically modified spectrum, which is discussed below. In Figure 2.9 (b) both numerical and analytical calculations are shown for $n > 0$, this panel clearly demonstrates a lack of acoustically induced reflectivity peaks.

The r_{-1} downconverted Bragg replica peaks at the frequency ω_1, which is the frequency of the lowest acoustically induced band gap, this was shown in Eq. (2.18). As discussed previously, the peak corresponds to a one TO-phonon transition from the negative-k side of the polariton dispersion to the positive, this was shown in Figure 2.8. It is also important to note that while the following discussion focuses on the LP branch, similar peaks can be found in the UP branch.

The second Bragg replica has more complex structure that can be used as the starting point of a more general understanding of the Bragg reflection. In Figure 2.9 the $n = -2$ replica has peaks at both $\omega = \omega_1$ and ω_2. This can be explained by considering Eq. (2.32b), the first term in the square brackets describes a composite two phonon process. The virtual intermediate state in this process emits only one acoustic phonon. As a result when Eq. (2.32b) is examined in Figure 2.10 the origin of the two peaks in r_{-2} becomes apparent. The red, dashed line of Figure 2.10 shows the first term in the square brackets. It clearly shows two peaks in the LP part of the spectrum, the higher

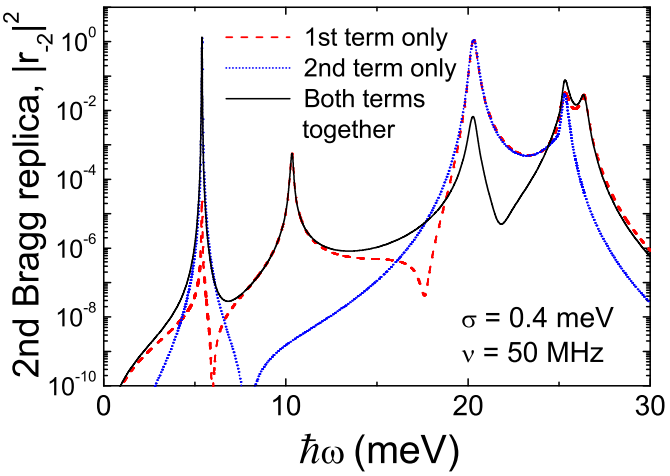

Figure 2.10: The analytic calculation of the Bragg reflectivity of the second Bragg replica from Eq. (2.32b). The first term only is given by the red dashed line, the second only by the blue dotted line and the full calculation by the black line. The parameters used in the calculation are the same as Figure 2.9.

energy one is the final state which dominates the lower energy intermediate one. By considering the second term, which is the blue dotted line in Figure 2.10, it has only one peak which shows the one phonon transition in second order. The fact that there is only one peak from the second term, is because the one phonon transition is the only component of r_{-1}. The resultant effect of these processes is that the $\omega \approx \omega_1$ peak is dominant overall, as can be seen by the black line in Figure 2.10. This reasoning can be generalised to higher order peaks, for example, in the Eq. (2.32c) the first term is due to a three-phonon process with an intermediate states in which one and two phonons are emitted. The last term is the third-order one phonon transition and the second term is a mixture of the one and two phonon transitions. Thus, three peaks are present in r_{-3}, at $\omega = \omega_1$, ω_2 and ω_3, all of which are due to various three phonon processes.

As mentioned previously, the initial analytical calculation of r_n used the bare polariton dispersion, which lead to unphysical results for even a relatively modest coupling strength. The solution to these problems is to replace $k = k^0(\omega)$ in Eqs. (2.28) and (2.30) with the numerically calculated, acoustically modified quasimomentum, $k = \varkappa(\omega)$. This results in a modification to the acoustic Bragg condition of Eq. (2.31), which determines the resonant energies ω_n of the RAO effect, given below

$$\mathrm{Re}\big[\varkappa(\omega_{|n|})\big] = -\frac{nK}{2}. \tag{2.33}$$

This approach to the analytical calculation allows the a larger number of Bragg replicas to be taken into account. While this is not strictly consistent with a lowest order calculation of r_n it does produced the desired improvements. Practically, this method of calculation works provided the resonances are suitably narrow. Figure 2.11(a)

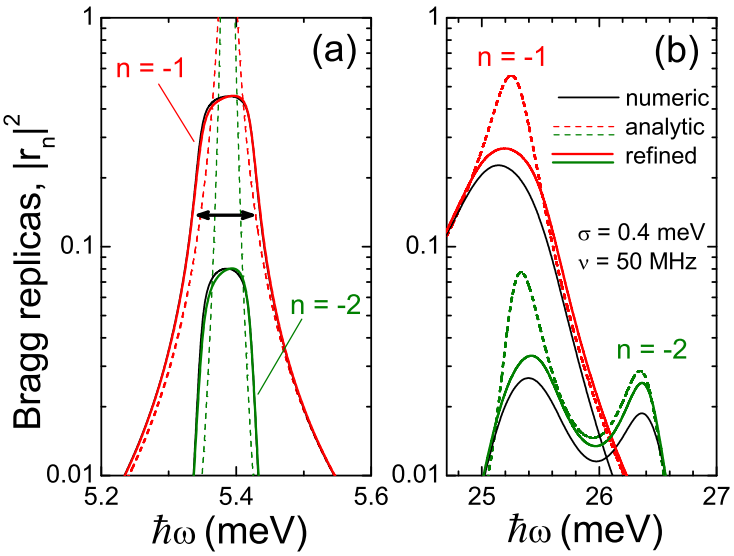

Figure 2.11: The analytic calculation of the Bragg reflectivity for the $n = -1$ and $n = -2$ Bragg replicas are shown by the coloured lines, the numerical calculation is shown by the black lines. The solid coloured lines were calculated by taking into account the effect of the AW on the dispersion, the dashed lines were calculated from the bare TO-phonon polariton dispersion. The arrow indicates acoustically induced gap width of the lowest energy band gap, as calculated by the first equation of Eqs. (2.19). In (a) the lower polariton branch is shown and in (b) the upper polariton branch is shown.

shows the improved calculations with the solid coloured lines and compares them with full numerical calculations in black and the original analytics given by the dashed coloured lines. In both analytic cases the red lines are for the $n = -1$ Bragg replica and the green lines for the $n = -2$ Bragg replica. The solid coloured lines reproduce the height and width of the full numerical calculations well, which is in contrast to the original analytics. As mentioned previously, the linewidth in these calculations is due solely to TO-phonon damping, in the improved calculations the use of $\varkappa(\omega)$ allows band gap width to determine the width of the peaks in r_n. This is because the band gap width is properly incorporated into $\varkappa(\omega)$, which is not the case with $k^0(\omega)$. There is a slight discrepancy between the improved analytics and the numerical calculation, which is due to the higher order corrections inevitably included in the numerical calculation but absent from the analytics. The fact that these corrections are large enough to make a noticeable, albeit small, discrepancy for a coupling strength as modest as $\sigma = 0.4$ meV is rather surprising. These higher order correction are more important for the UP branch at the low acoustic frequency of $\nu_{ac} = 50$ MHz due to the increased coupling strength around the Restrahlen band. This can be seen from the reduced impact the improvements have had on the analytics and the far

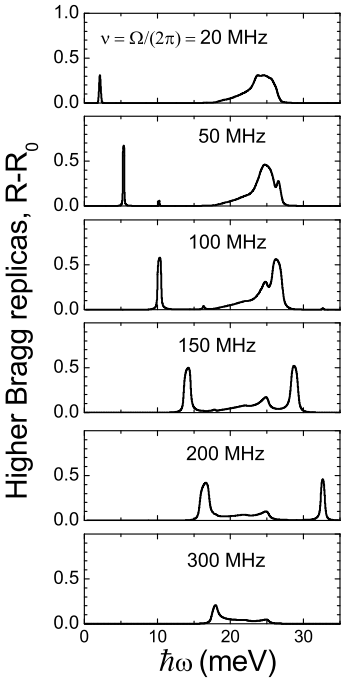

Figure 2.12: The total Bragg reflectivity less the central Bragg reflectivity for $\sigma_3 = 1$ meV and various acoustic frequencies.

larger discrepancy than in the LP branch.

Finally, a comment on the origin of the cusp-like dispersive features in the $n = 0$ Bragg replica. To begin second order corrections have to be included in the analytic equation

$$r_0 = \frac{1-\beta_0}{1+\beta} + \sigma \left(\frac{K}{q}\right)^2 \frac{4}{(1+\beta_0)^3} \frac{\alpha_0^2}{\alpha_1 D_1 \alpha_{-1} D_{-1}}. \tag{2.34}$$

It is clear from D_{-1} in the denominator of the second term above, that resonant features will be produced in r_0. In higher order Bragg replicas the resonant term is added to the Lorentzian line shape. However, in this case the term has only the bare TO-phonon polariton reflectivity to which the first term can be added. As a result of this mixing of the first and second terms in Eq. (2.34) a dispersive feature is seen in the $n = 0$ Bragg replica instead of the Lorentzian peak. This can been seen in the N shaped feature found in the zeroth Bragg replica, a numerical calculation of which is found in Figure 2.6 (b) for various frequencies.

2.4.3 Low and High Acoustic Frequency Behaviour

Previously, in this section, a discussion of the effect of various acoustic frequencies Ω on the AW driven polaritons has been presented and it was shown that Ω can be used

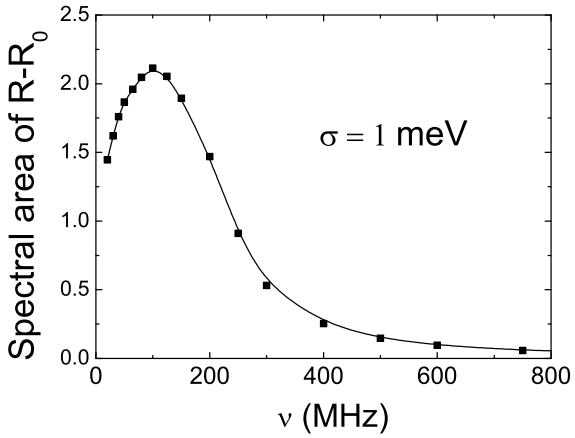

Figure 2.13: The spectral area of the Bragg reflectivity of the $n \neq 0$ Bragg replicas given by Eq. (2.35) and calculated for $\sigma = 1$ meV.

as a parameter to control the terahertz properties of semiconductors. Specifically, Figure 2.6 showed that the position and widths of the acoustically induced peaks in the reflectivity can be tuned by Ω. This figure also shows the effect of very large Ω on the reflectivity. This was characterised by two features, the formation of the cusp near the Restrahlen band, which was due to the accumulation of acoustically induced band gaps, and the massive reduction in strength of the higher order Bragg replicas. The later was caused by the AW modulation wavelength being reduced to the point where the light field was no longer able to be diffracted by it, which leads to the acoustic changes being limited to the zeroth Bragg replica. Figure 2.12 shows this more clearly, with each consecutive panel the AW frequency is increased and the total higher Bragg replica contribution decreases. Figure 2.13 highlights this for a greater number of frequencies, showing the spectral area approaching zero as $\Omega \to \infty$. The spectral area is calculated using

$$\int_{-\infty}^{\infty} \sum_{n \neq 0} |r_n(\omega)|^2 \, d\omega \,. \tag{2.35}$$

In the opposite limit the spectral area of the higher Bragg also replicas reduces as $\Omega \to 0$. In this case the AW becomes less effective at modulating the medium as the wavelength becomes long. Essential, this is the limit of no AW modulation so it is expected that for $\Omega < 10$ MHz the spectral area will fall to zero. However, the current numerical calculation does not produce results easily at $\nu < 20$ MHz and so it is difficult to produce results to support this claim.

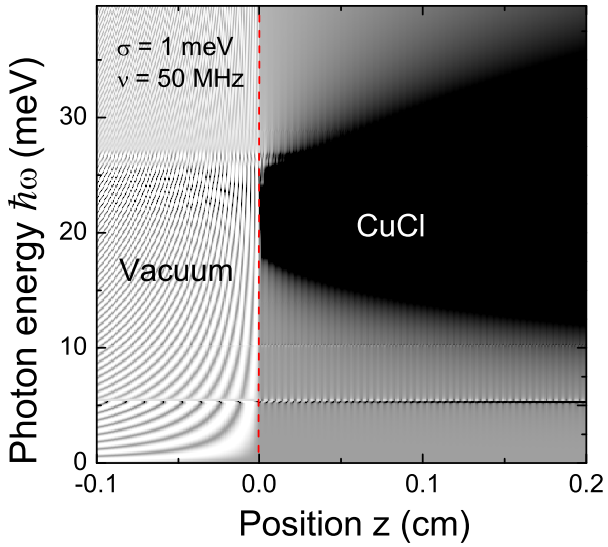

Figure 2.14: The electric field $|E(z,\omega)|^2$ in both vacuum and CuCl. The boundary is given by the dashed red line. The parameters used were $\sigma_3 = 1$ meV and $\nu = 50$ MHz. The colour scale is logarithmic and black corresponds to $|E|^2 \to 0$.

Finally, the region of the UP branch just above the Restrahlen band shows a peak in the reflectivity in Figure 2.12 for $\Omega = 20$ MHz. This is due to the accumulation of transitions at the upper edge of the Restrahlen band. Unlike the effect at the lower edge of the Restrahlen band the effect on the reflectivity remains associated with the n-Bragg replicas for $|n| \neq 0$.

2.4.4 Electric Field and Interaction Length

In Figure 2.14, the wavelength of the incident light is comparable to the AW modulation, which results in significant changes to the electric field. These changes are due to strong Bragg scattering of the TO-phonon polariton modes by the AW induced modulation of the CuCl crystal. The electric field shown in Figure 2.14 was calculated for $\nu = 50$ MHz, which means it corresponds to the reflectivity spectrum of the top panel of Figure 2.6 (a). The dashed red line shows the position of the interface between the vacuum and semi-infinite CuCl crystal. On the left, the modulations of the vacuum electric field are dependent solely on the light wavelength $\lambda = \lambda_{vac}/\sqrt{\varepsilon_b}$, and are caused by the interference of incident and reflected waves. On the right, in the semiconductor region, the medium is modulated by the AW which is constant for all ω, and given by the AW wavelength $2\pi/K$. An acoustically induced half-λ modulation occurs at $\hbar\omega \approx 5$ meV. The resulting destructive interference between

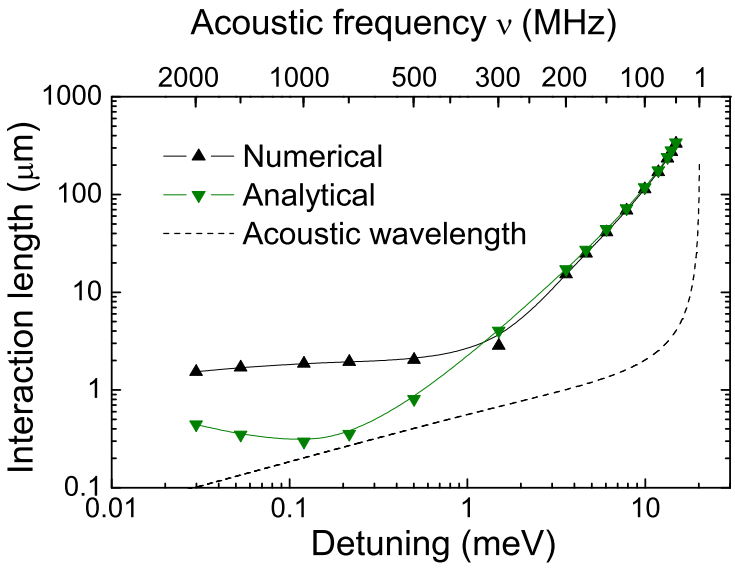

Figure 2.15: The interaction length for the lowest energy band gap in the LP branch. Obtained from the numerically calculated electric field profile (black line and triangle) shown in Figure 2.14 and analytically calculated from Eq. (2.36). Calculated with $\gamma = 0.2$ meV and $\sigma = 1$ meV. The detuning is given by $\omega_0 - \omega_1$ and the dashed line is the acoustic wavelength.

the co- and counterpropagting TO-phonon polaritons causes an abrupt attenuation of the electric field, seen as a thin black line in Figure 2.14.

The interaction length of the RAO effect l_{int} can be given an upper bound by the decay length of the electric field. This will characterise the length, in real space, over which the TO-phonon mediated coupling between the light and acoustic field takes place. An analytical comparison to the numerical results is given here

$$l_{\text{int}} = \frac{Kc^2}{\sigma\varepsilon_b\omega_t} \frac{(\omega_0^2 - \omega^2)^2 + 4\gamma^2\omega^2}{4\omega^2\omega_R^2} \tag{2.36}$$

The derivation of the interaction length is provide in Appendix E of [35]. The interaction length is shown in Figure 2.15 with the numerical calculation in black and its analytical comparison in green. In both case the calculation was performed at the first resonant frequency $\omega = \omega_1$ in the LP branch. The agreement between both results is excellent for the whole range of AW frequencies. At smaller detuning $\delta\omega = \omega_0 - \omega_1$ the numerical interaction length decreases monotonically and is limited by the damping of the TO-phonon. The dashed line showing the acoustic wavelength clearly indicates that the interaction length is never more than ten to a hundred time greater, this is a considerable improvement over conventional acousto-optics.

2.5 Quartic Anharmonicity: Thallium Chloride

In the previous section CuCl was the material considered, where the cubic anharmonic coupling between the TO-phonon component of the TO-phonon polariton and the AW is dominant. This led to Eq. (2.6), which was derived via the substitution of Eqs. (2.3) into the macroscopic equations Eqs. (2.1) and subsequently setting $\sigma_4 = 0$. From this tridiagonal matrix equation the numerical method was developed. In this section TlCl is the material under consideration, where the fourth order term is dominant in the Taylor expansion of the interatomic potential. This means that, while the derivation of the numerical method does not change, it is required that $\sigma_3 = 0$ instead of σ_4.

The process by which the matrix problem is derived in the third order case of CuCl, when applied to the fourth case gives

$$\Big[\omega_0^2 + 4\omega_0\sigma_4 - 2i\gamma(\omega + n\Omega) - (\omega + n\Omega)^2\Big]P_n + 2\sigma_4\omega_0(P_{n+2} + P_{n-2}) = \frac{\varepsilon_b\,\omega_R^2}{4\pi}\,E_n. \tag{2.37}$$

If a comparison is made between the matrix problems for the third order case, found in Eq. (2.6), and the fourth order case above, then some differences are found. Firstly, the off-center diagonals have moved out one place. The mathematical origin of this change is due to the factor of two in the argument of the σ_4 cosine term in Eq. (2.1b). Physically, this term represents the TO-phonon transitions that are allowed because of the cubic anharmonicity, which governs a four phonon scattering channel where a TO-phonon scatters off two TA-phonons. The TO-phonon transitions that occur due to the cubic anharmonicity coupling the AW must be due to only even order transitions, that is n can only take even integer values. That two TA-phonons are involved in the scattering process is also the reason for $\sigma_4 \propto I_{\mathrm{ac}}$.

The second major difference between the third and fourth order matrix problems is the appearance of the static σ_4 term that is found on the central diagonal. The third order coupling of the previous section had no direct influence on the TO-phonon component of the polariton. The static term in the central diagonal of the matrix for the fourth order problem changes this. This term induces a static blue shift of the TO-phonon frequency that for $I_{\mathrm{ac}} \neq 0$. This term is an acoustical analog of the Stark shift briefly discussed in Chapter 1.

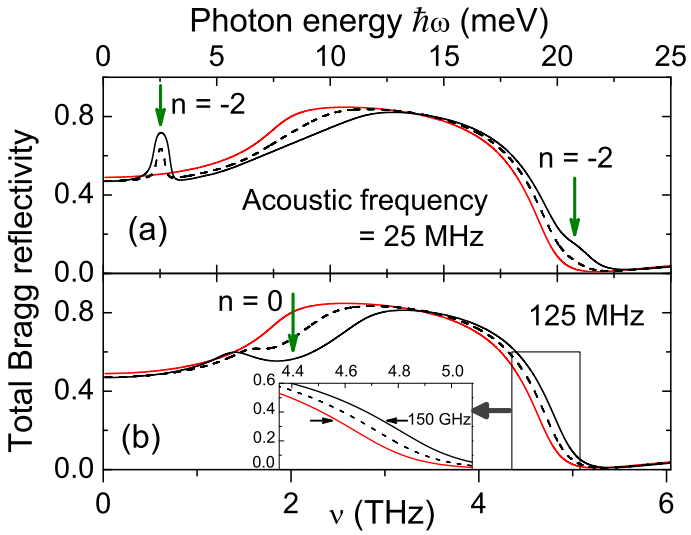

Figure 2.16: The total Bragg reflectivity for TlCl driven by an AW. (a) shows the reflectivity $\nu = 25$ MHz and (b) for $\nu = 125$ MHz. The acoustic intensity used to calculate the black dashed line is $I_{ac} = 100$ kW cm^{-2} corresponding to a coupling constant of $\sigma \sim 0.4$ meV, for the black solid line $I_{ac} = 200$ kW cm^{-2} ($\sigma \sim 0.8$ meV). The red line is the bare polariton reflectivity ($I_{ac} = 0$ kW cm^{-2}). The inset highlights the acoustically induced Stark shift of the TO-phonon polariton resonance.

In the optical Stark effect a semiconductor is pumped with a low power laser to generate a population of excitons. A laser with a higher power is then used to induce the Stark effect and of the excitons by energy ΔE [2]. This was explained as the photons from the high power laser dressing the excitons, which caused the nearly degenerate ground and exciton state to split and resulted in the probe beam generating polariton transitions [3]. Our case the acoustic wave generates the Stark blueshift rather than a high power pumping laser. The TO-phonon polaritons are dressed by TA-phonons leading to a shift in ω_0.

This Stark shift can be seen in the inset of Figure 2.16 (b), where the dashed black and solid black lines show the reflectivity for $\sigma \sim 0.4$ and $\sigma \sim 0.8$, respectively. It is clear that the blue shift caused by the acoustically Stark effect is tunable through the use of the coupling strength. The sharpest contrast for the Stark shift can be found at the blue edge of the Restrahlen band, where the blue shift is shown to measure ~ 0.15 THz.

There is, however, many similarities between the third and fourth order cases, which can be illustrated by the optical properties of the material. In Figure 2.16 the total

Bragg reflectivity is shown for two AW frequencies, one in the low range $\nu = 25$ MHz and one in the high $\nu = 125$ MHz, both for room temperature. In the low range frequency value the peaks in the reflectivity occur, in an similar fashion to the third order case. That is, TO-phonon transitions lead to acoustically induced band gaps and the peaks seen in Figure 2.16 (a). The only difference is that the lowest order Bragg replicas shown for the fourth order problem are equivalent to the second order Bragg replicas for the third order problem. This is the meaning of the $n = -2$ arrow in Figure 2.16 (a) in both the UP and LP branches.

At high frequencies, an example of which is shown in Figure 2.16 (b), the cusp-like feature appears due to the same physics as in the third order RAO effect. It is again caused by the accumulation of acoustically induced band gaps near the TO-phonon frequency. This modification of the total Bragg reflectivity spectrum, as in third order RAO effect, overwhelmingly occurs in the zeroth Bragg replica. The AW induced modulation of the material becomes too fine to be resolved by the TO-phonon polaritons, which leads to the AW modifications of the spectrum occurring only in the zeroth Bragg replica.

2.6 Summary

This chapter has covered the RAO effect for individual coupling between the TA and TO-phonons using anharmonic three- and four-phonon scattering channels. Using a modified dispersionless Hopfield macroscopic equation the numerical model was derived (see Appendix A) and the result of the analytical model found in [35] were presented. Using these models the AW induced TO-phonon transitions were investigated and found to lead to peaks in the total Bragg reflectivity spectrum of semi-infinite CuCl and TlCl crystal. It was shown that due to the resonant nature of the scattering process in the RAO effect, the spectral position of these peak could be modified by altering the AW frequency. The strength of the peaks was shown to be modifiable due to via the acoustic intensity.

The investigation of the reflectivity peaks showed that, for both CuCl and TlCl, the contribution of each Bragg replica to the total Bragg reflectivity was dependent of detuning from the Restrahlen band in the LP branch. It was found that at very high and very low detuning the contribution from the higher Bragg replicas was severely

reduced thanks the discrepancy between the AW modulation period and the TO-phonon polariton wavelength. It was also shown that the peaks become cusp-like at low detuning in LP due to an accumulation of AW induced band gaps. This also happens in the UP branch, but does not cause the same cusp-like feature. An investigation of the electric field and interaction length in CuCl showed considerable improvements over the *conventional* acousto-optic effect.

Finally, there where differences in the physics behind the third order RAO effect (CuCl) and the fourth order RAO effect (TlCl). In the fourth order effect the AW only induces even order (n even) TO-phonon transitions due to the scattering channel used. This means that the first order band gap in TlCl was equivalent to the second order band gap in CuCl. Also an acoustically induced renormalisation of the TO-phonon frequency was documented in the fourth order effect that has not been predicted in the third.

3 Resonant Acousto-Optics with TO-Phonons: Two Anharmonic Terms in the Lattice Potential

This chapter will focus on the RAO effect in $LiNbO_3$, which is a ferroelectric material. This class of material necessarily displays large phonon anharmonicities. The temperature dependent phase transition of the soft phonon mode, which is responsible for the ferroelectric behavior above the critical temperature, is evidence of a strongly anharmonic interatomic potential. In the case of $LiNbO_3$ the quartic anharmonicity, while weaker than the cubic, is still strong enough to have a relatively large effect on the optical properties of the material. Therefore, they will be considered simulataneously and on an equal footing.

3.1 Anharmonic Coupling Strength

This section estimates the coupling constants of both m_3 and m_4, which are the coupling constants for the cubic and quartic anharmonicity respectively, to an order of magnitude [34, 37]. These terms are related to the coupling strengths of the previous chapter by $\sigma_3 = m_3 I_{ac}^{1/2}$ and $\sigma_4 = m_4 I_{ac}$.

3.1.1 Cubic Anharmonic Coupling Constant

In Section 1.6 the anharmonicity of an ideal crystal was discussed, the cubic term of the anharmonic Hamiltonian is

$$H^{(3)} = V \begin{pmatrix} \mathbf{q}_1 & \mathbf{q}_2 & \mathbf{q}_3 \\ j_1 & j_2 & j_3 \end{pmatrix} (b_{j_1,\mathbf{q}_1} + b^\dagger_{j_1,-\mathbf{q}_1})(b_{j_2,\mathbf{q}_2} + b^\dagger_{j_2,-\mathbf{q}_2})(b_{j_3,\mathbf{q}_3} + b^\dagger_{j_3,-\mathbf{q}_3})$$

and $V(\mathbf{q}_1, \mathbf{q}_2, \mathbf{q}_3)$ is the cubic anharmonic potential given in Eq. (1.10). In the semi-infinite 1D geometry considered here the phonon polarization factors are unity. Thus, Eq. (1.10) can be rewritten as [16, 38, 39]

$$V \begin{pmatrix} \mathbf{q}_1 & \mathbf{q}_2 & \mathbf{q}_3 \\ j_1 & j_2 & j_3 \end{pmatrix} = \frac{\rho V_0}{3!} \left[\frac{\hbar^3}{8(\rho V_0)^3 \omega(\mathbf{q}_1 j_1)\omega(\mathbf{q}_2 j_2)\omega(\mathbf{q}_3 j_3)} \right]^{1/2} \Psi(\mathbf{q}_1, \mathbf{q}_2, \mathbf{q}_3) \tag{3.1}$$

where ρ is the mass density and V_0 is the lattice volume and [39],

$$\Psi(\mathbf{q}_1, \mathbf{q}_2, \mathbf{q}_3) = \frac{1}{\rho V_0} \sum_{\alpha,\beta,\gamma} \frac{\partial^3 V}{\partial \mathbf{u}_\alpha \partial \mathbf{u}_\beta \partial \mathbf{u}_\gamma} e^{i(\mathbf{q}_1 \cdot \mathbf{u}_\alpha + \mathbf{q}_2 \cdot \mathbf{u}_\beta + \mathbf{q}_3 \cdot \mathbf{u}_\gamma)}, \tag{3.2}$$

where $\mathbf{u}_\alpha$ are the atomic displacements along the α direction and α, β and γ are indices over the coordinates.

In the case of the RAO effect the interaction for the cubic anharmonic coupling is given by $TO + TA \rightarrow TO$, which corresponds to the $b_{\mathrm{TO},\mathbf{k}} \cdot b_{\mathrm{TA},\mathbf{K}} \cdot b_{\mathrm{TO},\mathbf{k}+\mathbf{K}}$. Thus, the wavevectors take the values $\mathbf{q}_1 = \mathbf{k}$, $\mathbf{q}_2 = \mathbf{K}$ and $\mathbf{q}_3 = -\mathbf{k} - \mathbf{K}$ and the Hamiltonian of the associated cubic anharmonicity is

$$H^{(3)}_{\mathrm{RAO}} \approx V \begin{pmatrix} \mathbf{k} & \mathbf{K} & \mathbf{k}+\mathbf{K} \\ j_{\mathrm{TO}} & j_{\mathrm{TA}} & j_{\mathrm{TO}} \end{pmatrix} (b_{j_{\mathrm{TO}},\mathbf{k}} + b^\dagger_{j_{\mathrm{TO}},-\mathbf{k}})(b_{j_{\mathrm{TA}},\mathbf{K}} + b^\dagger_{j_{\mathrm{TA}},-\mathbf{K}})(b_{j_{\mathrm{TO}},-\mathbf{k}-\mathbf{K}} + b^\dagger_{\mathbf{k}+\mathbf{K}}). \tag{3.3}$$

The phonon branches involved are $j_1 = j_{\mathrm{TO}}$, $j_2 = j_{\mathrm{TA}}$ and $j_3 = j_{\mathrm{TO}}$. By assuming that $\omega(\mathbf{k}, j_{\mathrm{TO}}) = \omega(\mathbf{k}+\mathbf{K}, j_{\mathrm{TO}}) = \omega_0$ the potential can be written as

$$V \begin{pmatrix} \mathbf{k} & \mathbf{K} & \mathbf{k}-\mathbf{K} \\ j_{\mathrm{TO}} & j_{\mathrm{TA}} & j_{\mathrm{TO}} \end{pmatrix} = \frac{\rho V_0}{3!} \left(\frac{\hbar^3}{8(\rho V_0)^3 \omega_0^2 \Omega} \right)^{1/2} \Psi(\mathbf{k}, \mathbf{K}, \mathbf{k}-\mathbf{K}) \tag{3.4}$$

To proceed it is necessary to find a value for $\Psi(\mathbf{k}, \mathbf{K}, \mathbf{k}-\mathbf{K})$. As there is little literature on this specific interaction an estimate is required.

According to Guerevich [39] we can make an order of magnitude approximation of the derivative in Eq. (3.2). Consider an atom displaced from equilibrium by an interatomic distance a. The energy of this displacement is of the order of a typical atomic energy ϵ_a, as a result the order of magnitude estimate is

$$\frac{\partial^3 V}{\partial \mathbf{u}_\alpha \partial \mathbf{u}_\beta \partial \mathbf{u}_\gamma} \approx \frac{\epsilon_a}{a^3},$$

where ϵ_a can be expressed in characteristic quantities of the crystal. As the crystal is invariant to a transform of a, the exponential term in Eq. (3.2) remains unaffected provided $|\mathbf{u}_\alpha - \mathbf{u}_\beta| << 1$ and $|\mathbf{u}_\alpha - \mathbf{u}_\gamma| << 1$.

The elastic energy of the displacement in the harmonic approximation is $(1/2)\lambda_{ilmn} u_{il} u_{mn}$, where λ_{ilmn} is the fourth order elastic tensor and u_{il} is the second order strain tensor. As the atomic displacement is small the harmonic approximation holds, and the deformation potentials are unity. The elastic coefficients can be approximated as $\lambda_{ilmn} \sim \rho \bar{v}_{\text{ac}}^2$, where $\bar{v}_{\text{ac}}$ is the average acoustic velocity. The total elastic energy of the crystal can also be written as $ns\epsilon_a$, where n is the density of unit cells and s the number of atoms per unit cell. This leads to $\rho \bar{v}_{\text{ac}}^2 = ns\epsilon_a$. Rearranging and canceling gives $\epsilon_a \sim \bar{m} \bar{v}_{ac}^2$, where $\bar{m} = M/s$ is the average mass of an atom and M is the mass of the crystal. It is now possible to rewrite the derivative as

$$\frac{\partial^3 V}{\partial \mathbf{u}_\alpha \partial \mathbf{u}_\beta \partial \mathbf{u}_\gamma} \approx \frac{\bar{m} \bar{v}_{\text{ac}}^2}{a^3}.$$

The sum in Eq. (3.2) can now be estimated. First the indices need to be changed to $\mathbf{u}_\alpha$, $\mathbf{u}_\alpha - \mathbf{u}_\beta$ and $\mathbf{u}_\alpha - \mathbf{u}_\gamma$, which can done by considering the exponential term in Eq. (3.2)

$$e^{i(\mathbf{q}_1 \cdot \mathbf{a}_\alpha + \mathbf{q}_2 \cdot \mathbf{a}_\beta + \mathbf{q}_3 \cdot \mathbf{a}_\gamma)} = e^{i[\mathbf{q}_2 \cdot (\mathbf{a}_\beta - \mathbf{a}_\alpha) + \mathbf{q}_2 \cdot (\mathbf{a}_\gamma - \mathbf{a}_\alpha)]} e^{i(\mathbf{q}_1 + \mathbf{q}_2 + \mathbf{q}_3)\mathbf{a}_\alpha}.$$

The anharmonic coefficient described by Eq.(3.1) must be invariant to a translation by a lattice vector [16, 40]. For phonon wavevectors, the conservation of momentum can be written as that $\mathbf{q}_1 + \mathbf{q}_2 + \mathbf{q}_3 = \mathbf{g}$. Due to the invariance of the lattice a translation of $\mathbf{a}$ obeys $\mathbf{a} \cdot \mathbf{g} = 0$. Therefore, $\Psi(\mathbf{q}_1, \mathbf{q}_2, \mathbf{q}_3)$ can be written as

$$\Psi(\mathbf{q}_1, \mathbf{q}_2, \mathbf{q}_3) \approx \frac{1}{\rho V_0} N_0 \frac{\bar{m} \bar{v}_{ac}^2}{a^3} \sum_{\alpha-\beta, \alpha-\gamma} e^{i[\mathbf{q}_2 \cdot (\mathbf{a}_\alpha - \mathbf{a}_\beta) + \mathbf{q}_3 \cdot (\mathbf{a}_\alpha - \mathbf{a}_\gamma)]},$$

where the factor of $N_0 = \rho V_0/\bar{m}$ is the number atoms in the lattice and comes from the completion of the sum over α [39]. The displacement of the atom is small, only of an average interatomic distance $\bar{a}$. Thus, the number of terms that need to be considered in the sum approaches unity [39]. Therefore, the summation is small and Ψ can be approximated as

$$\Psi(\mathbf{q}_1, \mathbf{q}_2, \mathbf{q}_3) \approx \frac{\bar{v}_{ac}^2}{\bar{a}^3}.$$

This approximation no longer holds when one of the phonons is from an acoustic branch and whose magnitude is small compared to $\bar{a}^{-1}$. In this case, $|\mathbf{K}|$ is far smaller than $\bar{a}^{-1}$ and as $|\mathbf{K}| \to 0$ the vibrations become a translation of the entire lattice. This motion cannot change the energy of the lattice. To ensure this is the case a factor of $|\mathbf{K}|\bar{a}$ is included [39] in the previous approximation

$$\Psi(\mathbf{k}, \mathbf{K}, \mathbf{k}') \approx |\mathbf{K}|\bar{a}\frac{\bar{v}_{ac}^2}{\bar{a}^3}.$$

The potential of the $TO + TA \to TO$ channel can now be written as,

$$V\begin{pmatrix} \mathbf{k} & \mathbf{K} & \mathbf{k}-\mathbf{K} \\ j_{\mathrm{TO}} & j_{\mathrm{TA}} & j_{\mathrm{TO}} \end{pmatrix} \approx \frac{1}{3!}\left[\frac{\hbar^3}{8\bar{\mu}^3\omega_0^2\Omega}\right]^{1/2}|\mathbf{K}|\bar{a}\frac{\bar{v}_{ac}^2}{\bar{a}^3}, \tag{3.5}$$

where $\bar{\mu}$ is the average effective mass of the phonon modes.

A classical approximation of the acoustic phonon term in the Hamiltonian can be made by writing

$$\left\langle \frac{(b_{\mathbf{K}} + b_{-\mathbf{K}}^\dagger)}{\sqrt{V}_{\mathrm{cell}}} \right\rangle = \sqrt{N_{\mathrm{ph}}} = \left(\frac{I_{\mathrm{ac}}}{\hbar^3\bar{v}_{\mathrm{ac}}\Omega}\right)^{1/2}$$

which, with the aid of the acoustic dispersion $\Omega(\mathbf{K}) = v_{\mathrm{ac}}\mathbf{K}$, allows the Hamiltonian to be approximated as

$$H_{\mathrm{RAO}}^{(3)} \approx V\begin{pmatrix} \mathbf{k} & \mathbf{K} & \mathbf{k}-\mathbf{K} \\ j_{\mathrm{TO}} & j_{\mathrm{TA}} & j_{\mathrm{TO}} \end{pmatrix}\left(\frac{I_{\mathrm{ac}}}{\hbar^3\mathbf{K}\bar{v}_{\mathrm{ac}}^2}V_{\mathrm{cell}}\right)^{1/2}(b_{j_{\mathrm{TO}},\mathbf{k}} + b_{j_{\mathrm{TO}},-\mathbf{k}}^\dagger)(b_{j_{\mathrm{TO}},\mathbf{k}-2\mathbf{K}} + b_{j_{\mathrm{TO}},-\mathbf{k}+2\mathbf{K}}^\dagger), \tag{3.6}$$

where $V(\mathbf{k}, \mathbf{K}, \mathbf{K}, \mathbf{k}-\mathbf{K})$ is defined in Eq. (3.5). The cubic anharmonic coupling

Table 3.1: Parameters for bulk $LiNbO_3$ used to calculate m_3 and m_4.

	$LiNbO_3$
V_0	3.17941×10^{22} cm^3
$v_{\rm ac}$	357290 cms^{-1}
$\lvert V(Q_0)\rvert$	18.2 mRy
$\bar{a}$	1.386×10^{-7} cm

constant σ_3 can be define as

$$\sigma_3 = 3!V \begin{pmatrix} \mathbf{k} & \mathbf{K} & \mathbf{k}-\mathbf{K} \\ j_{\rm TO} & j_{\rm TA} & j_{\rm TO} \end{pmatrix} \left(\frac{I_{\rm ac}}{\hbar \mathbf{K} v_{\rm ac}^2} V_{\rm cell} \right)^{1/2}, \tag{3.7}$$

where the factor of 3! is to account for the permutation of phonon branches. This equation is related to the third order coupling strength m_3 given in chapter 2 by $\sigma_3 = m_3\sqrt{I_{\rm ac}}$.

For the ferroelectric materials $LiNbO_3$ and $LiTaO_3$ the value of the magnitude of the derivative $\Psi(\mathbf{k}_1, \mathbf{k}_2, \mathbf{k}_3)$ has been empirically deduced [29]

$$\Psi_{\rm LiNbO_3}(\mathbf{k}_1, \mathbf{k}_2, \mathbf{k}_3) = \left(\frac{3\bar{\mu}^3 \omega_0^6}{16|V(Q_0)|} \right)^{1/2},$$

where $V(Q_0)$ are the minima of the interatomic ferroelectric potential. By applying the small $|\mathbf{K}|$ approximation of Gurevich discussed previously we can write

$$\Psi_{\rm LiNbO_3}(\mathbf{k}, \mathbf{K}, \mathbf{k}-\mathbf{K}) \approx \left(\frac{3\bar{\mu}^3 \omega_0^6}{16|V(Q_0)|} \right)^{1/2} |\mathbf{K}|\bar{a}.$$

The combination of this result with Eq. (3.4) and Eq. (3.7), after some manipulation, leads to

$$\sigma_3^{\rm LiNbO_3} = \frac{3}{8} \left[\frac{V_{\rm cell}\omega_0^4}{v_{ac}^3 |V(Q_0)|} \right]^{1/2} \bar{a} I_{\rm ac}^{1/2}. \tag{3.8}$$

Upon comparison with $\sigma_3 = m_3\sqrt{I_{\rm ac}}$ this gives the cubic anharmonic coupling constant for the ferroelectric materials $LiNbO_3$ and $LiTaO_3$ as

$$m_3 = \frac{3}{8} \left[\frac{V_{\rm cell}\omega_0^4}{v_{ac}^3 |V(Q_0)|} \right]^{1/2} \bar{a}. \tag{3.9}$$

Using the data provided in Table 3.1 [41, 42] $\sigma_3^{\mathrm{LiNbO_3}} \approx 1$ meV for $I_{\mathrm{ac}} = 1$ kWcm^{-2}. Throughout this chapter $I_{ac} = 25$ kWcm^{-2} which gives $\sigma_3^{\mathrm{LiNbO_3}} \approx 5$ meV. For the remainder of this chapter $LiNbO_3$ is the only material considered, for brevity the superscript will be dropped from $\sigma_3^{\mathrm{LiNbO_3}}$.

3.1.2 Quartic Anharmonic Coupling Constant

The quartic anharmonic term of the Hamiltonian of an ideal crystal is

$$H^{(4)} = V \begin{pmatrix} \mathbf{q}_1 & \mathbf{q}_2 & \mathbf{q}_3 & \mathbf{q}_4 \\ j_1 & j_2 & j_3 & j_3 \end{pmatrix} (b_{j_1,\mathbf{q}_1} + b^\dagger_{j_1,-\mathbf{q}_1})(b_{j_2,\mathbf{q}_2} + b^\dagger_{j_2,-\mathbf{q}_2})(b_{j_3,\mathbf{q}_3} + b^\dagger_{j_3,-\mathbf{q}_3})(b_{j_4,\mathbf{q}_4} + b^\dagger_{j_4,-\mathbf{q}_4})$$

and the $V(\mathbf{q}_1, \mathbf{q}_2, \mathbf{q}_3, \mathbf{q}_4)$ is the quartic anharmonic potential. As mentioned in the previous sub-section the TO-phonon polarization factors are unity, as a result the potential is

$$V \begin{pmatrix} \mathbf{q}_1 & \mathbf{q}_2 & \mathbf{q}_3 & \mathbf{q}_4 \\ j_1 & j_2 & j_3 & j_3 \end{pmatrix} = \frac{\rho V_0}{4!} \left[\frac{\hbar^4}{16\rho \bar{V}_0{}^4 \omega(\mathbf{q}_1 j_1)\omega(\mathbf{q}_2 j_2)\omega(\mathbf{q}_3 j_3 \omega(\mathbf{q}_4 j_3)} \right]^{1/2} \Phi(\mathbf{q}_1, \mathbf{q}_2, \mathbf{q}_3, \mathbf{q}_4) \tag{3.10}$$

and,

$$\Phi(\mathbf{q}_1, \mathbf{q}_2, \mathbf{q}_3, \mathbf{q}_4) = \frac{1}{\rho V_0} \sum_{\alpha,\beta,\gamma,\varsigma} \frac{\partial^3 V}{\partial \mathbf{u}_\alpha \partial \mathbf{u}_\beta \partial \mathbf{u}_\gamma \partial \mathbf{u}_\varsigma} e^{i(\mathbf{q}_1 \cdot \mathbf{u}_\alpha + \mathbf{q}_2 \cdot \mathbf{u}_\beta + \mathbf{q}_3 \cdot \mathbf{u}_\gamma + \mathbf{q}_4 \cdot \mathbf{u}_\varsigma)}, \tag{3.11}$$

where α, β, γ and ς are indices over the coordinates.

In the case of the RAO effect the interaction for the quartic anharmonic coupling is given by $TO{+}TA{+}TA \rightarrow TO$, which corresponds to the $b_{\mathrm{TO},\mathbf{k}} \cdot b_{\mathrm{TA},\mathbf{K}} \cdot b_{\mathrm{TA},\mathbf{K}} \cdot b_{\mathrm{TO},\mathbf{k}+2\mathbf{K}}$. Thus, the wavevectors take the values $\mathbf{q}_1 = \mathbf{k}$, $\mathbf{q}_2 = \mathbf{K}$, $\mathbf{q}_3 = \mathbf{K}$ and $\mathbf{q}_4 = \mathbf{k} - 2\mathbf{K}$ and the Hamiltonian of the associated quartic anharmonicity is

$$H^{(3)}_{\mathrm{RAO}} \approx V \begin{pmatrix} \mathbf{k} & \mathbf{K} & \mathbf{K} & \mathbf{k} - 2\mathbf{K} \\ j_{\mathrm{TO}} & j_{\mathrm{TA}} & j_{\mathrm{TA}} & j_{\mathrm{TO}} \end{pmatrix} (b_{j_{\mathrm{TO}},\mathbf{k}} + b^\dagger_{j_{\mathrm{TO}},-\mathbf{k}})(b_{j_{\mathrm{TA}},\mathbf{K}} + b^\dagger_{j_{\mathrm{TA}},-\mathbf{K}})$$
$$(b_{j_{\mathrm{TA}},\mathbf{K}} + b^\dagger_{j_{\mathrm{TA}},-\mathbf{K}})(b_{j_{\mathrm{TO}},\mathbf{k}-2\mathbf{K}} + b^\dagger_{j_{\mathrm{TO}},-\mathbf{k}+2\mathbf{K}}). \tag{3.12}$$

The phonon branches involved are $j_1 = j_{\mathrm{TO}}$, $j_2 = j_3 = j_{\mathrm{TA}}$ and $j_4 = j_{\mathrm{TO}}$. Similar to the previous section it is assumed that $\omega(\mathbf{k}, j_{\mathrm{TO}}) = \omega(\mathbf{k} - \mathbf{2K}, j_{\mathrm{TO}}) = \omega_0$, which

allows the potential to be written as

$$V\begin{pmatrix} \mathbf{k} & \mathbf{K} & \mathbf{K} & \mathbf{k}-2\mathbf{K} \\ j_{\mathrm{TO}} & j_{\mathrm{TA}} & j_{\mathrm{TA}} & j_{\mathrm{TO}} \end{pmatrix} = \frac{\rho V_0}{4!}\left(\frac{\hbar^4}{16\bar{\mu}^4\omega_0^2\Omega^2}\right)^{1/2}\Phi(\mathbf{k},\mathbf{K},\mathbf{K},\mathbf{k}-2\mathbf{K}) \quad (3.13)$$

Once again it necessary to find a value for $\Phi(\mathbf{k},\mathbf{K},\mathbf{K},\mathbf{k}-2\mathbf{K})$ to proceed. Like the previous sub-section there is little literature on this specific quartic anharmonic interaction so an estimate is required.

As in the last subsection, we apply Gurevich's approximation to provide a value for the derivative in $\Phi(\mathbf{k},\mathbf{K},\mathbf{K},\mathbf{k}-2\mathbf{K})$. Extending the logic of Gurevich [39], the atomic displacement argument used in the last subsection approximates the fourth order derivative as

$$\frac{\partial^4 V}{\partial\mathbf{u}_\alpha\partial\mathbf{u}_\beta\partial\mathbf{u}_\gamma\partial\mathbf{u}_\zeta} \approx \frac{\bar{m}\bar{v}_{ac}^2}{a^4}.$$

As in the cubic case $\epsilon_a = \bar{m}\bar{v}_{\mathrm{ac}}^2$. The invariance of the lattice to a translation by a means the exponential in Eq. (3.11) term remains unaffected, provided $|\mathbf{u}_\alpha - \mathbf{u}_\beta| << 1$, $|\mathbf{u}_\alpha - \mathbf{u}_\gamma| << 1$ and $|\mathbf{u}_\alpha - \mathbf{u}_\varsigma| << 1$.

The arguments used in the cubic case to approximate the summations in $\Psi(\mathbf{q_1},\mathbf{q_2},\mathbf{q_3})$ appealed to the translational invariance of the potential $V(\mathbf{q_1},\mathbf{q_2},\mathbf{q_3})$ and conservation of phonon momentum. In the quartic case discussed here these arguments still hold, $V(\mathbf{q_1},\mathbf{q_2},\mathbf{q_3},\mathbf{q_4})$ is also invariant to a translation by $\mathbf{a}$ and the four phonon interaction also obeys conservation of momentum. Also the same system is under consideration so the sums will also evaluate to the same values. Thus, we can approximate $\Phi(\mathbf{q_1},\mathbf{q_2},\mathbf{q_3},\mathbf{q_4})$ as

$$\Phi(\mathbf{q}_1,\mathbf{q}_2,\mathbf{q}_3,\mathbf{q}_4) \approx \frac{\bar{v}_{ac}^2}{a^4}.$$

As in the cubic case this approximation breaks down when the long wavelength acoustic phonons are present. However, in this case the quartic interaction involves two acoustic phonons and therefore the approximation becomes

$$\Phi(\mathbf{k},\mathbf{K},\mathbf{K},\mathbf{k}') \approx (|\mathbf{K}|\bar{a})^2\frac{\bar{v}_{ac}^2}{a^4}.$$

Where the factor of $(|\mathbf{K}|\bar{a})^2$ corrects for both acoustic phonons. The potential of the

$TO + TA + TA \rightarrow TO$ channel can now be written as,

$$V\begin{pmatrix} \mathbf{k} & \mathbf{K} & \mathbf{K} & \mathbf{k}-2\mathbf{K} \\ j_{\mathrm{TO}} & j_{\mathrm{TA}} & j_{\mathrm{TA}} & j_{\mathrm{TO}} \end{pmatrix} = \frac{\rho V_0}{4!}\left(\frac{\hbar^4}{16\bar{\mu}^4\omega_0^2\Omega^2}\right)^{1/2}(|\mathbf{K}|\bar{a})^2\frac{\bar{v}_{ac}^2}{a^4}. \tag{3.14}$$

The same classical approximation can be applied to $H^{(4)}_{\mathrm{RAO}}$ as to $H^{(3)}_{\mathrm{RAO}}$. As there are two $(b_K + b_K^\dagger)$ terms the Hamiltonian to be approximated as

$$H^{(4)}_{\mathrm{RAO}} \approx V\begin{pmatrix} \mathbf{k} & \mathbf{K} & \mathbf{K} & \mathbf{k}-2\mathbf{K} \\ j_{\mathrm{TO}} & j_{\mathrm{TA}} & j_{\mathrm{TA}} & j_{\mathrm{TO}} \end{pmatrix}\frac{I_{\mathrm{ac}}}{\hbar^3\mathbf{K}\bar{v}_{\mathrm{ac}}^2}V_{\mathrm{cell}}(b_{j_{\mathrm{TO}},\mathbf{k}} + b^\dagger_{j_{\mathrm{TO}},-\mathbf{k}})(b_{j_{\mathrm{TO}},\mathbf{k}-2\mathbf{K}} + b^\dagger_{j_{\mathrm{TO}},-\mathbf{k}+2\mathbf{K}}), \tag{3.15}$$

where $V(\mathbf{k},\mathbf{K},\mathbf{K},\mathbf{k}-\mathbf{K})$ is defined in Eq. (3.14). Then, cubic anharmonic coupling constant σ_3 can be define as

$$\sigma_4 = 4!V\begin{pmatrix} \mathbf{k} & \mathbf{K} & \mathbf{K} & \mathbf{k}-2\mathbf{K} \\ j_{\mathrm{TO}} & j_{\mathrm{TA}} & j_{\mathrm{TA}} & j_{\mathrm{TO}} \end{pmatrix}\frac{I_{\mathrm{ac}}}{\hbar^3\mathbf{K}\bar{v}_{\mathrm{ac}}^2}V_{\mathrm{cell}}, \tag{3.16}$$

where the factor of 4! is to account for the permutation of phonon branches. This equation is related to the third order coupling strength m_3 given in chapter 2 by $\sigma_4 = m_4 I_{\mathrm{ac}}$.

For the ferroelectric materials $LiNbO_3$ and $LiTaO_3$ an empirical value for the magnitude of $\Phi(\mathbf{k}_1,\mathbf{k}_2,\mathbf{k}_3,\mathbf{k}_4)$ has been deduced [29]

$$|\Phi(\mathbf{k}_1,\mathbf{k}_2,\mathbf{k}_3,\mathbf{k}_4)| \approx \frac{3\bar{\mu}^2\omega_0^4}{64|V(Q_0)|}.$$

The small $|\mathbf{K}|$ approximation of Gurevich is applied, this time a factor of $(|\mathbf{K}|\bar{a})^2$ is included. Combining this approximation with Eq. (3.13) and Eq. (3.16) leads to

$$\sigma_4^{\mathrm{LiNbO_3}} = \frac{3}{8}\frac{V_{\mathrm{cell}}\omega_0^3}{v_{ac}^3|V(Q_0)|}\bar{a}^2 I_{\mathrm{ac}}^{1/2}. \tag{3.17}$$

Upon comparison with $\sigma_4 = m_4 I_{\mathrm{ac}}$ this gives the quartic anharmonic coupling constant for the ferroelectric materials $LiNbO_3$ and $LiTaO_3$ as

$$m_4 = \frac{3}{8}\left[\frac{V_{\mathrm{cell}}\omega_0^4}{v_{ac}^3|V(Q_0)|}\right]^{1/2}\bar{a}. \tag{3.18}$$

The data found in Table 3.1 [41, 42] gives $\sigma_4^{\mathrm{LiNbO_3}} \approx 0.01$ meV for $I_{\mathrm{ac}} = 1$ kWcm^{-2},

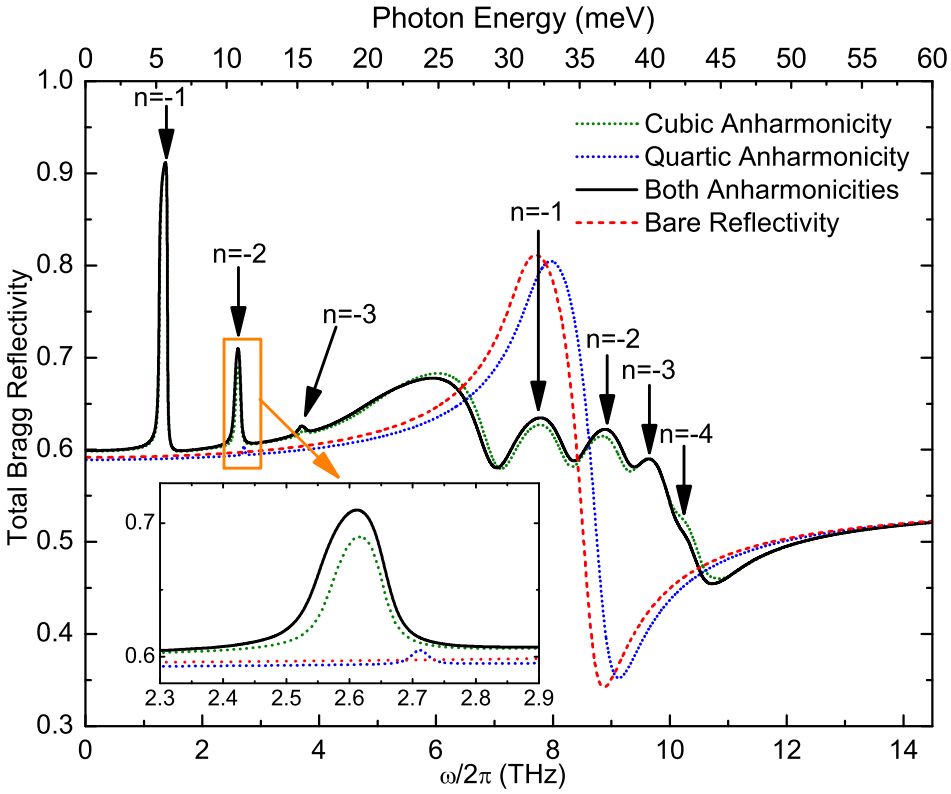

Figure 3.1: The solid black line shows the total Bragg reflectivity in which both cubic and quartic anharmonicity has been taken into account in $LiNbO_3$. The dotted green and blue lines show the total Bragg reflectivity due to the individual anharmonicities, the green line is the cubic anharmonicity and the blue line is the quartic anharmoncity. The reflectivity was calculated for $\nu_{\rm ac} = 250$ MHz and $I_{\rm ac} = 25$ kWcm^{-2}. The dashed red line is the bare TO-phonon polariton dispersion ($I_{ac} = 0$). The arrows label the peaks in the total Bragg reflectivity by the acoustically induced transition that is responsible for them.

for $I_{ac} = 25$ kWcm^{-2} the coupling strength is $\sigma_4^{\rm LiNbO_3} \approx 0.25$ meV. As with σ_3, for brevity the superscript will be dropped from $\sigma_4^{\rm LiNbO_3}$.

3.2 Comparison with the Case of One Anharmonicity

In the previous chapter the RAO effect due to only one anharmonicity was discussed, either for the cubic anharmoncity in CuCl or the quartic in TlCl. In this chapter the anharmonic coupling is strong enough that both anharmonicities must be considered on equal terms. While this leaves the numerical method of calculation unchanged, it does require a greater number of Bragg replicas to be taken into account. To produce

convergent dispersion branches for $I_{\rm ac} = 25$ kWcm^{-2} 400 Bragg replicas are required. The calculation of the total Bragg reflectivity requires far less Bragg replicas to be taken into account, roughly 40 are required for a precision of 10^{-7}.

The calculation proceeds by substituting the estimations produced in the previous section for σ_3 and σ_4 in Eq. (2.1b). This gives the material equation

$$\left[\frac{\partial^2}{\partial t^2} + 2\gamma_{\rm TO}\frac{\partial}{\partial t} + \omega_0^2 + 4\omega_0 m_4 I_{\rm ac} + 4\omega_0 m_3\sqrt{I_{\rm ac}}\cos(\Omega t - \mathbf{Kr} + \phi)\right.$$
$$\left. + 4\omega_0 m_4 I_{\rm ac}\cos(2\Omega t - 2\mathbf{Kr})\right]\mathbf{P}(\mathbf{r},t) = \frac{\varepsilon_{\rm b}}{4\pi}\omega_{\rm R}^2\mathbf{E}(\mathrm{r},t). \tag{3.19}$$

The two major differences with the previous chapter's case of one anharmoncity, are that both anharmonic terms are always present in Eq. (3.19) and that ϕ is not necessarily zero. This leads to the presence of both cubic and quartic anharmonic coupling between the TO-phonon component of the polariton and the TA-phonons of the bulk AW.

A comparison is made between the total Bragg reflectivity for each individual anharmonic coupling component and both components together in Figure. 3.1, which was calculated for $\nu_{\rm ac} = 250$ MHz and $I_{\rm ac} = 25$ kWcm^{-2}. The solid black line gives the total Bragg reflectivity spectrum for both the anharmonic contributions and the dashed red line for the bare TO-phonon polariton spectrum. The dashed lines are the individual anharmonic components of the RAO effect in $LiNbO_3$. The green line takes into account only the cubic anharmonic effect. Thus, the total Bragg reflectivity is formed by the acoustically induced band gaps of every transition, similar to CuCl investigated in the previous chapter. The dashed blue line is due solely to the quartic anharmonicity, accordingly only the even order acoustically induced transitions affect this line, as in TlCl discussed in the previous chapter.

Consider the peaks due to odd n TO-phonon transitions in Figure. 3.1. The total Bragg reflectivity for both anharmonicities (solid black lines) at these transitions is clearly very similar to the peaks due to cubic anharmonicity only (green dashed line). This is because the cubic component is the only contributor to the odd peaks, which is apparent from comparison of the two modulating terms in Eq. (3.19). The even n peaks have contributions from both the cubic and quartic scattering channels. Thus, discrepancies occur between the total Bragg reflectivity due to the third order and both anharmonicities at the even n peaks. This can be seen in the inset to Figure. 3.1. The apparent weakness of the quartic anharmonicity is very clear in this inset, the

total Bragg reflectivity due to this scattering channel (blue dashes) is considerably smaller than the cubic equivalent. However, from the difference between the cubic peak and the peak due to both anharmonicities, it is clear that the fourth order transition contributes significantly to the even n peaks.

In Figure. 3.1 the quartic only total Bragg reflectivity displays a blue shift with respect to the bare TO-phonon line. This is the Stark shift discussed in the previous chapter, which is due to the static quartic anharmonic term $4\omega_0 m_4 I_{\rm ac}$ in Eq. (3.19). This shift can be seen in the UP branch, $n = -2$ transition in the total Bragg reflectivity for both anharmonicities. However, it is not so clear in the total Bragg reflectivity for both anharmonicities. This is because the quasi-continuum that exist in the dispersion associated with the RAO effect over compensates for the Stark shift. A large increase in $I_{\rm ac}$ would increase the magnitude of the Stark shift but would also increase the strength of the quasi-continuum. Unfortunately, for $I_{\rm ac}$ of large magnitude the number of replicas required to calculate the dispersion becomes prohibitively large.

The introduction of two non-zero amplitude sinusoidal modulations in Eq. (3.19), leads to the introduction of one further parameter. The phase is a material parameter that cannot be accessed and varied experimentally. However, there is no literature on this parameter for $LiNbO_3$. The phase difference between these two terms has an impact on the reflectivity and extinction of a material undergoing the RAO effect. This parameter controls the degree to which the modulations interfere with each other, leading to variations in the strength of the coupling between the TO-phonon component of the polariton and the AW for even n TO-phonon transitions.

3.3 Phase Dependence

In this section the difference in phase between the third and quartic anharmonic effects of the acoustic modulation are discussed. Clearly, a class of material with more than one large anharmonic coefficient is necessary to access an anharmonic phase difference. It is for this reason that neither CuCl or TlCl, discussed in the previous chapter, are suitable. However, the ferroelectric material $LiNbO_3$ has very strong third order anhamonic coupling constant and the fourth order coupling constant, while much weaker, is of sufficient strength to be treated on an equal footing. These values have been estimated in the first section of this chapter. The other parameters

necessary for the calculation of the optical properties of acoustically excited $LiNbO_3$ are $\omega_{\mathrm{TO}} = 31\,\mathrm{meV}$, $\omega_R = 18.0\,\mathrm{meV}$, $\gamma_{\mathrm{TO}} = 1.26\,\mathrm{meV}$ and $\varepsilon_b = 44$ [43].

Previously, it has been assumed that the matrix element between the AW and the polarization component of the TO-phonon polariton is purely real. If this assumption of reality is dropped in Eq. (2.5) then anharmonic coupling terms can be expressed as,

$$(|\sigma_3|e^{-i\phi_3}e^{-i\Omega t}b_k^\dagger b_{k-K}^\dagger + H.C.) + (|\sigma_4|e^{-i\phi_4}e^{-2i\Omega t}b_k^\dagger b_{k-2K}^\dagger + H.C.),$$

where the amplitudes and the phases of the coupling constants were introduced $\sigma_{3,4} = |\sigma_{3,4}|e^{i\phi_{3,4}}$. In the material equation Eq. (2.1b) the corresponding coupling terms are given by

$$|\sigma_3|\cos(\Omega t - \mathbf{Kr} - \phi_3) + |\sigma_4|\cos(2\Omega t - 2\mathbf{Kr} - \phi_4),$$

where the constant prefactor of ω_0 has been dropped. Introducing a temporal offset $t' = t + t_0$ requires a change of variables, which allow the coupling terms to be written as

$$|\sigma_3|\cos[\Omega(t' - t_0) - \mathbf{Kr} - \phi_3] + |\sigma_4|\cos[2\Omega(t' - t_0) - 2\mathbf{Kr} - \phi_4]. \tag{3.20}$$

By choosing $t_0 = -\phi_4/2\Omega$ we can remove ϕ_4 from Eq. (3.20), this yields

$$|\sigma_3|\cos\left[\Omega\left(t' + \frac{\phi_4}{2\Omega}\right) - \mathbf{Kr} - \phi_3\right] + |\sigma_4|\cos(2\Omega t' - 2\mathbf{Kr}).$$

Then by defining $\phi = -\phi_3 + \phi_4/2$ and redefining $t = t'$, the usual coupling terms found in Eq. (2.1b) can be written as

$$|\sigma_3|\cos(\Omega t - \mathbf{Kr} + \phi) + |\sigma_4|\cos(2\Omega t - 2\mathbf{Kr}).$$

Throughout the remainder of this work the effect that phase term will have on the coupling strength will be referred to with the terms destructive and constructive interference. It will be shown that the effect the phase has on the phonon-phonon coupling strength will similar to the effect a phase term between two oscillations. This is due to the oscillating factors in the cubic and quartic coupling terms. A decrease in the absolute strength of the coupling will be observed in the reflectivity plots for specific values of ϕ that is analogous to interference effects see in coherent oscillations.

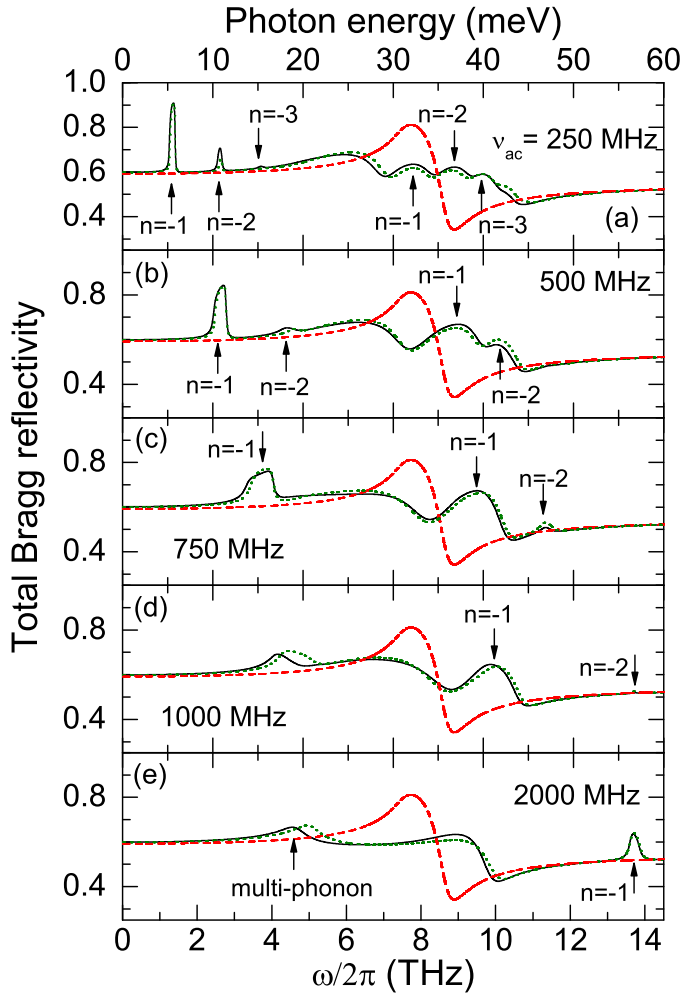

Figure 3.2: (a) to (e) show the development the THz reflectivity of $LiNbO_3$ with varying acoustic frequency and different phase shift between the cubic and quartic anharmonic parameters, $\phi = 0$ (black solid lines) and $\phi = \pi/2$ (green dotted lines). The red dashed line is the reflectivity spectrum at $I_{\text{ac}} = 0$.

The acoustic intensity effects the acoustically induced band gaps in $LiNbO_3$ in the same way as in the previous materials studied. The variation of the coupling strength for the cubic anharmonicity is still as the root of I_{ac}. For the quartic anharmonicity the coupling strength varies linearly in I_{ac}. Throughout this chapter $I_{\text{ac}} = 25$ kW/cm^2, unless otherwise stated, giving a third order coupling strength of $\sigma_3 = 5.02$ meV and a fourth order coupling strength of $\sigma_4 = 0.27$ meV. Despite the order of magnitude discrepancy between the two coupling strengths the interference effects are relatively pronounced.

Figure. 3.2 shows the effect of the variation of frequency for the extreme values of constructive and destructive interference on the total Bragg reflectivity. As in previous

chapters the bare reflectivity (I_{ac}=0) is given by the dashed red line, the black solid lines give the case of constructive interference $\phi = 0$ and the green dotted lines give the case of destructive interference $\phi = \pi/2$. The arrows show the position of the TO-phonon transition discussed previously. For frequencies away from the TO-phonon polariton restrahlen band, the spectral position of the transitions remain unaffected by anharmonic phase shift. Therefore, the peaks in the reflectivity associated with these transition still occur at the Bragg condition, $\omega = \omega_{pol}(nK/2)$, where $\omega_{pol}(q)$ is the bare TO-phonon polariton frequency. This is the case in both LP and UP branches, where the co- and counter-propagating polariton states are brought into resonance.

The phase difference can only affect transitions, and therefore a reflectivity peak, that has both cubic and quartic anharmonic components. The cubic anharmonicities contributes to all the Bragg signals ($n = -1$, $n = -2$, and so on) found in the total Bragg reflectivity of Figure. 3.2. The quartic anharmonicity contributes to only the even number transition. As a result only the even n peaks of each panel are directly effected by the phase difference.

In the LP branch in Figure. 3.2(a) it is clear that the $n = -1$ peak is almost indifferent to the phase. The transition that causes this peak has only two contributions. The $n = -2$ peak from the same panel and in the same branch, clearly demonstrates a decrease in height by roughly a factor of a half for $\phi = \pi/2$. The transitions that occur to form this peak include a two-phonon transition from the fourth order process and two one-phonon transition from the third order process. The former is the stronger component, the latter is a second order multi-phonon transition. The combination of the two allow for the interference effects that are seen by the green and black lines in Figure. 3.2.

When close to the lower Restrahlen band edge, which occurs at $\nu = \omega/2\pi \sim 8$ THz, the acoustically induced peak in the reflectivity fails to conform to the expectation of identical peaks for both phases. This is most clearly seen in Figure 3.2 (d) and (e). In the LP branch as the frequency increases in Figure 3.2 (b) to (e), the phase causes more pronounced changes in reflectivity. This is shown by the increasing differences between the dashed green and solid black lines. As previously discussed (see section 2.2), the flattening out of the LP branch of the bare TO-phonon polariton dispersion causes the transition to accumulate below the restrahlen band, causing

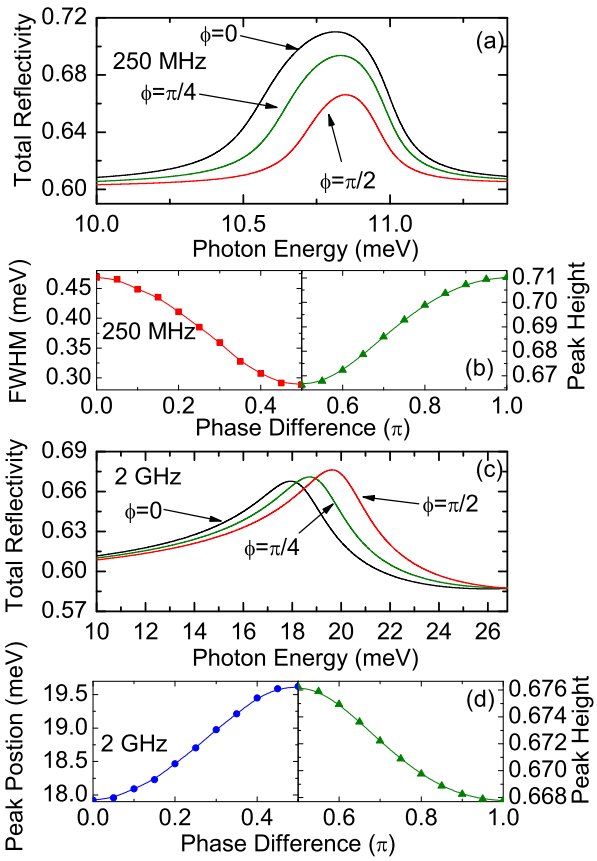

Figure 3.3: (a) The total Bragg reflectivity of the $n = -2$ Bragg signal in LP branch calculated for $\nu_{ac} = 250$ MHz and phase differences $\phi = 0$, $\pi/4$, and $\pi/2$. The variation of the full linewidth taken at half the peak maximum (FWHM) of the peak shown in (a) is given by the red squares in (b) and the peak height is given by the green triangles in (b). The cumulative cusp-like peak in the reflectivity spectrum, calculated for $\nu_{ac} = 2$ GHz, is shown in (c). The variation of the peak position is shown by blue circles and the peak height in green triangles of the peak in (c).

overlap between the acoustically induced band gaps. Therefore, at an acoustic frequency $\nu_{ac} = \Omega/2\pi \sim 2$ GHz the peak is due to multi-phonon transitions and it is no longer possible to separate the odd transitions from the even. Thus, the peaks becoming increasingly of a multi-phonon nature as the detuning decreases, leading to interference effects.

The UP branch also demonstrates some unusual behavior close to the restrahlen band. Unlike the LP branch the shape of the UP branch dispersion is not so conducive to the accumulation effect (see Figure 2.1). In this case multi-phonon process have little influence on the lowest energy peak in the UP reflectivity. However, there is still clearly a discrepancy for the two phases for small detuning even for the $n = -1$ peak. The discrepancy in this case is caused by virtual higher order transitions. These occur close to the restrahlen band because of the increased coupling strength due to the larger TO-phonon component of the polariton. In Figure 3.2(a) the $n = -3$ peak shows the expected similarity between the two different extremes of phase.

The effect that the phase difference has on the acoustically induced peaks is quantified in Figure 3.3. Figure 3.3 (a) clearly shows a very large difference in the efficiency of the

$n = -2$ peak for $\nu_{\text{ac}} = 250$ MHz. The peak position is almost completely unaffected by the phase because it is solely determined by the Bragg condition for this spectral range. Figure 3.3 (b) shows that the peak height is decreased by a factor of two and the FWHM falls by a third. This in line with the expectation of the destructive interference of the two anharmonic scattering channels.

The multi-phonon transition reflectivity peak shown in Figure 3.3 (c) behaves quite differently to the $n = -2$ transition investigated in Figure 3.3 (a) and (b). The peak shows minimal alteration in peak width and height. The small increase in the high of the multi-phonon peak is due to increase in the bare polariton reflectivity in this range. The peak position is shown to vary smoothly but drastically with phase, increasing as the interference becomes more destructive. In this case the accumulation effect near the lower Restrahlen band edge means the peak position is no longer dependent on the Bragg condition. As a result the peak position is effected solely by the interference effects.

A comparison of the phase difference for two different acoustic intensities is given in Figure 3.4. The black lines shows the total Bragg reflectivity $R = \sum_n |r_n|^2$ for $\phi = 0$ and the green line shows R for $\phi = \pi/2$. The red lines show the bare TO-phonon polariton reflectivity spectrum $R^{(0)}$, which has been calculated for $I_{ac} = 0$. The highlighted region is the area of the spectrum that is displayed in the inset to each panel. It shows the $n = -2$ transition in more detail, to illustrate the effect that the phase has on the even transitions.

In both Figure 3.4 (a) and (b) the phase difference of $\phi = \pi/2$ causes the destructive interference of the $n = -2$ peak, shown by the green line. As one would expect the destructive interference at the even order resonances, away from the restrahlen band, is nearly independent of the acoustic intensity. The slight difference that occurs for $I_{\text{ac}} = 25\text{kWcm}^{-2}$ is due to higher order effects. In the insets of both Figure 3.4 (a) and (b) the full destructive interference reduces the height of the reflectivity by roughly half. This is repeated in the UP branch where the acoustically induced peaks, while different between the two acoustic intensities, are reduced by half in both cases.

In the LP branch the peak at roughly 6 THz is caused by the acoustically induced quasi-continuum, which results from the accumulation of states near the lower restrahlen band edge. The effect this has is to reduce the reflectivity in the region just below the restrahlen band, immediately below $\omega/2\pi \sim 8$THz. This can be seen in both Figure 3.4 (a) and (b). The propagating TO-phonon states, which are part of

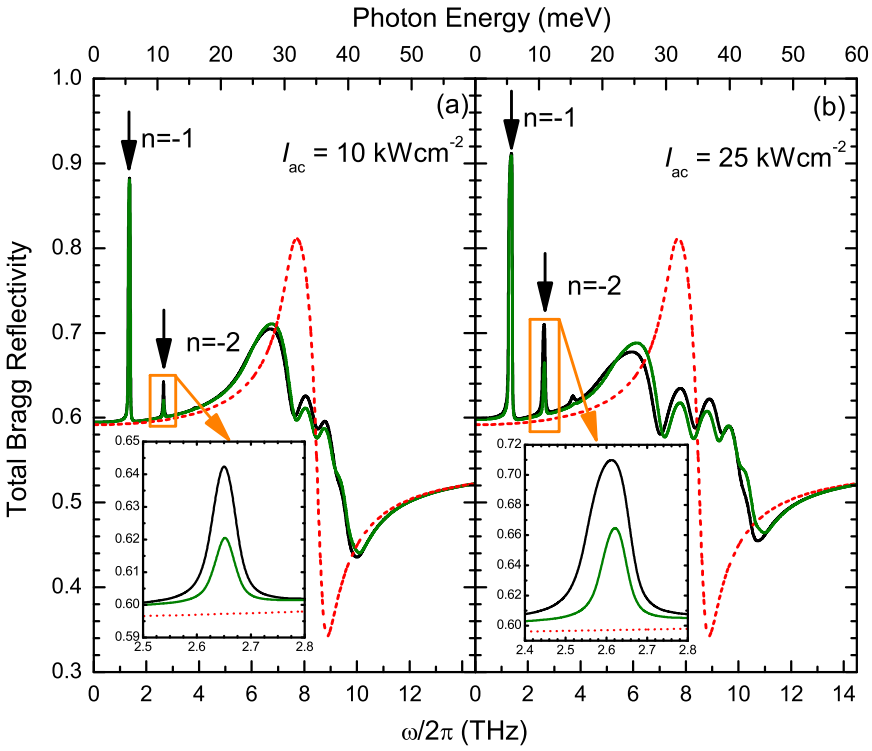

Figure 3.4: This shows the reflectivity of $LiNbO_3$ undergoing the RAO effect for $I_{ac} = 10\ \mathrm{kWcm}^{-2}$ and $25\ \mathrm{kWcm}^{-2}$ with $\nu_{ac} = 250$ MHz AW and for the chief values $\phi = 0$ and $\phi = \pi/2$ of the phase difference. The black line shows the Total Bragg reflectivity for $LiNbO_3$ for $\phi = 0$ and the green line for $\phi = \pi/2$. The dashed red line shows the total Bragg reflectivity when only the bare polariton is considered.

the acoustically induced quasi-continuum, cause this reduction. Increasing the acoustic intensity will then increase the width of the quasi-continuum, which reduces the reflectivity. Conversely, the full destructive value of ϕ, which reduces the effective coupling between the AW and TO-phonon, will reduce the width of the quasi-continuum. This will actually increase the reflectivity close to the restrahlen band.

3.4 Device Applications

Recently, THz radiation has become an important field of study due to the varied array of physics and chemistry that occurs in this spectral band [44]. Investigations that have made use of this spectral range include studies of picosecond phonon dynamics, polariton propagation and the optical properties of various materials [45–48]. There are also applications for THz radiation in fields as diverse as sub-mm wave

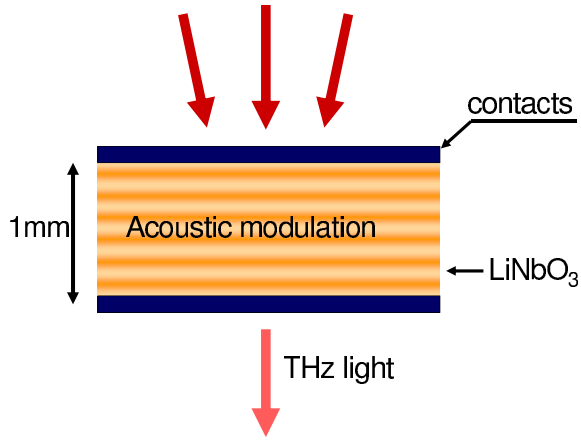

Figure 3.5: A schematic showing a possible design for a tunable THz filter, achieved using the RAO effect in $LiNbO_3$.

astronomy, chemical recognition, biomedical imaging, THz imaging and sensing for security applications [49–51].

As a result of the variety of use in which THz radiation can be employed, spectrally resolved control has become an important research topic. There are several examples of attempts at spectral control of THz radiation in the literature. One example is the optical control of carrier densities in type-I/type-II GaAs/AlAs multiple quantum wells at cryogenic temperatures [52]. Other examples include magnetically tuned liquid crystals in metallic hole arrays and Lyot and Sloc filters, shown to be tunable over various range between 0.1 and 0.8 THz [53–55]. A further example includes the relative lateral translation of two metallic photonic crystals to produce a THz filter, tunable in the range 0.365 to 0.385 THz [56].

This section discusses the use of $LiNbO_3$, undergoing the RAO effect, as a tunable THz filter. This filter would be tunable over a range of up to 4 THz, an improvement of an order of magnitude over previous designs. Figure 3.5 gives an example of the type of device proposed. A slab of $LiNbO_3$ undergoing the RAO effect is shown by the alternating bands of orange and yellow and is up to a 1 mm thick. Two thin contact layers of doped semiconductor produced the ultrasonic resonator necessary to achieve the required acoustic intensity.

In the previous section, Figure 3.2 demonstrates that the frequency of the bulk acoustic wave makes for an easily accessible parameter to tune the reflectivity spectrum of $LiNbO_3$. The transmission through the $LiNbO_3$ slab, which is undergoing the RAO effect, is quantified by the extinction given in Figure 3.7. The extinction is defined as

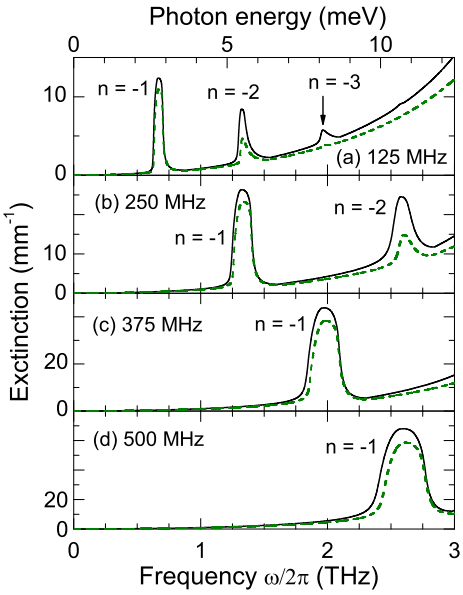

Figure 3.6: Extinction of the electric field at different acoustic frequencies, for $\phi = 0$ (black solid lines) and $\phi = \pi/2$ (green dashed lines), for $I_{ac} = 25$ kWcm^{-2}.

the inverse of the decay length $\ell(\omega)$, which is itself defined as $E(\ell, \omega) \equiv E(z = 0, \omega)/e$. Figure 3.6 shows the extinction up to ~ 3 THz, for the two extremes of interference at $\phi = 0$ and $\phi = \pi/2$.

The extinction, like the reflectivity, is clearly controlled by the acoustic frequency, the acoustically induced band gaps result in regions of high extinction. The large contrast between the background and the peaks in the extinction spectrum shown in Figure 3.6, coupled with a tunability between 0.5 and 3 THz, is a marked improvement on the other methods discussed previously. It is these factors that suggest that the RAO effect in $LiNbO_3$ would produce an effective filter.

In the schematic presented in Figure 3.5 GaAs contacts are used to compress and rarefy the bulk $LiNbO_3$. By passing an AC current through the films, the repulsion and attraction of each will induce bulk oscillation in the $LiNbO_3$. An estimate of the parameters required for the narrow doped GaAs contacts, can be made by using a pure Drude model to calculate the thickness and electron density n_e. The Drude dielectric function is given by [57]

$$\varepsilon(\omega) = \varepsilon_\infty - \frac{\omega_p^2}{\omega^2 + i\omega\gamma},$$

where ε_∞ is the high frequency dielectric constant and γ is the plasmon damping

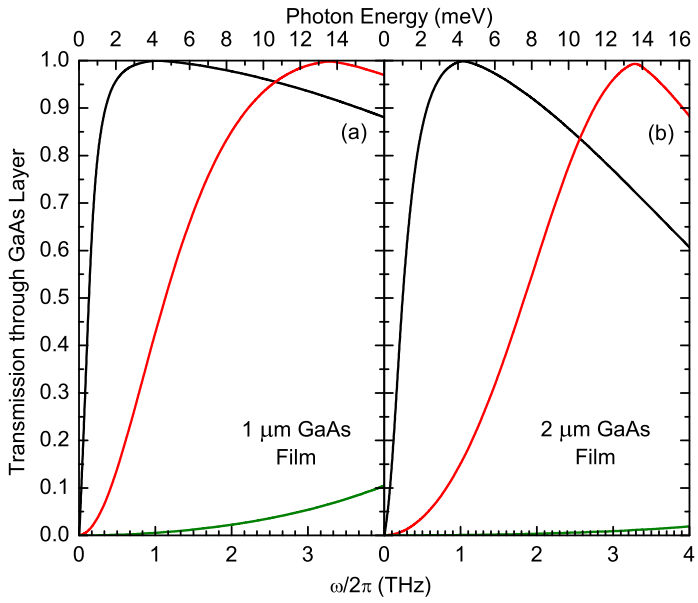

Figure 3.7: Transmission calculated using a Drude model, that is no phonon broadening is considered, for doped GaAs film of (a) 1 μm and (b) 2 μm thickness. The black line is for an electron concentration of $n_e = 10^{14}$ cm^{-3}, the red line for $n_e = 10^{15}$ cm^{-3} and the green line $n_e = 10^{16}$ cm^{-3}.

constant. The plasma frequency ω_p is given by

$$\omega_p = \sqrt{\frac{4\pi n_e e^2}{m^*}},$$

where m^* is the electron effective mass and e the electronic charge.

To calculate the transmission data shown in Figure 3.7 the scattering matrix method was used. This is a modification of the transfer matrix method for improved stability over multi-layered structures. A full description of this method can be found in the next chapter, where it has been used to calculate the optical response of a metal undergoing the acousto-plasmonic effect.

In Figure 3.7 the transmission of GaAs is shown, where the GaAs film is doped for an electron concentration of $n_e = 10^{14}$ cm^{-3} (black solid line), for $n_e = 10^{15}$ cm^{-3} (red solid line) and for $n_e = 10^{16}$ cm^{-3} (green solid line) over the range of operation of the device. The graph shows that a reduced damping constant and thinner layer improves the transmission in the range of values at which the filter could operate. It clearly indicates a large enough transmission through the GaAs layer for a transmission mode filter.

3.5 SUMMARY

The chapter has investigated, using numerical calculation, the TO-phonon RAO effect for two anharmonic terms in the interatomic potential. The system used to investigate this was semi-infinite $LiNbO_3$. The reason for choosing $LiNbO_3$ is that it is both ionic and displays a large cubic and quartic anharmonicity. The ionic nature of the material allows for the formation of the necessary TO-phonon polaritons. The large anharmonicity ensures that the fourth order term in the interatomic potential is sufficiently large enough to be treated on an equal footing with the third order term, that is non-perturbatively.

Initially, an estimate of the coupling constant between the TO-phonon and the AW was provided. It was found that there was a difference between the amplitudes of the coupling terms $\sigma_{3,4}$ of roughly an order of magnitude. Despite this, further investigation showed that the fourth order coupling constant was still of sufficient strength to have a noticeable impact on the reflectivity of $LiNbO_3$.

The phase difference between the two anharmonic terms in Eq. (3.19) has become an important material parameter. This is due to the relative strengths of the two anharmonic terms. It was shown in this chapter that for $\phi = \pi/2$ the maximum destructive interference occurs. This was due to the fourth order acoustic term in Eq. (3.19) having twice the frequency of the third order term. It was also shown that ϕ altered the total Bragg reflectivity in a slightly different manner close the TO-phonon polariton restrahlen band. This was due to the quasi-continuum close to the lower edge of the restrahlen band.

The tunability of the total Bragg reflectivity spectrum, caused by the RAO effect, is the basis for a proposed tunable THz filter over a wide spectral range. This chapter included an investigation of such a filter, one that sandwiches bulk $LiNbO_3$ between two doped GaAs films. The GaAs films proved the compressions and rarefactions that form the AW, which modifies the TO-phonon polariton dispersion. In turn this cause the tunable spikes that are the basis of the THz filter in a transmission mode.

4 Acousto-Plasmonics

One of the characteristics of metals is the high concentration of conduction electrons, which are responsible for most of their thermal and optical properties. Under certain circumstances the plasma oscillations of the free electrons can couple to light, this forms plasmon polaritons. This chapter examines the effect that a surface acoustic wave (SAW) has on a thin Au foil. The acoustical excitation of the surface plasmon polariton (SPP) leads to dramatic changes in the optical properties of the foil.

4.1 Theoretical Background

This section discusses the method of calculation used to produce the numerical results. It based on the scattering matrix method of Tikhodeev et. al. [58]. The method was extended to include the possibility of a propagating sinusoidal corrugation at each interface.

4.1.1 Theoretical Model

The acousto-plasmonic effect can be investigated by starting with Maxwell's curl equations. Approximating the permeability as $\mu = 1$, the equations can be written

as

$$\frac{1}{c}\frac{\partial \mathbf{H}}{\partial t} = \nabla \times \mathbf{E}, \tag{4.1a}$$

$$-\frac{1}{c}\frac{\partial \mathbf{D}}{\partial t} = \nabla \times \mathbf{H}. \tag{4.1b}$$

The magnetic field strength is given by $\mathbf{H}$, the electric field strength by $\mathbf{E}$ and the dielectric displacement by $\mathbf{D} = \varepsilon\mathbf{E}$. To access the surface plasmons polariton (SPP) some conditions must be met. The first of these requirements is that the electric field must have a component normal to the interface. This is fulfilled only by p-polarised light, where the magnetic field is given by

$$\mathbf{H} = \begin{pmatrix} 0 \\ H_y(x,z,t) \\ 0 \end{pmatrix},$$

and the electric field by

$$\mathbf{E} = \begin{pmatrix} E_x(x,z,t) \\ 0 \\ E_z(x,z,t) \end{pmatrix}.$$

There can be no s-polarised surface waves which couple to the surface plasmon [13].

In general, no SPP can be excited in a simple metal foil by light, the dispersion of the SPP falls outside the light cone. To couple light to the plasmon requires that, for a given photon energy $\hbar\omega$, the SPP dispersion must be shifted inside the light cone. This is the second condition required for light to excite SPPs. There are two methods to achieve this. To excite SPPs by incident light the attenuated total reflection (ATR) method is to pass the incident light through a dielectric medium with a wider light cone than the vacuum. This allows direct excitation of the V/M SPP. As the ATR method is not used in this thesis, no further mention will be made of it. The other method is to directly provide the required Δk by inducing some surface roughness, such as a diffraction grating, to shift the wavevector of the incident light by Δk.

The geometry of the system under study is shown in Figure 4.1. The upper interface shows the boundary between the Au foil and vacuum, this is the surface on which the light is incident. In the z direction the light has a wavevector q_0 and along the x axis a wavevector of k. The foil is of thickness d and shares a lower boundary with a

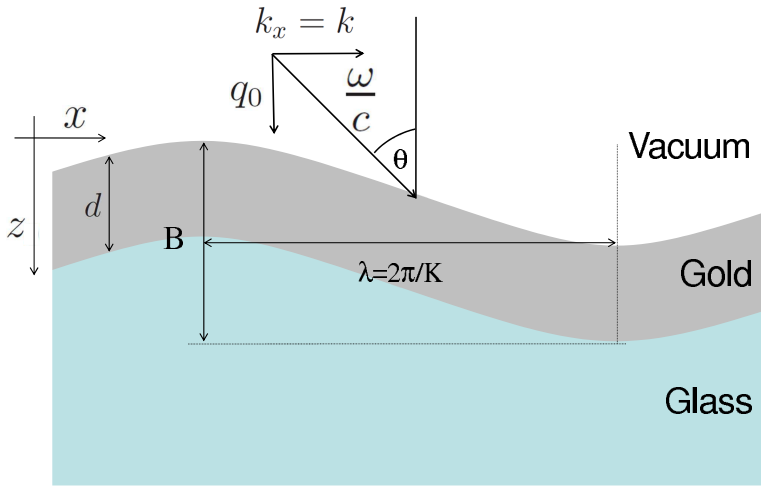

Figure 4.1: The geometry of the RAO effect in a thin Au films studied in this chapter. The light wavevector symbols are defined by the arrows labeled q_0 and k. The SAW wavevector is labeled by K. The amplitude of the SAW modulation is B and d is the thickness of the Au foil. The light is incident on the foil at an angel θ.

glass substrate, which has a dielectric constant of $\varepsilon_g = 2.28$. The foil is acoustically modulated by a SAW. The interfaces of the foil the foil can be described by

$$z_0(x,t) = B\cos(Kx - \Omega t), \tag{4.2a}$$

$$z_1(x,t) = z_0(x,t) + d, \tag{4.2b}$$

where the SAW wavevector is K and its transverse amplitude B.

The grating method of light excitation of SPPs involves the direct addition of the required increase in wavevector Δk for a given ω value. The grating allows the in plane wavevector of the incident light to take the values

$$k = \frac{\omega}{c}\sin(\theta) + n\,\Delta k,$$

where n is an integer and Δk the wavevector shift induced by the grating. The extra momentum provide by the grating allows the incident light to excite the V/M SPP [31]. In this chapter a similar process occurs where the grating is provided by a SAW propagating in the positive x-direction. This causes the appearance of n Bragg replicas and results in $\Delta k = K$. This is schematically shown by the orange arrows in Figure 4.2. Strictly, the use of a propagating SAW as the grating means that

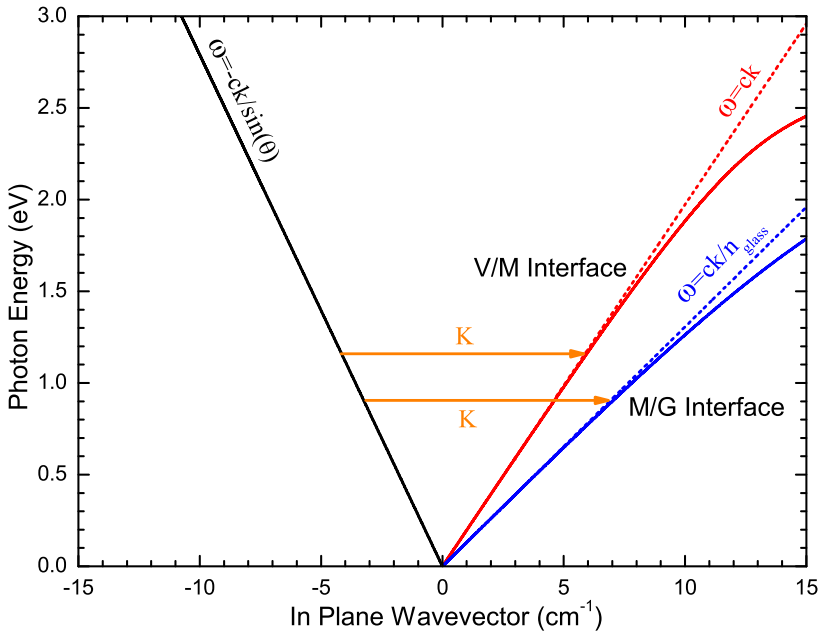

Figure 4.2: The red and blue lines are the bare SPP dispersion at the V/M and M/G interface, respectively. The dashed red and blue lines are the light dispersions in vacuum and glass at normal incidence, respectively. The dispersion of light in the vacuum is shown by the solid black line at $\theta = 45^o$. The arrows indicate the SAW coupling for an acoustic wavevector K.

the photon energy is also altered by $n\Omega$, giving each the dispersion curve of each Bragg replica a slight frequency offset. However, while the plasmon energy in Au is $\hbar\omega_p = 9.03$ eV the energy of a SAW phonon is $\hbar\Omega < 8 \times 10^{-6}$ eV. The value of n required to make this offset more than negligible is several orders of magnitude larger than the $n = 5$ that is necessary for the parameters used in this chapter.

Using a SAW to induce a dynamical superlattice in the plane of the Au foil results in a folded dispersion, which is sketched in Figure 4.3. The blue lines show the SAW induced folded dispersion of the SPP on the glass side of the Au foil and the black lines show a similar dispersion for the vacuum side. The orange dashed lines show the light cone for various angles of incidence and the red dashed lines the first SAW induced Brillouin zone boundary. Like the TO-phonon polariton RAO effect discussed in earlier chapters the crossing points are where the SAW induced band gaps would form. In Figure 4.3 these gaps are not shown, the dispersion here is simply the translation of the bare dispersion by up to $n_r = 2$ Bragg replicas.

The SAW induced SPP band gaps are regions in the spectrum where no propagating SPP states occur. In contrast to the TO-phonon RAO effect, this reduces the reflectivity around these band gaps. At these points in the dispersion no propagating SPP

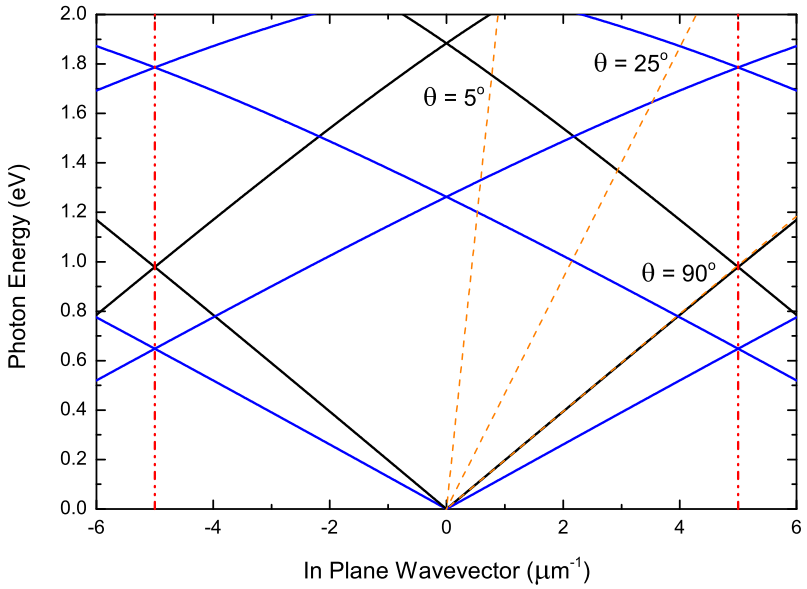

Figure 4.3: A schematic of the folded SPP dispersion for the SAW modulated Au foil, where $K = 10\,\mu\text{m}^{-1}$ and $n_r = 2$. The solid black lines are the dispersion of the SPPs at the VM interface and the solid blue lines are for SPPs at the MG interface. The dashed orange lines are the light cones for light incident at $\theta = 5^{\text{o}}$, 25^{o} and the limit of 90^{o}. The red dashed line is the position of the SAW induced Brillouin zone edge.

states occur reducing the reflectivity and leading to absorption in the metal. The angle of incidence of the light decides which of the crossing points are to be excite. With normal incidence only the crossing points near the center of SAW induced Brillouin zone are within the light cone. As the angle of incidence increases the widening light cone allows a wider range of points in the dispersion to be accessed.

The electric and magnetic fields that are used to model this system take the form

$$H_y(x,z,t) = \sum_n [H_y^+ e^{i\kappa_n z} + H_y^- e^{-i\kappa_n z}] e^{ikx+i\omega t} e^{i(Kx-\Omega t)n},$$
$$E_x(x,z,t) = \sum_n [E_x^+ e^{i\kappa_n z} + E_x^- e^{-i\kappa_n z}] e^{ikx+i\omega t} e^{i(Kx-\Omega t)n},$$
$$E_z(x,z,t) = \sum_n [E_z^+ e^{i\kappa_n z} + E_z^- e^{-i\kappa_n z}] e^{ikx+i\omega t} e^{i(Kx-\Omega t)n},$$

where κ_n is the wavevector of light in a given material along the z-axis (vacuum, metal or glass). Along the z-direction the dispersion takes the same form for each material in the system. The derivation is presented in section B.1 of the appendices.

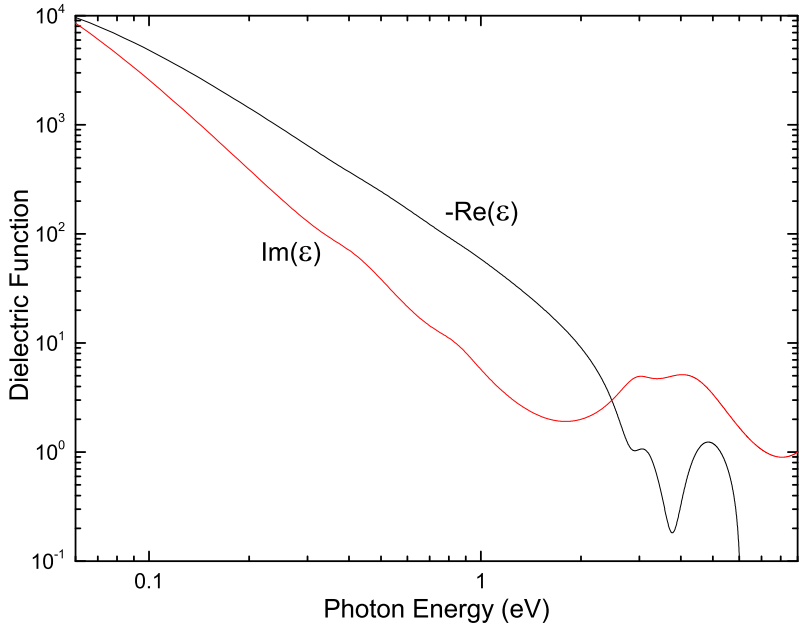

Figure 4.4: The real and imaginary parts of the dielectric function of Au calculated using the Lorentz-Drude model. The real part of the dielectric function has been multiplied by -1.

The form of the dispersion is given by

$$\kappa_n = \sqrt{\frac{\varepsilon}{c^2}(\omega + n\Omega)^2 - (k + nK)^2} \tag{4.3}$$

where $\varepsilon = 1$, ε_M or ε_G depending on the material in which the dispersion is calculated. The dispersion in metal is given by ε_M, the dispersion in glass by ε_G.

4.1.2 Dielectric Function

The model used for the complex dielectric function was calculated by Rakić et al [59] and is a Lorentz-Drude oscillator model. More information on this can be found in Appendix C. In the case of the Lorentz-Drude model the free electron part of the dielectric function is given by the Drude model and the bound electron part by the Lorentz oscillator model. The full function is

$$\varepsilon_m = 1 - \frac{f_0\omega_p^2}{\omega(\omega - i\Gamma_0)} + \sum_{j=1}^{l} \frac{f_j\omega_p^2}{(\omega_j^2 - \omega^2) + i\omega\Gamma_j}, \tag{4.4}$$

where Γ_0 is the reciprocal of the time between collisions and ω_p is the plasma frequency. The summation is over l different oscillators of the strength f_j, frequency ω_j with a damping constant of Γ_j. The values of these parameters are given in Table C.1 of Appendix C. The dielectric function is shown in Figure 4.4, the real part has a factor of -1 include so it can be shown on a logarithmic scale.

The Drude component of dielectric function is given by the first two terms of Eq. (4.4). The Drude model is a classical model that assumes the electrons are in constant motion and undergo collisions only with the immobile ions of the crystal lattice [60]. The final term in Eq. (4.4) is the Lorentz component of the model and gives the contribution to the dielectric behaviour of the material from the bound electrons. The Lorentz oscillator model takes account of the interband transitions of the bound electrons in the metal. The dielectric function can be split into these two components because each component dominates a separate spectral range. At low frequencies the Drude component dominates and at high frequencies the Lorentz components dominate [61, 62].

4.2 Scattering Matrix Method

Conventionally, the calculation of the optical properties of an arbitrary layered system is performed using the transfer matrix method. The transfer matrix formalism is a method for calculating partial wave amplitudes across a layered system. The transfer matrix formalism separates the amplitude of the electric field into a z-dependent part and a part that depends only on the material properties. An interface transfer matrix $\mathbb{T}_{a,b}$ will then be used to connect a vector $\mathbb{A}(z)$ of z-dependent parts, the elements of the vector are partial wave amplitudes $\mathcal{A}_j^{\pm}(z)$, across an interface. This interface matrix is essentially a statement of the boundary conditions across the boundary in question.

In the transfer matrix formalism $\mathcal{A}_j^{\pm}(z)$ are split into vectors according to which side of the layer they are on. This is schematically represented in Figure 4.5 (a), where the amplitudes of matching colour are grouped into vectors $\mathbb{A}_v$ on the vacuum side and $\mathbb{A}_s$ on the substrate side. It is because $\mathcal{A}_j^{\pm}(z)$ are organised into vectors in this way that the transfer matrix, which propagates the partial waves across a layer, takes

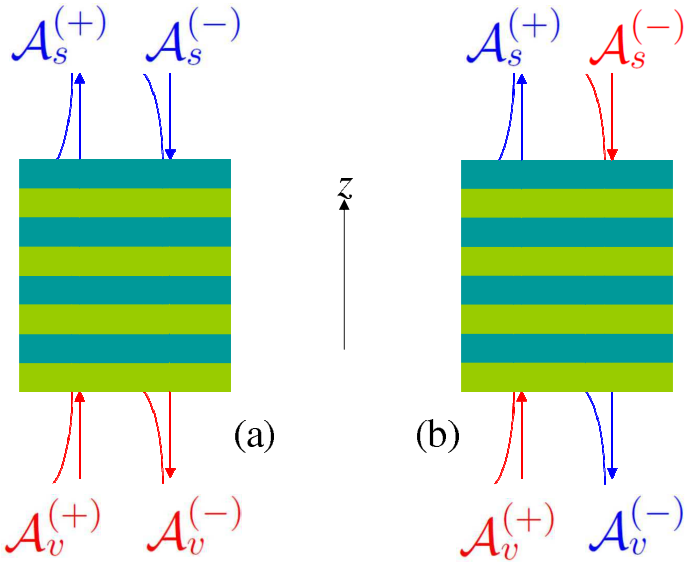

Figure 4.5: A diagram that defines the conceptual differences between the (a) the transfer matrix and (b) the scattering matrix formalisms. The positive z-direction is defined as running from bottom to top and the partial wave amplitudes in the vacuum are $\mathcal{A}_v^{\pm}$ and in the substrate $\mathcal{A}_s^{\pm}$, where the superscript indicates direction propagation. The colours indicate how the amplitudes are group into vectors. In (b) we can see that at the interface the each vector will contain elements of similar magnitude because waves are grouped according to direction of propagation.

the form

$$\mathbb{T}_L = \begin{pmatrix} e^{i\mathcal{K}d} & 0 \\ 0 & e^{-i\mathcal{K}d} \end{pmatrix}. \tag{4.5}$$

The existence of evanescent solutions can make the element $\mathbb{T}_L(2,2)$ exponentially large. For a layered system $\mathbb{A}_s$ can be calculated using

$$\mathbb{A}_s = \mathbb{T}\mathbb{A}_v,$$

where $\mathbb{T}$ is the product of all transfer matrices. This means that for higher values of d or a great number of layers this can be a problem for numerical calculations. However, it is still necessary to use the transfer matrices for each layer of the system to calculate the scattering matrix. The transfer matrices at the V/M boundary of the system described in Figure. 4.1 are given by

$$\mathbb{T}_{V/M} = \mathbb{V}^{-1}\mathbb{M}, \tag{4.6}$$

and at the M/G boundary

$$\mathbb{T}_{M/G} = \mathbb{M}^{-1}\mathbb{G}, \tag{4.7}$$

where $\mathbb{V}$, $\mathbb{M}$ and $\mathbb{G}$ are square matrices of dimension $2(2n_r + 1)$. These matrices contain the Bessel functions of the first kind that described the modulated interfaces. The full transfer matrix of the system is given by

$$\mathbb{T}_{total} = \mathbb{T}_{V/M} \begin{pmatrix} \mathcal{E}^+ & 0 \\ 0 & \mathcal{E}^- \end{pmatrix} \mathbb{T}_{M/G}, \tag{4.8}$$

where $\mathcal{E}^- = \delta_{n,m}\exp(-ip_n d)$ and $\mathcal{E}^+ = \delta_{n,m}\exp(ip_n d)$. A full derivation is provided in Appendix B.

The geometry studied in this chapter has only two interfaces, one between the vacuum and the metal and another between the metal and glass. While the amplitude of the corrugation relative to the metal layer thickness is not great enough to require more than two interfaces it could become so. The thickness d could also become too thick for a reliable calculation to be made by the transfer matrix method. To deal with this case a modification of the transfer matrix method is required. The scattering matrix formalism, developed for problems such as this by Tikhodeev et al from similar methods for electron tunnelling in hetrostructures [58, 63], solves some of the problems associated with partial amplitudes calculated by the transfer matrix method. The possibility of further research makes it prudent to use a method that would withstand as wide a range of parameters as possible. For example, using the scattering matrix method, the optical properties of a system with an arbitrary number of layers can be investigated.

The scattering matrix avoids the problems associated with the transfer matrix by organising $\mathcal{A}_j^{\pm}$ in to vectors in a different way. A schematic example of this can be found in Figure 4.5 (b), where $\mathcal{A}_{v,s}^{(\pm)}$ are the grouped according to similar colour in the vectors $\mathbb{B}_{\text{in,out}}$. Red shows the partial amplitudes of the input vector

$$\mathbb{B}_{\text{in}} = \begin{pmatrix} \mathcal{A}_v^+ \\ \mathcal{A}_s^- \end{pmatrix}, \tag{4.9}$$

and blue shows the partial amplitudes of the output vector,

$$\mathbb{B}_{\text{out}} = \begin{pmatrix} \mathcal{A}_s^+ \\ \mathcal{A}_v^- \end{pmatrix}. \tag{4.10}$$

These vectors are coupled by the total scattering matrix

$$\mathbb{B}_{\text{out}} = \mathbb{S}_{\text{v,s}} \mathbb{B}_{\text{in}}. \tag{4.11}$$

The optical properties of the system under question can then be calculated from the elements of Eq. (4.10),

$$T_n = |\mathcal{A}_s^+|^2, \tag{4.12a}$$

$$R_n = |\mathcal{A}_v^-|^2. \tag{4.12b}$$

The main disadvantages of the scattering matrix compared to the transfer matrix is the slightly increased difficulty in calculating it. The method of deriving the scattering matrix is given in the Appendix B

For the problem of acousto-plasmonics, as with the TO-phonon RAO effect of the previous two chapters, the number of Bragg replicas generated has to be truncated for the problem to be tractable. As in the previous chapters the number of Bragg replicas used is $-n_r \leq n \leq n_r$. Each amplitude $\mathcal{A}_j^{\pm}$ is actually a vector of dimension $N = 2n_r + 1$. The use of a calligraphic font will, henceforth, indicate either a vector of the same dimension or a matrix of $N \times N$ dimensions. The vectors $\mathbb{B}_{\text{in,out}}$ and $\mathbb{A}_{\text{v,s}}$ are constructed of the partial amplitude vectors and have the dimensions $2N$. Henceforth, this bold font will only be used for vectors of this dimension or matrices of dimension $2N \times 2N$.

4.3 Reflectivity of SAW Modulated Thin Au Foil

This section will show the effect that the SAW has on the reflectivity of the central Bragg replica. It will also demonstrate the effect that varying each of the four parameters of the system has on the central Bragg reflectivity of the Au film. The section demonstrates the tunability of resonant plasmonic state and the effect it has on the central Bragg reflectivity of the system.

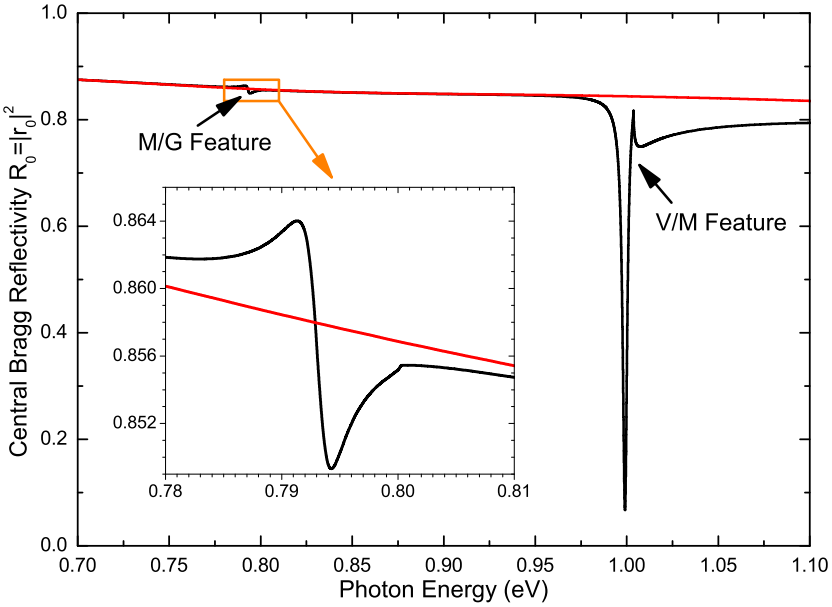

Figure 4.6: A figure to show the effect the acoustic excitation has on the central Bragg reflectivity of an Au foil where $d = 0.04$ μm, $B = 0.01$ μm, $K = 10$ μm^{-1} and $\theta = 75^{o}$. The small feature highlighted by the orange box is due to the acoustic excitation of the SPPs at the M/G interface. The large peak at $\omega \sim 1$ eV is due to the acoustic excitation of the SPPs at the interface between the vacuum and the Au foil.

4.3.1 Acoustic Modification of the Bare Plasmon Polariton Reflectivity

The bare, acoustically unexcited plasmon reflectivity is drastically modified by SAW excitation. The SAW generates a corrugation in the surface of the Au foil. This periodicity provides the extra momentum to the incident light necessary to couple it to the SPPs. In the case presented in this chapter it is assumed that the foil thickness is much smaller than the z-direction decay of the SAW induced corrugation. Thus, coupling between the SPPs and light can occur at both interfaces.

In Figure 4.6 the bare reflectivity is shown by the red line and the black line shows the the effect the SAW has. The SAW-modified reflectivity spectrum shows two features. The highest frequency feature is caused by the V/M interface SPP and the lowest by the M/G SPP. In both cases the light couples to the SPP at the values at which the acoustic wave is resonant with SPP dispersion, as shown in Fig 4.2 by the orange arrows, and Figure 4.3 by the crossing points.

The two features that are present in Figure 4.6 correspond to SAW induced band gaps

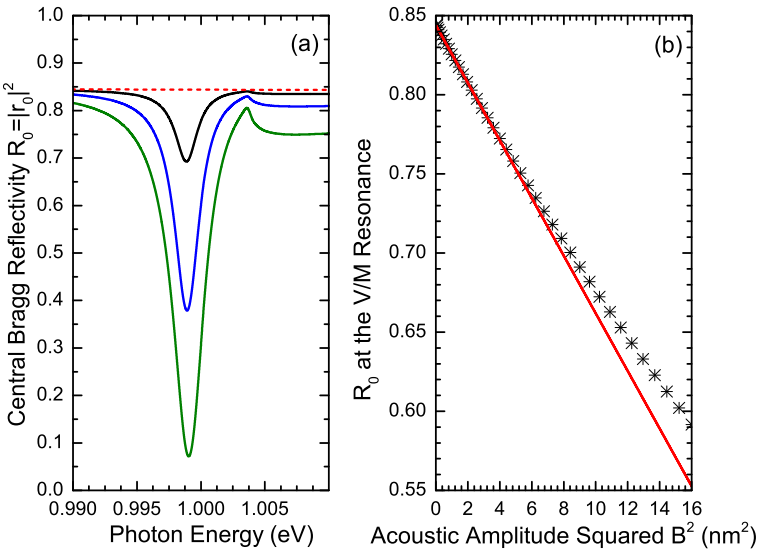

Figure 4.7: A graph showing how the variation of the corrugation amplitude alters the central Bragg reflectivity on an Au foil of $d = 40$ nm. (a) shows the central Bragg reflectivity at the SPP resonance on the V/M interface for $B = 3$ nm, 6 nm and 10 nm with $K = 10\mu\text{m}^{-1}$ and $\theta = 75^o$. The dashed red line shows the reflectivity for $B = 0$. (b) shows the variation the dip depth with the square of the acoustic amplitude for the same values of d, K and ϕ as (a). The red line is a linear fit of the first 17 data points and highlights the nonlinear nature of the resonance strength above $B \sim 2$ nm.

at each face of the foil. The large feature is due to a band gap at the V/M interface. The weaker feature is due to a band gap between the SPPs at each interface. In this case the foil is sufficiently thin enough to allow the band gap to form.

4.3.2 Corrugation Amplitude

The amplitude of the corrugation B of the Au foil is the main parameter by which the strength of the coupling between the light and surface plasmon can be controlled. The increased efficiency of diffraction of the incident light by the grating associated with larger B leads to larger splitting between the dispersion branches of the SPP. The increase in gap width leads to larger dips in the reflectivity.

In Figure 4.7 (a) the red dashed line shows the reflectivity of the Au film unexcited by a SAW. As the SPP dispersion falls outside the vacuum light cone no SPP are excited in this case. The use of the SAW clearly changes this. By inducing a dynamical

superlattice band gaps are induced, as shown in Figure 4.3. As the band gaps are regions where the SPPs cannot propagate the absorption occurs, leading to the dips in the reflectivity.

In Figure 4.7 (a) the black solid lines is for $B = 3$ nm, the red line for $B = 6$ nm and the green line for $B = 10$ nm. The increase in the corrugation amplitude makes the SPP coupling more efficient by diffracting a larger proportion of the light into the first Bragg replica to couple with SPPs. This is analogous to the the increase in I_{ac} in the TO-phonon RAO effect. The resultant band gap at the Brillouin zone edge is therefore larger. In this case the SPP under consideration is at the V/M boundary.

It is possible to use the depth of the reflectivity dip in the central Bragg replica to quantify the strength of the coupling and see the effect the corrugation amplitude has on it. In Figure 4.7 (b) the symbols show the value of the central Bragg replica at the SPP resonance plotted against the square of the corrugation amplitude B^2 in units of nm^2. As the coupling strength is proportional to the size the peak it varies quadratically with B up to $B \sim 2$ but higher order coupling becomes increasingly dominant beyond this point.

4.3.3 Angle of Incidence

The effect of varying the angle of incidence on the central Bragg reflectivity is to alter the resonant frequency of the coupling. The wavevector of the light parallel to the surface is one of the parameters that determines the value of the SPP resonant frequency. This is clearly seen in Figure 4.2. The light dispersion in black is given by $\omega = -ck/\sin(\theta)$. As the gradient changes with variation of θ, so will the value of ω at which the coupling occurs, indicated by the orange arrows.

The alteration of the SPP resonant frequency strongly effects the reflectivity of the central Bragg replica. This can be seen in Figure 4.8, where the dip position variation is due to the alteration of θ. The lowest frequency dip occurs at $\omega \sim 1$ eV and is for $\theta = 75^o$ and as the angle of incidence reduces the resonant frequency rises. As the angle of incidence rises the light cone narrows scanning through folded dispersion in Figure 4.3. At the highest angle of incidence the lowest lying energy gap in the spectrum occurs. Reducing the angle of incidence to normal, causes only the central SAW induced band gap to fall within the light cone which occurs at the highest

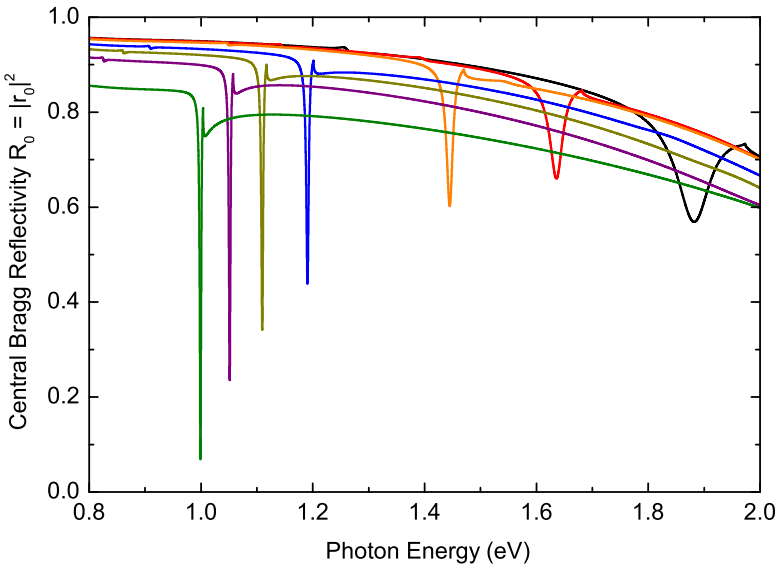

Figure 4.8: The central Bragg reflectivity is shown for the variation of the central Bragg reflectivity for various θ. The data was calculated for an Au film of thickness $d = 40$ nm, perturbed by a SAW of wavevector $K = 10\ \mu\text{m}^{-1}$ and $B = 10$ nm. Starting on the left the dips are due to $\theta = 75^o, 60^o, 50^o, 40^o, 20^o, 10^o$ and 0^o.

frequency. The dip widens and increases in depth as it moves to higher frequency. At $\omega \sim 1.65$ eV the dip is for $\theta = 10^o$ and the depth is at its minimum. However, this minimum is an artifact caused by the shape of the bare reflectivity spectrum.

The broadening of the central Bragg reflectivity peak as it is blue shifted is displayed in Figure 4.8. This is caused by the reduced detuning from the main surface plasmon resonance that occurs at $\omega \sim 3$ eV. This behaviour is analogous to the broaden that occured in the TO-phonon RAO effect mentioned in Chapters 2 and 3.

4.3.4 Foil Thickness

The properties of the SPP are dependent on the foil thickness and dielectric environment in which the foil is placed. In the geometry described in this chapter the foil shares each boundary with material of different dielectric constant. In these circumstances the foil is said to be supported because the dielectric medium on each side differs. It said to be unsupported when dielectric medium is the same on each side [64]. Whether the foil is supported or unsupported can alter the effect a variation of thickness has on the SPPs in a thin foil. As the example under consideration in

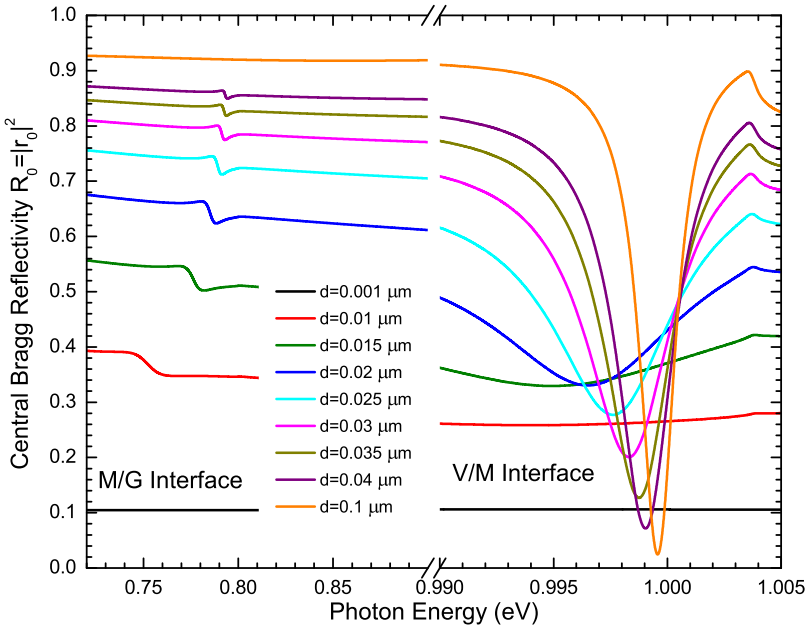

Figure 4.9: The reflectivity for light incident at $\theta = 75^o$ on an Au film of various thickness, perturbed by a SAW of $B = 10$ nm and $K = 10\mu m^{-1}$. The region to the left of the break on the horizontal axis shows the feature due to the interface between the metal foil and the glass substrate. The region to the right shows the large dip due to the SPPs at the vacuum metal interface.

this chapter is supported, this is the only case that will be considered.

In thick metal foils the plasmons at each boundary are independent. This is because the associated electric field decays rapidly into the metal. They do not interact and their resonant frequencies are determined in large part by the dielectric media the metal surface is in contact with. As the thickness of the material reduces the evanescent fields in the z-direction overlap. Thus, a transverse standing wave is established with both symmetric and anti-symmetric modes each with their own resonant frequency. The two excitations shown in Fig 4.9 show both reflectivity alterations caused the interaction of the evanescent fields associated with the SPPs at each surface.

Figure 4.9 shows that narrower foils reduce the size of the peak. The electric field amplitude of the SPP does not abruptly reach zero away from the surface of the metal, the skin depth is the distance over which the electric field decays away from the interface. As the thickness of the foil reduces the skin depth of the SPP in the metal becomes larger than the foil thickness. This decay is then continuous over the second boundary in the structure. The second boundary, within the range of the evanescent field of the SPP, is an extra source of scattering which leads to increased

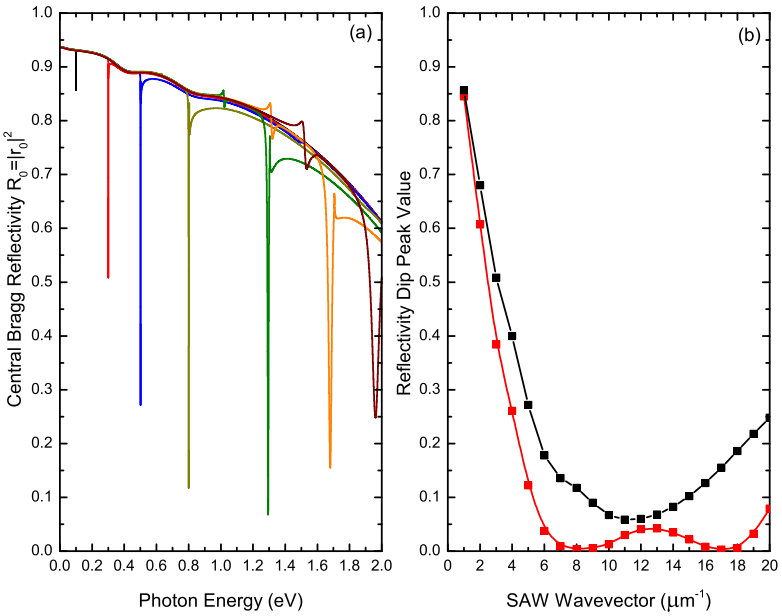

Figure 4.10: The reflectivity of light at angle of incidence $\theta = 75^{o}$ on an Au film, excited by a SAW induced corrugation of amplitude $B = 10$ nm of various wavevector K. (a) shows the central Bragg reflectivity for a foil of $d = 40$ nm selected values of K, from the left $K = 1\ \mu\text{m}^{-1}$, $3\ \mu\text{m}^{-1}$, $5\ \mu\text{m}^{-1}$, $8\ \mu\text{m}^{-1}$, $13\ \mu\text{m}^{-1}$, $17\ \mu\text{m}^{-1}$, $20\ \mu\text{m}^{-1}$. (b) shows the variation of the depth of the dip in the central Bragg reflectivity at the V/M SPP resonance, for K up to $20\ \mu\text{m}^{-1}$, where the black line is for $d = 40$ nm.

couple to the continuum states in the substrate. Thus, the thickness of the reflectivity dip is increased.

4.3.5 SAW Wavevector

The corrugation periodicity is set by the SAW wavevector K. The first order band gaps are found at the SAW induced Brillouin zone edges. The size of the Brillouin zone is set using this K and therefore setting the spectral position of the SPP resonances. This subsection examines the effect this has on the central Bragg reflectivity, for an Au foil of $d = 40$ nm with a SAW induced corrugation of $B = 10$ nm. The light is incident at an angle of 75^{o}.

In Figure 4.10 the central Bragg reflectivity is examined for a range of different SAW wavevectors. As expected, an increase in the wavevector blue shifts the dips in the reflectivity. This is shown in Figure 4.10 (a), where the increasingly blue shifted peaks are caused by successively large value of K. This is because the SAW induced

Brillouin zone becomes larger for greater K. At the edge of the Brillouin zone is the lowest order and strongest SAW induced band gap, these are the resonant points that cause the reflectivity dip.

The data shown in Figure 4.10 (b) by the black squares is the variation of the depth of the dip in the central Bragg reflectivity as a function of K for $d = 40$ nm. The decrease in central Bragg reflectivity at the SPP resonance steadily decreases up to a value of $K = 3\ \mu\text{m}^{-1}$. Beyond this value the dip depth variation with K levels off before increasing. This is due the spectral position of the dips associated with each data point in Figure 4.10 (b).

As shown in Figure 4.10 (a) increasing K blue shifts the resonant spectral position of the SPP, this reduces its detuning from a surface plasmon resonance, which leads to a reduction in the maximum reflectivity depth at the SPP resonance. By increasing K the crossing points in Figure 4.3 occur at increasing values of ω. At higher frequencies, i.e. in the non-retarded regime limit $k >> \omega s/c$, the crossing points approach the SPP Restrahlen band. At this point in the spectrum the larger surface plasmon component of the SPP leads to stronger couple to the SAW. The result in a broader band gap and therefore broader peak in the reflectivity.

4.4 Summary

This chapter has presented an extension to the method suggested by Tikhodeev et al [58], for numerical calculation for electromagnetic fields in multilayer structures. The extended method now allows for the calculation of propagating sinusoidal gratings. This method was demonstrated by considering the optical properties of a thin Au foil for strong coupling between SPPs. The parameters of the SAW induced corrugation were varied and the effect of the reflectivity of the foil were reported.

The use of a SAW to produced propagating conformal modulations at each foil interface was numerically investigated. It was shown that this caused the development of sharp dips in the reflectivity spectrum and smaller features at a lower frequency. This features were due the SPPs at each interface, the large feature due to the V/M SPP and the smaller due to the M/G SPP.

It was also shown that corrugation amplitude effected the strength of the coupling

between the SAW and the SPP. This lead to larger features in the reflectivity for increased B. The increase in dip depth was shown to be proportional to B^2 up to $B \sim 2$ nm. Above this non-linearities in the coupling become important.

The effect of the angle of incidence on the reflectivity spectrum of the thin Au foil was discussed. The angle of incidence controlled the selection of the SPP dispersion that fell inside the light cone. Therefore, the spectral position of SAW induced gaps in the spectrum could be set using the angle of incidence.

It was shown that the thickness of the Au foil had effects on the strength and spectral position of the dips in the reflectivity. Reducing the thickness of the foil lead to deceased reflectivity dip depth as light increasingly coupled to the continuum in the substrate. The blue-shift associated with increasing foil thickness was the result of the change in the nature of the system from thin foil to bulk medium.

Finally, the effect of the SAW wavevector on reflectivity spectrum of a thin Au foil was investigated. It was found that the increase in wavevector lead to a blue shift of the dips in the reflectivity. This was due to the increased width of the SAW induced Brillouin zone leading to SAW induced band gaps in the folded-dispersion occurring at higher frequencies. The increased strength of the effect was apparent with wider shallower dips due to stronger SAW-SPP coupling around the Restrahlen band.

5 Conclusion

This thesis discussed the RAO effect in both ionic and metallic crystal lattices. In the introductory chapter a discussion of the previous research was given, as well as a discussion of the the components necessary for the RAO effect to occur. The original case of bulk exciton polaritons, followed by the case of microcavity polaritons was also presented. A general concept of the RAO interaction was given, which showed that a polarization could be used to mediate and enhance the acousto-optic interaction, in sharp contrast to the conventional acousto-optic effect. Practically, this was achieved by the spatial and temporal modulation of polaritons, which allowed the acoustic wave to couple to solid state excitaions.

5.1 RAO Effect in Ionic Crystals: One Anharmonicity

The RAO effect for individual anhamonic coupling between the AW and the polarization has been considered for cubic anharmoncity in semi-infinite CuCl and for quartic anharmoncity in semi-infinite TlCl. The numerical model was derived from a modification of Hopfield's macroscopic equations. For the RAO effect in CuCl the results of the numerical model were compared with approximate analytic results. It was shown that the AW induced TO-phonon transitions caused band gaps in the dispersion, which lead to spikes in the total Bragg reflectivity. The spectral position of the peaks was shown to depend on the AW frequency and the peak strength on the AW intensity.

The strength of the peaks was also shown to be dependent on the detuning of the acoustically induced band gaps from the Restrahlen band for both CuCl and TlCl. The width of the AW induced band gaps increased as the detuning decreased leading to larger peaks in the total Bragg reflectivity. At both very high and very low detuning the contribution of higher Bragg replicas was severely reduced. This can be attributed to the large discrepancy between the AW modulation period and the TO-phonon wavelength. The reflectivity peaks in the LP branch take on a more cusp-like appearance at low detuning. This was the result of the accumulation of AW induced band gaps just below the Restrahlen band. A similar accumulation effect can also happen in the UP branch at the top edge of the Restrahlen band but does not cause a cusp-like feature. The interaction length of the AW with the electric field was shown to be greatly reduced compared to the *conventional* acousto-optic effect.

The RAO effect in CuCl and TlCl did demonstrate some qualitative differences. In CuCl the cubic anharmonicity is dominant and the corresponding scattering channel can produce any TO-phonon transition. In TlCl the quartic anharmonicity is dominant and the associated scattering channel produces only even order (n even) TO-phonon transitions. As a result the first order AW induced band gap in TlCl is analogous to the second order AW induced band in CuCl. Finally, the quartic anharmonic RAO effect in TlCl produces a renormalisation of the TO-phonon frequency that was not present in the cubic effect.

5.2 RAO Effect in Ionic Crystals: Two Anharmonicities

The TO-phonon RAO effect was investigated for an interatomic potential with two anharmonic terms that were treated on an equal footing. The investigated system was semi-infinite $LiNbO_3$. This material was chosen for its large cubic and quartic anharmonicity and ionic properties. It was necessary that the anharmonicity was large, so that both cubic and quartic terms could be equally treated.

The strength of the coupling between the TO-phonon and the AW was estimated. It was found that the coupling strength $\sigma_{3,4}$ differed by as much as an order of magnitude. However, on further investigation, and despite the large discrepancy in coupling strength, σ_4 was still sufficiently large enough to make significant impact on

the reflectivity of the system.

With the inclusion of two anharmonic terms in the macroscopic equations the phase difference has become an important material parameter. It was shown that the maximum destructive interference occurred between the two anharmonicities when $\phi = \pi/2$. The dependence of the Bragg reflectivity on ϕ alters when the band gaps have small detuning from the restrahlen band. This was due to the break down of the Bragg condition near ω_0.

The tunable Bragg reflectivity spectrum due to the RAO effect in $LiNbO_3$, formed the basis of a proposed tunable THz filter. The design of the filter involved a $LiNbO_3$ layer sandwiched between two doped GaAs films, which are transparent to THz radiation. The current passing through the GaAs films would provide the compressions and rarefactions of the AW. This would result in an RAO effect in the $LiNbO_3$ with a tunable reflectivity spectrum.

5.3 RAO Effect in Metals

The use of the scattering matrix method for the calculation of electromagnetic field in multilayer structures was discussed. The extension allows for the calculation of a multilayered structure undergoing sinusoidal modulation by a propagating acoustic wave. A demonstration of the method was given by calculating the optical properties of a SAW-modulated Au foil. The investigated system was of an Au foil on a glass substrate, the SAW generated propagating conformal modulations of the foil, when the thickness of the foil d was small compared to the SAW wavelength. The SPPs at each interface allowed the SAW-induced modulations to alter the reflectivity spectrum of the Au foil.

The corrugation amplitude B played a significant role in controlling the modifications of the Au foils optical properties. Increased B led to large dips in the reflectivity at the resonant positions in the spectrum. The depth of the dips was shown to increase proportional to B^2 up to $B \sim 2$ nm. Above this value the variations were of a higher order.

The angle of light incidence ϕ of the light on the Au foil was shown to effect the regions of the spectrum that fell inside the light cone. This allowed the resonant

position of the SAW-induced gaps, which produced reflectivity dips, to be set. By deceasing ϕ the crossing points in the folded dispersion occurred at higher frequency regions found along the dispersion branches. This lead to blue shifted dips in the reflectivity spectrum for reduced ϕ.

Variations in the thickness of the Au foil effected both the strength and the spectral position of the reflectivity peaks. It was shown that decreasing foil thickness reduced the depth of the peak in the reflectivity and increased its width. This was caused by increased coupling of the incident light directly to the continuum in the substrate.

It was shown that the SAW wavevector K also played an important role in determining the spectral position of the dips in the SAW modified reflectivity. An increase in K lead to widening of the SAW induced Brillouin zone and to blue-shifted band gaps, as the separation of SPP branches increases. As a result the dips in the reflectivity spectrum are also blue-shifted This reduces the detuning of the resonant points from the Restrahlen band resulting in deeper and wider reflectivity dips due to stronger SAW-SPP coupling.

5.4 Future Work

In this thesis the RAO effect for TO-phonon polaritons was presented for a semi-infinite geometry. The effect a different geometry would have on the AW modulated reflectivity and transmissivity would be a possible line of inquiry. It would also prudent to consider whether an increase in coupling strength could be achieved by using a different geometry. It is worth noting that as the RAO coupling strength is inversely dependent on the AW velocity square root of the AW velocity for cubic and quartic anharmonicities, respectively. A reduction of the acoustic velocity by using a SAW may impact the strength of the RAO effect.

It may also be a valuable exercise to investigate the possibility of a coherent TO-phonon polariton state lasing in the THz range. The effect a dynamical superlattice might have on such a device may also be of interest. Such a device would would allow easy access to the THz band as sources of this type are currently lacking.

Appendix A Derivation of the Eigenvalue Problem

The eigenvalue problem that is the basis of all the calculations in chapters 2 and 3 is derived in this appendix. The derivation is given here for a ferroelectric material with both third and fourth order anharmonicity, the individual anharmonic coupling derivation is accessed by setting $\sigma_3 = 0$ or $\sigma_4 = 0$, respectively. This appendix is split into two cases; the eigenvalue problem for complex $\omega(k)$ (quasienergy) with real k and for complex $k(\omega)$ (quasimomentum) with real ω.

A.1 Quasienergy Dispersion

Consider Eq. (2.4b) for the first case, $\omega(k)$, k is real and $\gamma = 0$ for convince. By introducing

$$\tilde{\omega}_0^2 = \omega_0^2 + 4\omega_0\sigma_4,$$

Eq. (2.4b) can be rewritten as

$$\left[\tilde{\omega}_0^2 - (\omega + n\Omega)^2\right] P_n + 2\sigma_3\omega_0(P_{n+1}e^{-i\phi} + P_{n-1}e^{i\phi}) + 2\sigma_4\omega_0(P_{n+2} + P_{n-2}) = \frac{\varepsilon_b\,\omega_R^2}{4\pi}\,E_n. \tag{A.1}$$

This can be simplified by defining the matrix

$$B = \begin{pmatrix} \tilde{\omega}_0^2 & 2\sigma_3\omega_0 e^{i\phi} & 2\sigma_4\omega_0 & \cdots & 0 \\ 2\sigma_3\omega_0 e^{-i\phi} & \ddots & \ddots & \ddots & \vdots \\ 2\sigma_4\omega_0 & \ddots & \ddots & \ddots & 2\sigma_4\omega_0 \\ \vdots & \ddots & \ddots & \ddots & 2\sigma_3\omega_0 e^{i\phi} \\ 0 & \cdots & 2\sigma_4\omega_0 & 2\sigma_3\omega_0 e^{-i\phi} & \tilde{\omega}_0^2 \end{pmatrix}$$

so that Eq. (A.1) can be written as

$$\frac{4\pi}{\varepsilon_b\omega_R^2}\left[-(\omega+n\Omega)^2P_n+B_{nm}P_m\right]=E_n.$$

The electric field eigenvalue E_n is then removed by the substitution of Eq. (2.4a). If another matrix is defined

$$A_{nm}=-\frac{B_{nm}}{\omega_R^2c^2}-\left[\frac{(k+nK)^2}{\varepsilon_bc^2}+\frac{1}{c}\right]\delta_{nm},$$

then Eq. (A.1) can be written as

$$\frac{1}{c^2\omega_R^2}(\omega+n\Omega)^4P_n+(\omega+n\Omega)^2A_{nm}P_m+\frac{(k+nK)^2}{\varepsilon_bc^2}B_{nm}P_m=0.$$

By defining the vectors $Q_n=\omega P_n$, $R_n=\omega^2P_n$ and $S_n=\omega^3P_n$ this can be written as the eigenvalue problem for ω

$$\hat{\mathbb{W}}\vec{\mathbb{X}}=\omega\vec{\mathbb{X}}.$$

The eigenvectors are defined as $\vec{\mathbb{X}}=(S_n,R_n,Q_n,P_n)^{\mathrm{T}}$ and the matrix $\hat{\mathbb{W}}$ is defined as

$$\hat{\mathbb{W}}=\begin{pmatrix}-4n\Omega\delta_{nm} & X_{nm} & Y_{nm} & Z_{nm}\\ \delta_{nm} & 0 & 0 & 0\\ 0 & \delta_{nm} & 0 & 0\\ 0 & 0 & \delta_{nm} & 0\end{pmatrix},$$

where

$$X_{nm}=-c^2\omega_R^2\left[\frac{6(n\Omega)^2}{c^2\omega_R^2}\delta_{nm}+A_{nm}\right],$$
$$Y_{nm}=-c^2\omega_R^2\left[\frac{4(n\Omega)^3}{c^2\omega_R^2}\delta_{nm}+2n\Omega A_{nm}\right],$$
$$Z_{nm}=-c^2\omega_R^2\left[\frac{(n\Omega)^4}{c^2\omega_R^2}\delta_{nm}+(n\Omega)^2A_{nm}+\frac{(k+nK)^2}{\varepsilon_bc^2}B_{nm}\right].$$

A.2 Quasimomentum Dispersion

The starting point for the derivation of the quasimomentum eigenvalue problem, in which ω is real and k complex, is the same as for the quasienergy problem, Eq. (2.4b). In this case γ is non-zero and by defining the vector

$$G_n=-(\omega-n\Omega)^2+\tilde{\omega}_0^2-2i\gamma(\omega+n\Omega),$$

and the matrix

$$C = \frac{4\pi}{\varepsilon_b \omega_R^2} \begin{pmatrix} G_{-n_r} & 2\sigma_3\omega_0 e^{i\phi} & 2\sigma_4\omega_0 & \cdots & 0 \\ 2\sigma_3\omega_0 e^{-i\phi} & \ddots & \ddots & \ddots & \vdots \\ 2\sigma_4\omega_0 & \ddots & \ddots & \ddots & 2\sigma_4\omega_0 \\ \vdots & \ddots & \ddots & \ddots & 2\sigma_3\omega_0 e^{i\phi} \\ 0 & \cdots & 2\sigma_4\omega_0 & 2\sigma_3\omega_0 e^{-i\phi} & G_{n_r} \end{pmatrix},$$

Eq. (2.4b) can be rewritten as

$$\sum_m C_{nm} P_m = E_n, \tag{A.2}$$

where n_r is the Bragg replica cutoff. By making P_m the subject of Eq. (A.2), which is possible only because C_{nm} is not k dependent, and substituting to remove P_n from Eq. (2.4a) gives,

$$\left[-\frac{\varepsilon_b}{c^2}(\omega + n\Omega)^2 + (k + nK)^2\right] E_n = \sum D_{nm} E_m \tag{A.3}$$

where the matrix A_{nm} is

$$D_{nm} = \frac{4\pi}{c^2}(\omega + n\Omega)^2 C^{-1}_{nm}.$$

By defining the vector

$$F_n = \left(k + nK + \sqrt{\varepsilon_b}\frac{\omega + n\Omega}{c}\right) E_n,$$

Eq. (A.3) can be rewritten as

$$\left(k + nK - \sqrt{\varepsilon_b}\frac{\omega + n\Omega}{c}\right) F_n = \sum D_{nm} E_m.$$

This can be written as the eigenvalue problem

$$\hat{\mathbb{V}}\vec{\mathbb{Y}} = k\vec{\mathbb{Y}}$$

where

$$\hat{\mathbb{V}} = \begin{pmatrix} -\sqrt{\varepsilon_b}\frac{\omega\hat{1}+n\Omega}{c} - \hat{n}K & \hat{1} \\ \hat{D} & \sqrt{\varepsilon_b}\frac{\omega\hat{1}+n\Omega}{c} - \hat{n}K \end{pmatrix},$$

$\hat{1}$ is an $n_r \times n_r$ identity matrix and

$$\vec{\mathbb{Y}} = \begin{pmatrix} E_n \\ F_n \end{pmatrix}.$$

Appendix B Acousto-Plasmonics: Electromagnetic Field, Interface Transfer Matrix Derivation and Scattering Matrix Formula.

This appendix presents the derivation of the transfer matrices across the vacuum-to-metal (V/M) boundary and the metal-to-glass (M/G) boundary. Both of these matrices form the basis for all the calculation of the RAO effect in thin metal films.

B.1 Electromagnetic Field Derivation

The starting point for the derivation of the electromagnetic field is Maxwell's cross product equations,

$$\frac{1}{c}\frac{\partial \mathbf{H}}{\partial t} = \nabla \times \mathbf{E}, \tag{B.1a}$$

$$-\frac{1}{c}\frac{\partial \mathbf{D}}{\partial t} = \nabla \times \mathbf{H}. \tag{B.1b}$$

The system that they will be applied to has two boundaries and a thickness of d, which is the metallic layer thickness. These boundaries have a corrugation that is acoustically induced with an amplitude B and given by

$$z_0(x,t) = B\cos(Kx - \Omega t), \tag{B.2a}$$

$$z_1(x,t) = z_0(x,t) + d, \tag{B.2b}$$

were K and Ω are the acoustic wavevector and frequency, respectively.

Only p-polarized electric fields can be used to access surface plasmon polaritons

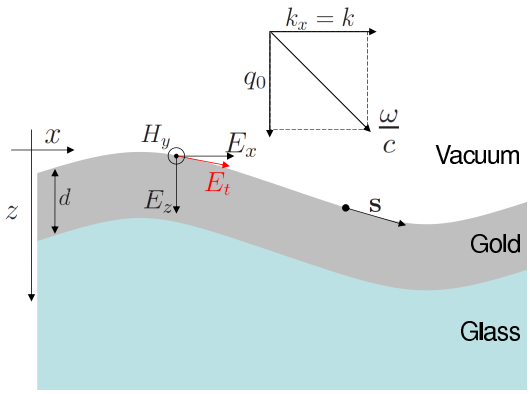

Figure B.1: The geometry of the RAO effect in a thin gold films. The electromagnetic field is p-polarized and E_t is the electric field component along the corrugated surface, **s** is the unit tangent vector to the surface.

(SPP). Thus, the magnetic field vector can be written as

$$\mathbf{H} = \begin{pmatrix} 0 \\ H(x,z,t) \\ 0 \end{pmatrix}.$$

The y-components of $\vec{H}$ in each layer are

$$H_V(x,z,t) = \sum_n \left[\mathcal{A}_n^{(+,V)} e^{iq_n z} + \mathcal{A}_n^{(-,V)} e^{-iq_n z}\right] e^{ikx - i\omega t} e^{i(Kx - \Omega t)n}, \tag{B.3a}$$

$$H_M(x,z,t) = \sum_n \left[\mathcal{A}_n^{(+,M)} e^{ip_n z} + \mathcal{A}_n^{(-,M)} e^{-ip_n z}\right] e^{ikx - i\omega t} e^{i(Kx - \Omega t)n}, \tag{B.3b}$$

$$H_G(x,z,t) = \sum_n \left[\mathcal{A}_n^{(+,G)} e^{iq_n^{(G)} z} + \mathcal{A}_n^{(-,G)} e^{-iq_n^{(G)} z}\right] e^{ikx - i\omega t} e^{i(Kx - \Omega t)n}. \tag{B.3c}$$

The partial wave amplitudes in the positive and negative z-direction for the vacuum, metal and glass are $\mathcal{A}_n^{(\pm,V,M,G)}$, respectively, and the wavevectors for these materials are q_n, p_n and $q_n^{(G)}$, respectively. The dimensions are $2n_{\max} + 1$ for the calligraphic letters.

The wavevectors are derived by substituting the Eqs. (B.3) into Eq. (B.1). The results of this are

$$q_n = \sqrt{\frac{1}{c^2}(\omega + n\Omega)^2 - (k + nK)^2}, \tag{B.4a}$$

$$p_n = \sqrt{\frac{\varepsilon_M(\omega)}{c^2}(\omega + n\Omega)^2 - (k + nK)^2}, \tag{B.4b}$$

$$q_n^{(G)} = \sqrt{\frac{\varepsilon_G}{c^2}(\omega + n\Omega)^2 - (k + nK)^2}, \tag{B.4c}$$

where ε_G is the dielectric constant of the glass substrate. The dielectric constant of

the metal $\varepsilon_M(\omega)$ has been taken in a Lorentz-Drude model [59]. On the scale of $n_{\max}\Omega$ The metallic dielectric constant is weakly dependent on ω, therefore any discrepancies between $\varepsilon_M(\omega)$ and $\varepsilon_M(\omega + n\Omega)$ can be neglected.

The x and y components of the electric field can now be calculated through Eq. (B.1b) by using the material relation $\mathbf{D}(\omega) = \varepsilon_M(\omega)\mathbf{E}(\omega)$ and the H-field components given in Eqs. (B.3). As p-polarized light is being used the y-component of the E-field is zero and the x- and z-components are given by

$$\frac{i}{c}E_n^{(x)}(x,z) = -\frac{1}{\varepsilon(\omega)}\frac{\partial H_n(x,z)}{\partial z_0}\frac{1}{\omega + n\Omega}, \tag{B.5a}$$

$$\frac{1}{c}E_n^{(z)}(x,z) = \frac{1}{\varepsilon(\omega)}\frac{k + nK}{\omega + n\Omega}H_n(x,z). \tag{B.5b}$$

By the substitution of Eqs. (B.3) into Eqs. (B.5) we can derive the E-field from the H-field. For the sake of brevity throughout the remainder of this appendix, the metallic dielectric constant is written with implicit ω dependence ε_M.

We can finally write the electric and magnetic field in all layers in terms of the partial wave amplitudes. These are, in the vacuum

$$\mathbf{H}_V(x,z,t) = \sum_n \begin{pmatrix} 0 \\ \mathcal{A}_n^{(+,V)}e^{iq_n z} + \mathcal{A}_n^{(-,V)}e^{-iq_n z} \\ 0 \end{pmatrix} e^{ikx - i\omega t}e^{i(Kx - \Omega t)n}, \tag{B.6a}$$

$$\mathbf{E}_V(x,z,t) = \sum_n \begin{pmatrix} -\frac{cq_n}{\varepsilon_0(\omega+n\Omega)}\left[\mathcal{A}_n^{(+,V)}e^{iq_n z} - \mathcal{A}_n^{(-,V)}e^{-iq_n z}\right] \\ 0 \\ \frac{c(k+nK)}{\varepsilon_0(\omega+n\Omega)}\left[\mathcal{A}_n^{(+,V)}e^{iq_n z} + \mathcal{A}_n^{(-,V)}e^{-iq_n z}\right] \end{pmatrix} e^{ikx - i\omega t}e^{i(Kx - \Omega t)n}, \tag{B.6b}$$

in the metal

$$\mathbf{H}_M(x,z,t) = \sum_n \begin{pmatrix} 0 \\ \mathcal{A}_n^{(+,M)}e^{ip_n z} + \mathcal{A}_n^{(-,M)}e^{-ip_n z} \\ 0 \end{pmatrix} e^{ikx - i\omega t}e^{i(Kx - \Omega t)n}, \tag{B.7a}$$

$$\mathbf{E}_M(x,z,t) = \sum_n \begin{pmatrix} -\frac{cp_n}{\varepsilon_M(\omega+n\Omega)}\left[\mathcal{A}_n^{(+,M)}e^{ip_n z} - \mathcal{A}_n^{(-,M)}e^{-ip_n z}\right] \\ 0 \\ \frac{c(k+nK)}{\varepsilon_M(\omega+n\Omega)}\left[\mathcal{A}_n^{(+,M)}e^{ip_n z} + \mathcal{A}_n^{(-,M)}e^{-ip_n z}\right] \end{pmatrix} e^{ikx - i\omega t}e^{i(Kx - \Omega t)n}, \tag{B.7b}$$

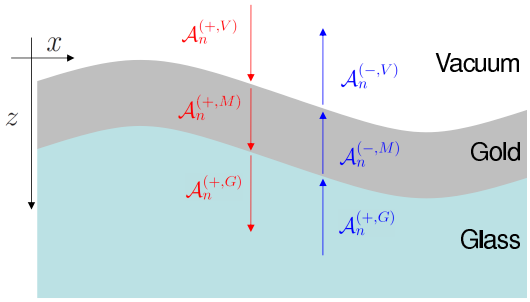

Figure B.2: The definitions of the partial wave amplitudes.

and in the glass substrate

$$\mathbf{H}_G(x,z,t) = \sum_n \begin{pmatrix} 0 \\ \mathcal{A}_n^{(+,G)} e^{iq_n^{(G)} z} + \mathcal{A}_n^{(-,G)} e^{-iq_n^{(G)} z} \\ 0 \end{pmatrix} e^{ikx - i\omega t} e^{i(Kx - \Omega t)n}, \tag{B.8a}$$

$$\mathbf{E}_G(x,z,t) = \sum_n \begin{pmatrix} -\frac{cq_n^{(G)}}{\varepsilon_G(\omega + n\Omega)} \left[\mathcal{A}_n^{(+,G)} e^{iq_n^{(G)} z} - \mathcal{A}_n^{(-,G)} e^{-iq_n^{(G)} z} \right] \\ 0 \\ \frac{c(k+nK)}{\varepsilon_G(\omega+n\Omega)} \left[\mathcal{A}_n^{(+,G)} e^{iq_n^{(G)} z} + \mathcal{A}_n^{(-,G)} e^{-iq_n^{(G)} z} \right] \end{pmatrix} e^{ikx - i\omega t} e^{i(Kx - \Omega t)n}. \tag{B.8b}$$

B.2 Interface Transfer Matrix Derivation

Having derived the wavevectors in each layer and the corresponding E- and H-fields, boundary conditions (BCs) can now be applied to calculate the partial wave amplitudes. The boundary conditions require that the H-field amplitude and the component of the E-field amplitude that is tangential to the boundary are continuous across the boundary. For H-field continuity across the vacuum to metal (V/M) interface, Eqs. (B.6a) and (B.7a) are equated at $z = z_0$ and the $e^{ikx - i\omega t}$ term cancelled to give

$$\sum_n \left[\mathcal{A}_n^{(+,V)} e^{iq_n B \cos\varphi} + \mathcal{A}_n^{(-,V)} e^{-iq_n B \cos\varphi} \right] e^{i\varphi n} = \sum_n \left[\mathcal{A}_n^{(+,M)} e^{ip_n B \cos\varphi} + \mathcal{A}_n^{(-,M)} e^{-ip_n B \cos\varphi} \right] e^{i\varphi n}, \tag{B.9}$$

where, for the sake of brevity, $\varphi = Kx - \Omega t$. For the E-field BC the tangential component to the interface must be derived. Therefore, the starting point is to define

the tangent unit vector

$$\mathbf{s} = \begin{pmatrix} 1 \\ 0 \\ z_0'(x,t) \end{pmatrix} = \begin{pmatrix} 1 \\ 0 \\ -KB\sin(\varphi) \end{pmatrix}$$

where $z_0'(x,t)$ is the differentiation of $z_0(x,t)$ with respect to x. Therefore, the magnitude of the tangential electric field is

$$E_t = \frac{\mathbf{s}\cdot\mathbf{E}}{\sqrt{\mathbf{s}\cdot\mathbf{s}}} = E_t = \frac{E_x + z_0' E_z}{\sqrt{1+(z_0')^2}}.$$

After canceling the common denominator, the tangential E-field boundary condition can be written as

$$E_V^{(x)} + z_0' E_V^{(z)} = E_M^{(x)} + z_0' E_M^{(z)}.$$

Thus, using Eqs. (B.6b) and (B.7b) gives

$$\begin{aligned}
&\sum_n \Bigg[-\frac{cq_n}{\varepsilon_0(\omega+n\Omega)} \left\{ \mathcal{A}_n^{(+,V)} e^{iq_n B\cos\varphi} - \mathcal{A}_n^{(-,V)} e^{-iq_n B\cos\varphi} \right\} \\
&\quad - KB\sin(\varphi)\frac{c(k+nK)}{\varepsilon_0(\omega+n\Omega)} \left\{ \mathcal{A}_n^{(+,V)} e^{iq_n B\cos\varphi} + \mathcal{A}_n^{(-,V)} e^{-iq_n B\cos\varphi} \right\} \Bigg] e^{i\varphi n} = \\
&\sum_n \Bigg[-\frac{cp_n}{\varepsilon_M(\omega+n\Omega)} \left\{ \mathcal{A}_n^{(+,M)} e^{ip_n B\cos\varphi} - \mathcal{A}_n^{(-,M)} e^{-ip_n B\cos\varphi} \right\} \\
&\quad - KB\sin(\varphi)\frac{c(k+nK)}{\varepsilon_M(\omega+n\Omega)} \left\{ \mathcal{A}_n^{(+,M)} e^{ip_n B\cos\varphi} + \mathcal{A}_n^{(-,M)} e^{-ip_n B\cos\varphi} \right\} \Bigg] e^{i\varphi n}
\end{aligned} \tag{B.10}$$

In general the Fourier transform of $e^{ir\cos\psi}$ gives

$$e^{ir\cos\psi} = \sum_l i^l J_l(r) e^{i\psi l}, \tag{B.11}$$

where $J_l(r)$ is Bessel function of the first kind. The Fourier transform of the $\sin(\psi)\exp[ir\cos(\psi)]$ term can calculated from Eq. (B.11)

$$\frac{\partial}{\partial\psi} e^{ir\cos\psi} = -ir\sin\psi e^{ir\cos\psi} = \sum_l i^l il J_l(r) e^{i\psi l}.$$

Thus,

$$\sin(\psi) e^{ir\cos(\psi)} = -\sum_l \frac{i^l l}{r} J_l(r) e^{i\psi l}, \tag{B.12}$$

where l is an integer [65].

We can now apply Eqs. (B.11) and (B.12) to Eqs (B.9) and (B.10), this will allow them to be written more compactly with the use of the Bessel functions. Eq. (B.9) becomes

$$\sum_{n,m}\left[\mathcal{A}_n^{(+,V)}J_m(q_nB)+\mathcal{A}_n^{(-,V)}J_m(-q_nB)\right]e^{i\varphi(n+m)}i^m=$$
$$\sum_{n,m}\left[\mathcal{A}_n^{(+,M)}J_m(p_nB)+\mathcal{A}_n^{(-,M)}J_m(-p_nB)\right]e^{i\varphi(n+m)}i^m, \tag{B.13}$$

and Eq. (B.10) becomes

$$\begin{aligned}\sum_{n,m}\Bigg[&-\frac{cq_n}{\varepsilon_0(\omega+n\Omega)}\left\{\mathcal{A}_n^{(+,V)}J_m(q_nB)-\mathcal{A}_n^{(-,V)}J_m(-q_nB)\right\}i^m\\&+KB\frac{c(k+nK)}{\varepsilon_0(\omega+n\Omega)}\Bigg\{\mathcal{A}_n^{(+,V)}J_m(q_nB)\frac{m}{q_nB}\\&\qquad-\mathcal{A}_n^{(-,V)}J_m(-q_nB)\frac{m}{q_nB}\Bigg\}i^m\Bigg]e^{i\varphi(n+m)}=\\\sum_{n,m}\Bigg[&-\frac{cp_n}{\varepsilon_M(\omega+n\Omega)}\left\{\mathcal{A}_n^{(+,M)}J_m(p_nB)-\mathcal{A}_n^{(-,M)}J_m(-p_nB)\right\}i^m\\&+KB\frac{c(k+nK)}{\varepsilon_M(\omega+n\Omega)}\Bigg\{\mathcal{A}_n^{(+,M)}J_m(p_nB)\frac{m}{p_nB}\\&\qquad-\mathcal{A}_n^{(-,M)}J_m(-p_nB)\frac{m}{p_nB}\Bigg\}i^m\Bigg]e^{i\varphi(n+m)}\end{aligned} \tag{B.14}$$

To express the boundary conditions in matrix form it is necessary to let $n+m=s$ and $m=s-n$ so in general

$$\sum_{n,m}J_m(r_n)e^{i\psi(n+m)}\rightarrow\sum_{n,s}J_{s-n}(r_n)e^{i\psi s}. \tag{B.15}$$

If we allow $s=m$ and apply the above to Eqs. (B.13) and (B.14) we can rewrite the boundary conditions for the H-field as

$$\sum_{n,m}\left[\mathcal{A}_n^{(+,V)}J_{m-n}(q_nB)+\mathcal{A}_n^{(-,V)}J_{m-n}(-q_nB)\right]i^{m-n}e^{i\varphi m}=$$
$$\sum_{n,m}\left[\mathcal{A}_n^{(+,M)}J_{m-n}(p_nB)+\mathcal{A}_n^{(-,M)}J_{m-n}(-p_nB)\right]i^{m-n}e^{i\varphi m}, \tag{B.16}$$

and for the tangential E-field, Eq. (B.14) becomes

$$\begin{aligned}
&\sum_{n,m}\Bigg[-\frac{cq_n}{\varepsilon_0(\omega+n\Omega)}\left\{\mathcal{A}_n^{(+,V)}J_{m-n}(q_nB)-\mathcal{A}_n^{(-,V)}J_{m-n}(-q_nB)\right\}\\
&\quad + KB\frac{c(k+nK)}{\varepsilon_0(\omega+n\Omega)}\Bigg\{\mathcal{A}_n^{(+,V)}J_{m-n}(q_nB)\frac{m-n}{q_nB}\\
&\qquad\qquad -\mathcal{A}_n^{(-,V)}J_{m-n}(-q_nB)\frac{m-n}{q_nB}\Bigg\}\Bigg]i^{m-n}e^{i\varphi m} =\\
&\sum_{n,m}\Bigg[-\frac{cp_n}{\varepsilon_M(\omega+n\Omega)}\left\{\mathcal{A}_n^{(+,M)}J_{m-n}(p_nB)-\mathcal{A}_n^{(-,M)}J_{m-n}(-p_nB)\right\}\\
&\quad + KB\frac{c(k+nK)}{\varepsilon_M(\omega+n\Omega)}\Bigg\{\mathcal{A}_n^{(+,M)}J_{m-n}(p_nB)\frac{m-n}{p_nB}+\\
&\qquad\qquad -\mathcal{A}_n^{(-,M)}J_{m-n}(-p_nB)\frac{m-n}{p_nB}\Bigg\}\Bigg]i^{m-n}e^{i\varphi m}.
\end{aligned} \tag{B.17}$$

These two equations can now be used to derive the transfer matrix at the V/M interface.

It is necessary to equate the coefficients of the exponential terms $\exp[i\varphi m]$ in Eqs. (B.16) and (B.17) and express the result in matrix form

$$\begin{pmatrix}\mathcal{V}^{(1,1)} & \mathcal{V}^{(1,2)}\\ \mathcal{V}^{(2,1)} & \mathcal{V}^{(2,2)}\end{pmatrix}\begin{pmatrix}\mathcal{A}_n^{(+,V)}\\ \mathcal{A}_n^{(-,V)}\end{pmatrix} = \begin{pmatrix}\mathcal{M}^{(1,1)} & \mathcal{M}^{(1,2)}\\ \mathcal{M}^{(2,1)} & \mathcal{M}^{(2,2)}\end{pmatrix}\begin{pmatrix}\mathcal{A}_n^{(+,M)}\\ \mathcal{A}_n^{(-,M)}\end{pmatrix}. \tag{B.18}$$

Then by defining all open faced letters as either $2(2n_r+1)$ square matrices or equivalent sized vectors, the elements of $\mathbb{V}$ are

$$\mathcal{V}_{m,n}^{(1,1)} = J_{m-n}(q_nB)i^{m-n}, \tag{B.19a}$$

$$\mathcal{V}_{m,n}^{(1,2)} = J_{m-n}(-q_nB)i^{m-n}, \tag{B.19b}$$

$$\mathcal{V}_{m,n}^{(2,1)} = \left[-\frac{cq_n}{\omega+n\Omega}J_{m-n}(q_nB)i^{m-n} + K\frac{c(k+nK)}{\omega+n\Omega}J_{m-n}(q_nB)i^{m-n}\frac{m-n}{q_n}\right], \tag{B.19c}$$

$$\mathcal{V}_{m,n}^{(2,2)} = \left[\frac{cq_n}{\omega+n\Omega}J_{m-n}(-q_nB)i^{m-n} - K\frac{c(k+nK)}{\omega+n\Omega}J_{m-n}(-q_nB)i^{m-n}\frac{m-n}{q_n}\right], \tag{B.19d}$$

and the elements of $\mathbb{M}$ are

$$\mathcal{M}_{m,n}^{(1,1)} = J_{m-n}(p_n B) i^{m-n}, \tag{B.20a}$$

$$\mathcal{M}_{m,n}^{(1,2)} = J_{m-n}(-p_n B) i^{m-n}, \tag{B.20b}$$

$$\mathcal{M}_{m,n}^{(2,1)} = \left[-\frac{c p_n}{\varepsilon_M(\omega + n\Omega)} J_{m-n}(p_n B) i^{m-n} + K \frac{c(k+nK)}{\varepsilon_M(\omega+n\Omega)} J_{m-n}(p_n B) i^{m-n} \frac{m-n}{p_n} \right], \tag{B.20c}$$

$$\mathcal{M}_{m,n}^{(2,2)} = \left[\frac{c p_n}{\varepsilon_M(\omega + n\Omega)} J_{m-n}(-p_n B) i^{m-n} - K \frac{c(k+nK)}{\varepsilon_M(\omega+n\Omega)} J_{m-n}(-p_n B) i^{m-n} \frac{m-n}{p_n} \right]. \tag{B.20d}$$

As the transfer interface matrix $\mathbb{T}$ across the V/M boundary is defined by,

$$\begin{pmatrix} \mathcal{A}_n^{(+,V)} \\ \mathcal{A}_n^{(-,V)} \end{pmatrix} = \begin{pmatrix} \mathcal{T}_{1,1} & \mathcal{T}_{1,2} \\ \mathcal{T}_{2,1} & \mathcal{T}_{2,2} \end{pmatrix} \begin{pmatrix} \mathcal{A}_n^{(+,M)} \\ \mathcal{A}_n^{(-,M)} \end{pmatrix},$$

from comparison with Eq. (B.18) we can say

$$\mathbb{T}_{V/M} = \mathbb{V}^{-1}\mathbb{M}. \tag{B.21}$$

The $\mathbb{T}$-matrix at the second boundary between metal and glass (M/G) can be derived from an identical process. The matrix of coefficients of the partial wave amplitudes in glass $\mathbb{A}^G$ is designated $\mathbb{G}$ and has the elements

$$\mathcal{G}_{m,n}^{(1,1)} = J_{m-n}(q_n^{(G)} B) i^{m-n}, \tag{B.22a}$$

$$\mathcal{G}_{m,n}^{(1,2)} = J_{m-n}(-q_n^{(G)} B) i^{m-n}, \tag{B.22b}$$

$$\mathcal{G}_{m,n}^{(2,1)} = \left[-\frac{c q_n^{(G)}}{\varepsilon_G(\omega + n\Omega)} J_{m-n}(q_n^{(G)} B) i^{m-n} + K \frac{c(k+nK)}{\varepsilon_G(\omega+n\Omega)} J_{m-n}(q_n^{(G)} B) i^{m-n} \frac{m-n}{q_n^{(G)}} \right], \tag{B.22c}$$

$$\mathcal{G}_{m,n}^{(2,2)} = \left[\frac{c q_n^{(G)}}{\varepsilon_G(\omega + n\Omega)} J_{m-n}(-q_n^{(G)} B) i^{m-n} - K \frac{c(k+nK)}{\varepsilon_G(\omega+n\Omega)} J_{m-n}(-q_n^{(G)} B) i^{m-n} \frac{m-n}{q_n^{(G)}} \right]. \tag{B.22d}$$

Using the same approach as for the first boundary

$$\mathbb{T}_{M/G} = \mathbb{M}^{-1}\mathbb{G}. \tag{B.23}$$

Having now calculated the $\mathbb{T}$-matrix for both boundaries the reflectivity may be calculated form the total $\mathbb{T}$-matrix.

The $\mathbb{T}$ of the entire system is then calculated from

$$\mathbb{T}_{total} = \mathbb{T}_{V/M} \begin{pmatrix} \mathcal{E}^+ & 0 \\ 0 & \mathcal{E}^- \end{pmatrix} \mathbb{T}_{M/G}, \tag{B.24}$$

where $\mathcal{E}^- = \delta_{n,m}\exp(-ip_n d)$ and $\mathcal{E}^+ = \delta_{n,m}\exp(ip_n d)$. From the total $\mathbb{T}$-matrix the n^{th}-order Bragg reflectivity R_n and transmissivity T_n are given by

$$T_n = |\mathcal{A}_n^{+,G}|^2, \tag{B.25a}$$
$$R_n = |\mathcal{A}_n^{-,V}|^2. \tag{B.25b}$$

The amplitudes of the partial waves contributing to Eqs. (B.25) are given by

$$\mathcal{A}_n^{+,G} = \mathcal{T}_{1,1}^{-1}\mathcal{A}_n^{+,V}, \tag{B.26a}$$
$$\mathcal{A}_n^{-,V} = \mathcal{T}_{2,1}\mathcal{T}_{1,1}^{-1}\mathcal{A}_n^{+,V}. \tag{B.26b}$$

Where $\mathcal{A}_n^{+,V}$ is the partial wave amplitude vector for the incident light. For a monochromatic incident plane wave it is a column vector with $2n_r + 1$ elements, the central element is unity and the rest zero.

B.3 Scattering Matrix

To derive the scattering matrix an iterative process is required, based on the initial condition

$$\mathbb{S}_v = \mathbb{I}, \tag{B.27}$$

where $\mathbb{I}$ is a $2N \times 2N$ identity matrix, and the use of the transfer matrix at layer interfaces. In general, for a system in which the transfer matrix at a given layer L is

$$\mathbb{T}_L = \begin{pmatrix} \mathcal{T}_{1,1} & \mathcal{T}_{1,2} \\ \mathcal{T}_{2,1} & \mathcal{T}_{2,2} \end{pmatrix} \tag{B.28}$$

and the scattering matrix is

$$\mathbb{S}_L = \begin{pmatrix} \mathcal{S}_{1,1} & \mathcal{S}_{1,2} \\ \mathcal{S}_{2,1} & \mathcal{S}_{2,2,} \end{pmatrix} \tag{B.29}$$

then the scattering matrix to cross the boundary into the $(L+1)$th layer is

$$\mathbb{S}_{L+1} = \begin{pmatrix} \mathcal{D}\mathcal{S}_{11} & \mathcal{D}\mathcal{E} \\ \mathcal{S}_{21} + \mathcal{S}_{22}\mathcal{T}_{21}\mathcal{D}\mathcal{S}_{11} & \mathcal{S}_{22}\mathcal{T}_{21}\mathcal{D}\mathcal{E} + \mathcal{S}_{22}\mathcal{T}_{22} \end{pmatrix}, \tag{B.30}$$

where the $N \times N$ block matrix $\mathcal{E} = \mathcal{S}_{12}\mathcal{T}_{22} - \mathcal{T}_{21}$ and $\mathcal{D} = (\mathcal{T}_{11} - \mathcal{S}_{12}\mathcal{T}_{21})^{-1}$. To propagate the wave across the $(L+1)$ layer to the next boundary

$$\mathbb{S}_{L+1} = \begin{pmatrix} e^{i\mathcal{K}d} & \mathcal{O} \\ \mathcal{O} & \mathcal{I} \end{pmatrix} \mathbb{S}_L \begin{pmatrix} \mathcal{I} & 0 \\ 0 & e^{i\mathcal{K}d} \end{pmatrix}. \tag{B.31}$$

The block matrices $\mathcal{O}$ and $\mathcal{I}$ are $N \times N$ zero and identity matrices, respectively. The matrix $\mathcal{K}$ has the terms $k + nK$ along its diagonal, where k is the wavevector of light in the layer. Notice the absences of growing exponential terms in Eq. (B.31), removing the problem found in the transfer matrix method. The calculation of the necessary transfer matrices can be found in Appendix B.2.

Appendix C Dielectric Function of Au

In Eq (4.4) in section 4.1 the dielectric function has been split into two parts. The first is a classical Drude model, which describes the optical effects of the conduction electrons in the metal. The second part is a sum over a series of Lorentz oscillators which describes the optical properties of the bound electrons. The separation of the dielectric function into two components is allowed because the components operate in different spectral regions.

The Drude dielectric function assumes the electrons interact only with the metallic ions and not with each other. It can be derived by considering the current induced by a time varying electric field in a metal. Consider the Maxwell-Faraday equation

$$\nabla \times \mathbf{E} = \frac{1}{c}\frac{\partial \mathbf{E}}{\partial t} \tag{C.1}$$

and Ampere's Law with Maxwell's correction

$$\nabla \times \mathbf{H} = \frac{4\pi}{c}\mathbf{j} + \frac{1}{c}\frac{\partial \mathbf{E}}{\partial t}, \tag{C.2}$$

where $\mathbf{j}$ is current density. By making use of the vector calculus identity

$$\nabla \times \nabla \times \mathbf{F} = \nabla(\nabla \cdot \mathbf{F}) - \nabla^2 \mathbf{F},$$

and the condition that $\nabla \cdot \mathbf{E} = 0$ when there is no static charge and the fact that for a metal the current density can be written as $\mathbf{j} = \sigma(\omega)\mathbf{E}$, where $\sigma(\omega)$ is the conductivity, a combination of Eq. (C.1) and Eq. (C.2) can be written as

$$\nabla^2 \mathbf{E} = -\frac{1}{c}\frac{\partial}{\partial t}\left[\frac{4\pi}{c}\sigma(\omega)\mathbf{E} + \frac{1}{c}\frac{\partial \mathbf{E}}{\partial t}\right]. \tag{C.3}$$

If the wavelength of the electric field is far longer than the mean free path of the electrons in the current then we can write the electric field as

$$\mathbf{E} = \mathbf{E}_0 e^{i\omega t}.$$

Table C.1: The value of the parameters used for the calculation of a Lorentz-Drude model dielectric function.

Parameters	f_0	Γ_0	f_1	Γ_1	ω_1	f_2	Γ_2	ω_2	–
Au	0.760	0.053	0.024	0.241	0.415	0.010	0.345	0.830	–
Parameters	f_3	Γ_3	ω_3	f_4	Γ_4	ω_4	f_5	Γ_5	ω_5
Au	0.071	0.870	2.969	0.601	2.494	4.304	4.384	2.214	13.32

Substituting into Eq. (C.3) for $\mathbf{E}$ to give

$$\nabla^2\mathbf{E} = -\frac{\omega^2}{c^2}\left[1 + \frac{4\pi i\sigma(\omega)}{\omega}\right]\mathbf{E}.$$

From this the dielectric function is defined as

$$\varepsilon(\omega) = 1 + \frac{4\pi i\sigma(\omega)}{\omega}. \tag{C.4}$$

The conductivity of a metal is given by [60]

$$\sigma(\omega) = \frac{ne^2\tau}{m(1 - i\omega\tau)}, \tag{C.5}$$

where n is the number of electrons, τ is the time between collisions with the metallic ions and e and m is the electronic charge and mass, respectively. By substituting Eq. (C.5) into Eq. (C.4) and defining $\Gamma_0 = \tau^{-1}$ the Drude dielectric function for classical electrons can be written as

$$\varepsilon(\omega) = 1 - \frac{\omega_p^2}{\omega(\omega - i\Gamma_0)}, \tag{C.6}$$

where ω_p is defined in Eq. (1.16) in section 1.7.

The parameters necessary to model the dielectric function of Au are given in Table C.1 and are taken from Rakic et al [59].

References

[1] A. L. Ivanov and P. B. Littlewood. Acoustically induced stark effect for excitons in intrinsic semiconductors. *Phys. Rev. Lett.*, **87**, 136403 (2001).

[2] D. Fröhlich, A. Nöthe and K. Reimann. Observation of the resonant optical stark effect in a semiconductor. *Phys. Rev. Lett.*, **55**, 1335 (1985).

[3] A. Mysyrowicz, D. Hulin, A. Antonetti, A. Migus, W. T. Masselink and H. Morkoç. "Dressed excitons" in a multiple-quantum-well structure: Evidence for an optical stark effect with femtosecond response time. *Phys. Rev. Lett.*, **56**, 2748 (1986).

[4] L. Remer, B. Lüthi, H. Sauer, R. Geick and R. E. Camley. Nonreciprocal optical reflection of the uniaxial antiferromagnet mn$f$_2. *Phys. Rev. Lett.*, **56**, 2752 (1986).

[5] A. L. Ivanov and L. P. B. Resonant acousto-optics of microcavity polaritons. *Semicond. Sci. Technol.*, **18**, s428 (2003).

[6] K. Cho, K. Okumoto, N. I. Nikolaev and A. L. Ivanov. Bragg diffraction of microcavity polaritons by a surafce acoustic wave. *Phys. Rev. Lett.*, **94**, 226406 (2005).

[7] A. L. Ivanov. Resonant acousto-optic response of microcavity polaritons. *Physica Status Solidi (b)*, **202**, 2687 (2005).

[8] J. M. M. de Lima, M. van der Poel, P. V. Santos and J. M. Hvam. Phonon-induced polariton superlattices. *Phys. Rev. Lett.*, **97**, 045501 (2006).

[9] P. S. J. Russell. Bragg resonance of light in optical superlattices. *Phys. Rev. Lett.*, **56**, 596 (1986).

[10] P. V. Santos. Collinear light modulation by surface acoustic waves in latterly structure semiconductors. *J Appl. Phys.*, **86**, 5060 (2001).

[11] A. L. Ivanov. Acoustically Induced Superlattices: From Photons and Electrons to Excitons, To-phonons and Polaritons. In A. L. Ivanov and S. G. Tikhodeev, editors, *Problems of Condensed Matter Physics*, International Series of Monographs on Physics (Oxford University Press, 2007).

[12] R. H. Ritchie. Plasma loses by fast electrons in thin films. *Phys. Rev.*, **106**, 874 (1957).

[13] J. M. Pitarke, V. M. Silkin, E. V. Chulkov and P. M. Echenique. Theory of surface plasmons and surface-plasmon polaritons. *Rep. Prog. Phys.*, **70**, 1 (2007).

[14] G. W. Farnell. Types and properties of surface waves. In A. A. Oliner, editor, *Topics in Applied Physics*, volume 27 of *Topics in Applied Physics*, chapter 2, pages 13–22 (Springer-Verlag, 1978).

[15] G. P. Srivastava. *The Physics of Phonons*, chapter 4, pages 88–110 (IOP Publishing Ltd, 1990).

[16] R. A. Cowley. Anhamonic crystals. *Rep. Prog. Phys.*, **31**, 123 (1968).

[17] D. Pines and D. Bohm. A collective description of electron interactions: Ii. collective *vs* individual particle aspects of the interactions. *Phys. Rev.*, **85**, 338 (1952).

[18] J. M. Ziman. *The Principle of the Theory of Solids* (Cambridge, 1964).

[19] J. Hubbard. The dielectric theory of electronic interactions in solids. *Proc. Phys. Soc.*, **68**, 976 (1955).

[20] J. Sólyom. *Fundamentals of the Physics of Solids*, volume 3 (Springer, 2003).

[21] G. Dressel, Martin & Gr´uer. *Electrodynamics of Solids* (Cambridge University Press, Cambridge, 2003), netlibrary edition.

[22] C. J. Powell and J. B. Swan. Origin of the characteristic electron energy losses in aluminum. *Phys. Rev.*, **115**, 869 (1959).

[23] C. J. Powell and J. B. Swan. Origin of the characteristic electron energy losses in magnesium. *Phys. Rev.*, **116**, 81 (1959).

[24] K. Huang. Lattice vibrations and optical waves in ionic crystals. *Nature*, **167**, 779 (1951).

[25] K. Huang. On the interaction betwween the radiation field and ionic crystals. *Proc. R. Soc. Lond. A*, **208**, 352 (1951).

[26] M. Born and K. Huang. *Dynamical Theory of Crystal Lattices*, chapter 8, pages 89–100 (Oxford University Press, 1954).

[27] J. J. Hopfield. Theory of the contribution of excitons to the complex dielectric constant of crystals. *Phys. Rev.*, **112**, 1555 (1958).

[28] J. J. Hopfield and D. G. Thomas. Theoretical and experimental effects of spatial dispersion on the optical properties of crystals. *Phys. Rev.*, **132**, 563 (1963).

[29] V. Romero-Rochín, R. M. Koehl, C. J. Brennan and K. A. Nelson. Anharmonic phonon-polariton excitation through impulsive stimulated raman scattering and detection through wave vector overtone spectroscopy: Theory and comparison to experiments on lithium tantalate. *J. Chem. Phys.*, **111**, 3559 (1999).

[30] Y.-Y. Teng and E. A. Stern. Plasma radiation from metal grating surfaces. *Phys. Rev. Lett.*, **19**, 511 (1967).

[31] H. Reather. *Surface plasmons on smooth and rough surfaces and on gratings*, volume 111 of *Springer Tracts in Modern Physics*, chapter 1, pages 10–13 (Springer, 1988).

[32] S. H. Autler and C. H. Townes. Stark effect in rapidly varying fields. *Phys. Rev.*, **100**, 703 (1955).

[33] P. Y. Yu and M. Cardona. *Fundamentles of Semiconductors* (Springer, 1999), 3rd edition.

[34] R. H. Poolman, E. A. Muljarov and A. L. Ivanov. Terahertz response of acoustically driven optical phonons. *Phys. Rev. B*, **81**, 245208 (2010).

[35] E. A. Muljarov, R. H. Poolman and A. L. Ivanov. Resonant acousto-optics in the terahertz range: To-phonon polaritons driven by an ultrasonic wave. *Phys. Rev. B*, **00**, 005200 (2011).

[36] W. C. Tait. Quantum theory of a basic light-matter interaction. *Phys. Rev. B*, **5**, 648 (1972).

[37] R. H. Poolman, E. A. Muljarov and A. L. Ivanov. Ultrasonic control of terahertz radiation via lattice anharmonicity in linbo$_3$. *Appl. Phys. Lett.*, **98**, 263505 (2011).

[38] J. Menéndez and M. Cardona. Temperature dependence of the first-order raman scattering by phonons in si, ge, and $\alpha - sn$: Anharmonic effects. *Phys. Rev. B*, **29**, 2051 (1984).

[39] V. L. Gurevich. *Kinetics of Phonon Systems* (Nauka, 1980).

[40] G. Leibfried and W. Ludwig. Theory of anharmonic effects in crystals. In F. Seitz and D. Turnbull, editors, *Solid State Physics*, volume 12 (Academic Press, New York, 1961).

[41] I. Inbar and R. E. Cohen. Comparison of the electronic structures and energetics of ferroelectric linbo$_3$ and litao$_3$. *Phys. Rev. B*, **53**, 1193 (1996).

[42] K. K. Wong, editor. *Properties of Lithium Niobate*. Number 28 in EMIS Datareviews Series (The Institute of Electrical Engineers, 2002).

[43] S. C. Abrahams. Stoichiometry, defect structure and composition of $LiNbO_3$. In K. K. Wong, editor, *Properties of Lithium Niobate* (The Institute of Electrical Engineers, 2002).

[44] C. A. Schmuttenmaer. Exploring dynamics in the far-infrared with terahertz spectroscopy. *Chem. Rev.*, **104**, 1759 (2004).

[45] S. Kojima, N. Tsumura, W. M. Takeda and S. Nishizawa. Far-infrared phonon-polariton dispersion probed by terahertz time-domain spectroscopy. *Phys. Rev. B*, **67**, 035102 (2003).

[46] P. Y. Han and X.-C. Zhang. Free-space coherent broadband terahertz time-domain spectroscopy. *Meas. Sci. amd Technol.*, **12**, 1747 (2001).

[47] N. S. Stoyanov, D. W. Ward, T. Feurer and K. A. Nelson. Terahertz polariton propagation in patterned materials. *Nature Mater.*, **1**, 95 (2002).

[48] J. C. Feurer, J. C. Vaughan and K. A. Nelson. Spatiotemporal coherent control of lattice vibrational waves. *Science*, **299**, 374 (2003).

[49] P. H. Siegel. Terahertz technology. *IEEE T. Microw. Theory*, **50**, 910 (2002).

[50] B. Fischer, M. Hoffmann, H. Helm, G. Modjesch and P. U. Jepsen. Chemical recognition in terahertz time-domain spectroscopy and imaging. *Semicond. Sci. Technol.*, **20**, S246 (2005).

[51] J. F. Federici, B. Brian Schulkin, F. Huang, D. Gary, R. Barat, F. Oliveira and D. Zimdars. Thz imaging and sensing for security applicationsexplosives, weapons and drugs. *Semicond. Sci. Technol.*, **20**, S266 (2005).

[52] I. H. Libon, S. Baumgärtner, M. Hemple, N. E. Hecker, J. Feldmann, M. Kock and P. Dawson. An optically controllable terahertz filter. *Apl. Phys. Lett.*, **76**, 2821 (2000).

[53] C.-L. Pan, C.-F. Hsieh, R.-P. Pan, M. Tanaka, F. Miyamaru, M. Tani and M. Hangyo. Control of enhanced thz transmission through metallic hole arrays using nematic liquid crystal. *Opt. Express.*, **13**, 113921 (2005).

[54] C.-Y. Chen, C.-L. Pan, C.-F. Hsieh, Y.-F. Lin and R.-P. Pan. Liquid-crystal-based terahertz tunable lyot filter. *Appl. Phys. Lett.*, **88**, 101107 (2006).

[55] I.-C. Ho, C.-L. Pan, C.-F. Hsieh and R.-P. Pan. Liquid-crystal-based terahertz tunable solc filter. *Opt. Lett.*, **33**, 1401 (2008).

[56] T. D. Drysdale, I. S. Gregory, C. Baker, E. H. Linfield, W. R. Tribe and D. R. S. Cumming. Transmittance of a tunable filter at terahertz frequencies. *Appl. Phys. Lett.*, **85**, 5173 (2004).

[57] T. E. Tiwald, J. A. Woollam, S. Zollner, J. Christiansen, R. B. Gregory, T. Wetteroth, S. R. Wilson and A. R. Powell. Carrier concentration and lattice absorption in bulk and epitaxial silicon carbide determined using infrared ellipsometry. *Phys. Rev. B*, **60**, 11464 (1999).

[58] S. G. Tikhodeev, A. L. Yablonskii, M. E. A., N. A. Gippius and T. Ishihara. Quasiguided modes and optical properties of photonic crystals. *Phys. Rev. B*, **66**, 045102 (2002).

[59] A. D. Rakić, A. B. Djurišić, J. M. Elazar and M. L. Majewski. Optical properties of metallic films for vertical-cavity optoelectronic devices. *Appl. Optics*, **37**, 5271 (1998).

[60] N. W. Ashcroft and D. N. Mermin. *Solid State Physics* (Saunders College Publishing, 1976).

[61] H. Ehrenreich and R. Philipp. Optical prperties of Ag and Cu. *Phys. Rev.*, **128**, 1622 (1962).

[62] H. Ehrenreich, R. Philipp and B. Segall. Optical properties of aluminum. *Phys. Rev.*, **132**, 1918 (1963).

[63] D. Y. K. Ko and J. C. Inkson. Matrix method for tunneling in hetrostructures: Resonant tunneling in multilayer systems. *Phys. Rev. B*, **38**, 9945 (1988).

[64] D. Sarid. Long range surface plasmon waves on very thin metal films. *Phys. Rev. Lett.*, **47**, 1927 (1981).

[65] K. F. Riley, M. P. Hobson and S. J. Bence. *Mathematical Methods for Physics and Engineering*, chapter 16, page 573 (Cambridge University Press, 2002), 2nd edition.